A SQUID-Based RF Cavity Search for Dark Matter Axions

Michael T. Hotz

A dissertation
submitted in partial fulfillment of the
requirements for the degree of

Doctor of Philosophy

University of Washington
2013

Reading Committee:
Leslie Rosenberg, Chair
Alejandro Garcia
Thompson Burnett

Program Authorized to Offer Degree:
Physics

University of Washington

Abstract

A SQUID-Based RF Cavity Search for Dark Matter Axions

Michael T. Hotz

Chair of Supervisory Committee:
Dr. Leslie Rosenberg
Physics

The axion is a hypothetical elementary particle resulting from a solution to the "Strong-CP" problem. This serious problem in the standard model of particle physics is manifested as a 10^{10} discrepancy between the measured upper limit and the calculated value of the neutron's electric dipole moment. Furthermore, a light ($\sim \mu$eV) axion is an ideal dark matter candidate: axions would have been copiously produced during the Big Bang and would be the primary component of the dark matter in the universe.

The resolution of the Strong-CP problem and the discovery of the composition of dark matter are two of the most pressing problems in physics. The observation of a light, dark-

matter axion would resolve both of these problems. The Axion Dark Matter eXperiment (ADMX) is the most sensitive search for dark-matter axions. Axions in our Milky Way Galaxy may scatter off a magnetic field and convert into microwave photons. ADMX consists of a tunable high-Q RF cavity within the bore of a large, 8.5 Tesla superconducting solenoidal magnet. When the cavity's resonant frequency matches the axion's total energy, the probability of axion-to-photon conversion is enhanced. The cavity's narrow bandwidth requires ADMX to slowly scan possible axion masses. A receiver amplifies, mixes, and digitizes the power developed in the cavity from possible axion-to-photon conversions. This is the most sensitive spectral receiver of microwave radiation in the world. The resulting data is scrutinized for an axion signal above the thermal background.

ADMX first operated from 1995-2005 and produced exclusion limits on the energy of dark-matter axions from 1.9 μeV to 3.3 μeV. In order to improve on these limits and continue the search for plausible dark-matter axions, the system was considerably upgraded from 2005 until 2008. In the upgrade, the key technical advance was the use of a dc Superconducting QUantum Interference Device (SQUID) as a microwave amplifier. The SQUID amplifier's noise level is near the allowed minimum from quantum mechanics, allowing ADMX to reduce its thermal noise background by up to 100x. However, SQUIDs are extremely sensitive to magnetic fields, such as those within in ADMX. Integrating a SQUID amplifier into ADMX presented a serious technical challenge. Commissioning the SQUID amplifier was a major focus of my thesis work. This work demonstrates the successful use of a SQUID amplifier in ADMX during operations from 2008-2010.

Compared to other dark-matter candidates, the axion's mass and the axion's coupling strength to normal matter and radiation are rather tightly constrained. This allows for the near-definitive elimination or detection of dark-matter axions. A successful detection in ADMX would immediately lead to a determination of the axion's spectral line shape. This shape encodes the history of the Milky Way's formation and is therefore of high scientific importance. The imperfectly-constrained Milky Way dark-matter halo, however, produces

remnant uncertainties of the axion signal in both its spectral line-shape and its total intensity, complicating the ADMX search. This work investigates proposed features of dark-matter halo models which enhance ADMX's sensitivity. From these models, this work presents the corresponding exclusion limits for both the local axion density and axion-to-photon coupling strength for axions with mass in the 3.36 μeV to 3.69 μeV region.

Contents

List of Figures

Acknowledgments

First and foremost, I want to thank my advisor Leslie Rosenberg. His guidance has helped me to navigate the craziness of national lab bureaucracy and grow as a productive scientist. I thank my reading committee members, Thompson Burnett, and Alejandro Garcia who read through this document and provided valuable advice during my tenure as a graduate student. This experiment would not be possible without my many colleagues, especially Gianpaolo Carosi, Gray Rybka, Andrew Wagner, Dmitry Layapustin, and Christian Boutan. Finally, I want to thank my family and my partner, Liz Manrao, for being loving and supportive though graduate school and especially the last year of completing my degree.

Dedication

This work is dedicated to all future ADMX researchers. I hope that this dissertation proves useful to understanding the experiment. Good Luck!

Chapter 1

Introduction

1.1 The Axion Particle

Over the last century, particle physicists have determined the composition of matter at the smallest scales and highest energies. They discovered a myriad of subatomic particles: hadrons, leptons, and gauge bosons. While the 6 leptons and photon, Z, and W bosons lack any detected internal structure, the zoo of hadrons is composed of combinations of the 6 quarks and 8 gluons. All these particles interact by one of the four fundamental forces: strong mediated by the gluons, weak mediated by the W's and the Z, electromagnetic mediated by the photon, and gravitational. The "Standard Model" of particle physics is a robust framework that predicts particle dynamics, interactions, and decays from their masses, charges, quantum numbers, and interaction rules. The Standard Model successfully predicts the complicated processes seen in particle-accelerator collisions and has endured nearly four decades of experimental scrutiny.

Within the Standard Model is the theory of Quantum ChromoDynamics (QCD). QCD describes the strong interaction, the force between quarks. QCD is expected to violate time reversal symmetry. The weak force and everyday life violate time reversal symmetry. However, no evidence for time reversal symmetry breaking has been detected in QCD, leading to a 10^{10} discrepancy between theory and observation. This discrepancy is called the "Strong-CP" problem [1]. As discussed in chapter 2, this problem is perhaps best resolved by the "Peccei-Quinn" solution [2]. This solution introduces a new, hidden symmetry, which was spontaneously broken in the early universe. The breaking of the symmetry resulted in a new particle, the axion [3] [4]. It happens that the axion, introduced to solve a small-scale particle-physics problem, also may play a profound role on the universe at the largest scales.

1.2 The Dark Matter Problem

A long-standing issue in cosmology is the question of what makes up dark matter. Dark matter is a non-luminous form of mass that's gravitationally inferred from the motions of galaxies and galaxy clusters. As discussed in chapter 3, astronomers and cosmologists have made an astounding discovery [5]: only 4.6% of the universe's overall matter and energy density is composed of normal "baryonic" matter (figure 1.1). The remaining 95% of the universe's density is composed of two exotic species: "dark matter" and "dark energy".

Seventy-two percent of the energy density of the universe is dark energy. Unlike structures like stars and galaxies, dark energy is uniformly distributed throughout space. Dark energy acts as a pressure, pushing the universe apart and thereby causing the universe's outward expansion to accelerate. Particle physics has few good ideas of the fundamental nature of dark energy. The nature of dark energy will not be addressed in this work.

Comprising the remaining twenty-three percent of the universe's energy density is dark matter, an unknown type of matter that dominates large gravitational potentials like galaxies and galaxy clusters. Dark matter is non-luminous and non-interacting yet has gravitational interactions. Determining the composition of dark matter is one of the most important scientific problems today [6]. Particle physics provides several dark-matter candidate particles, including the axion. A light axion, produced in great abundance during the early universe, would account for the density of dark matter observed in the universe today. Hence, light

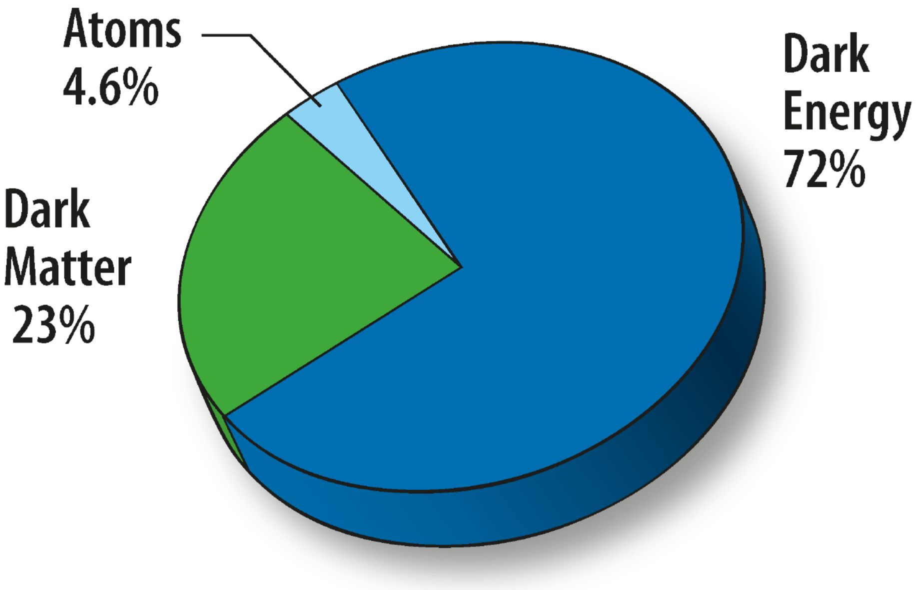

Figure 1.1: The composition of the universe. At the largest scales, the universe is assumed to be isotropic and homogeneous. This assumption allows for the measurement of the matter and energy density of the universe. It is found that less than 5% of the universe is comprised of atoms. More than 95%, of the universe is dark energy and dark matter. [5]

axions are a highly compelling dark-matter candidate.

1.3 Detecting the Dark-Matter Axion

The Axion Dark Matter eXperiment (ADMX) is the most sensitive search for plausible dark-matter axions. Chapter 4 details the workings of ADMX. Dark-matter axions rarely decay into microwave photons (with a lifetime of around 10^{54} seconds). ADMX enhances the spontaneous axion-to-photon decay rate by a factor of roughly 10^{37} by means of a tunable, resonant cavity immersed in a strong magnetic field. In ADMX, the magnetic field is produced by a 9 Ton, 8.5 Tesla superconducting solenoidal magnet, contained within the cryostat shown in figure 1.2. The resonant cavity, tuning system, and detection electronics are contained within an experimental package installed in the magnet's bore, the top of which is shown in figure 1.3. The resonant cavity and electronics introduce black-body and thermal photon backgrounds which compete with the expected axion decay signal. By cool-

Figure 1.2: Photo of the ADMX magnet being installed at the University of Washington. The data presented here was collected during ADMX's run from 2008-2010 at the Lawrence Livermore National Lab. The 9 ton, 3.4 meter tall magnet and cryostat were then transported 1400 km to Seattle.

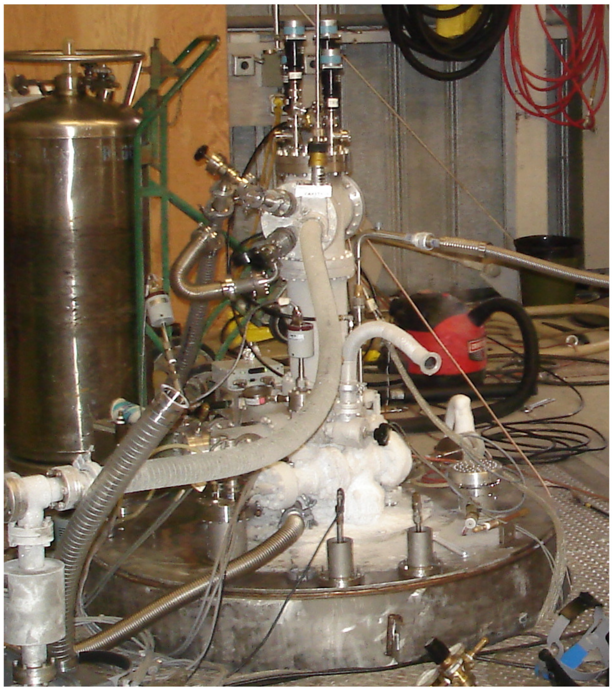

Figure 1.3: Photo of the top of ADMX. The experimental insert extends roughly 3.4 meters into the magnet's bore. The top of the insert has all of the mechanical, electrical, and vacuum connections necessary to operate the insert. The frost is due to cold, helium exhaust produced as the microwave cavity is cooled from 78 K to 4.2 K.

ing the cavity and electronics with liquid helium, ADMX reduces the thermal background and becomes more sensitive to dark-matter axions.

The masses and couplings of axions searched for by ADMX are within a highly compelling dark-matter axion window, with a mass range from roughly 1 μeV to 10 meV and a coupling-range spanning a factor of 3x in axion-to-photon coupling strength. During its 1995 to 2005 run, ADMX search for axions with masses from roughly 2 μeV to 4 μeV at relatively high coupling strength. From 2005 to 2008, ADMX underwent an upgrade to improve its sensitivity to a larger range of axion models. To achieve the increase in sensitivity, a Superconducting Quantum Interference Device (SQUID) microwave amplifier was installed as the primary amplifier of the detector electronics. The microwave SQUID amplifier can operate near the limit of noise allowed by quantum mechanics, allowing ADMX to reduce the noise backgrounds and improve sensitivity by up to 100x. The SQUID amplifier, however, is extremely sensitivity to magnetic fields, and ADMX's magnet generates a large, high-field environment. ADMX had to be substantially modified to create a zero-field volume deep inside the experiment to house the SQUID amplifier. Chapter 4 describes the successful operation of a SQUID amplifier within ADMX during the 2008-2010 run.

Chapter 5 describes the algorithms used to convert the signal recorded by ADMX into a search for dark-matter axions. Within this analysis, several models of the nature of the Milky Way's dark-matter halo are investigated. The baseline halo model in most dark-matter searches is the isothermal-sphere model, which is assumed in the baseline sensitivity of ADMX. Halo models such as the "dark disk" model [7] and the "caustic ring" model [8] are demonstrated to significantly enhance the sensitivity of ADMX.

As elaborated in the chapter 6, ADMX is by far the most sensitive search for one of the most compelling dark-matter candidates, the axion. This work demonstrates the successful operation of ADMX and provides the most sensitive limits to axion density and coupling to date. ADMX will be further upgraded towards the definitive axion dark-matter search. Assuming equal likelihood for the axion's allowed masses and couplings, the search during the next few years has roughly a 20% chance of finding the dark-matter axion, if it exists.

Chapter 2

Motivation for the Axion Particle

The existence of the axion is motivated by a solution to the Strong-CP problem in the theory of Quantum ChromoDynamics (QCD). This chapter begins by describing the fundamentals of QCD. It then describes an early issue in QCD known as the $U(1)_A$ problem. The detailed resolution of the $U(1)_A$ problem produces the "Strong-CP" problem. A solution to Strong-CP problem is the Peccei-Quinn solution, which produces an undetected light and weakly coupled particle named the axion. This chapter concludes by describing various models and properties of the axion.

2.1 Introduction to QCD

The story of QCD begins with the fundamental quest of particle physics: to describe the most basic building blocks of nature in a rigid, mathematical framework. During the nineteenth century, the atomic theory developed into the field of chemistry. In 1897, Thompson discovered the first fundamental particle: the electron. In 1909, Rutherford discovered that atoms contained a hard and heavy nucleus and in 1917 identified the proton. The discovery of protons, neutrons, and electrons allowed for the many elements to be described by different combinations of only 3 particles.

By the middle of the 1960s, dozens of particles had been discovered in a variety of experi-

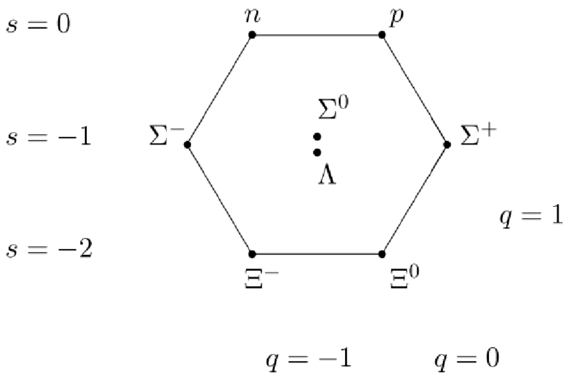

Figure 2.1: The Eightfold Way for spin-1/2 baryons. This classification organizes spin-1/2 baryons according to charge and mass/strangeness. It was realized that the same organization is generated with the quark model.

ments. The majority of these particles were classified as “hadrons” which are heavy particles that interact with each other through the strong force responsible for binding neutrons and protons into nuclei. The growing zoo of hadrons was organized by electric charge, mass, spin, and “strangeness”. Gell-Mann realized that the hadron spectrum could be explained with a scheme called the “Eightfold Way” [9]. In this scheme, hadrons were first grouped by spin, then by mass and charge. Figure 2.1 shows the resulting order of this scheme on the spin-1/2 baryons. The Eightfold Way organizes hadrons analogous to how the periodic table organizes atoms. Soon after proposing the Eightfold Way, Gell-Mann realized that the organization of the Eightfold Way could be reproduced if the hadrons were composed of two or three fractionally charged sub-particles called quarks. Since all experimental searches for the fractionally charged quarks failed, the idea of quarks as real particles was disfavored over quarks simply being mathematical constructs.

During the late 1960s, an electron accelerator at SLAC fired high energy electrons at a fixed proton target. These high energy electrons shattered the protons, inelastically scattering the incident electron. By measuring the angle and energy of the scattered electron, the momentum transfer of the collision was measured. The recoiling electron’s kinematics suggested that the electron was striking localized particles or “partons” inside the proton, analogous to the dense nucleus of an atom [10]. However, unlike the stationary nucleus of an atom, these particles appeared unbound, with relativistic velocities while inside the proton. This property, called asymptotic freedom, meant that partons (quarks) are particles, but must experience a strong force that kept them confined inside a hadron. With this discovery, the quarks were found to be real particles, but with the unusual property of being confined within hadrons.

Simultaneously as experiments discovered new particles, mathematicians and theoretical physicists found new models to describe the observed dynamics. A major discovery was the gauge theory, which is a relativistic and quantized field theory that is invariant under a group of "local" transformations[1]. In group-theory terminology, the collection of all possible phase transformations is known as the unitary group of dimension 1 or U(1). The gauge theory with a U(1) symmetry just happens to reproduce Maxwell's equations: the U(1) gauge theory is the basis of Quantum Electrodynamics (QED), which accurately describes particles' electro-magnetic interactions at all scales and speeds. The U(1) symmetry has one generator, corresponding to the gauge boson of QED, the photon. Also the U(1) symmetry has dimension 1, corresponding to charge conservation in QED. The great success of QED lead to the investigation of other gauge-invariant field theories.

An "SU(3)" gauge theory is the foundation of QCD and the strong interaction.[2] The 3 dimensions of SU(3) in QCD lead to the conservation of the three "color" charges of "red", "green", and "blue". The fermionic quarks possesses color charge and come in two chiralities, left-handed and right-handed. The 8 gauge bosons of QCD, corresponding to the 8 generators of SU(3), are called gluons. From perturbation theory, QCD predicts that quarks are asymptotically free, in agreement with experiment. In the non-perturbative, strongly-coupled realm of QCD, lattice calculations have demonstrated the confinement of quarks inside hadrons. The revolution in computing power since QCD's birth in the 1970s

---

[1] A local symmetry allows for different transformations at every point. If only the same transformation at all points is invariant, this weaker symmetry is called "global".

[2] SU(3), the special unitary group of dimension 3, is the set of all possible matrices of dimension 3 with a determinant of 1.

has allowed for more accurate and complicated calculations of observables from QCD. Like QED before it, QCD has remained robust to experimental scrutiny.

2.1.1 The $U(1)_A$ Problem

QCD, while elegant and accurate, is not without issue. The QCD issues that gives rise to axions originate from problems involving one-dimensional "axial" transformations, which rotate the chirality of quarks from left-handed, L, to right handed, R. These issues are best illustrated in a simplified QCD model, described by the Lagrangian:

$$\mathcal{L}_{QCD} = \sum_{x=u_L,u_R,d_L,d_R} \bar{q}_x i\gamma^\mu \partial_\mu q_x - \frac{1}{4} G^a_{\mu\nu} G^{\mu\nu}_a \tag{2.1}$$

Since quarks are effectively massless at high energy, this simple QCD model consists of two massless quark flavors, u and d, each possessing left handed, L, and right handed, R, chiralities, along with the gluon fields, $G^a_{\mu\nu}$.

Performing unitary transformations that rotate the flavors ($u \leftrightarrow d$) and chiralities ($L \leftrightarrow R$) do not change the observables in this model. Therefore, this model is said to have $U(2)_R \bigotimes U(2)_L$ symmetry, where $U(2)$ is the unitary group of order 2. By factoring out the complex $U(1)$ transformations, these symmetry groups are equivalent to the groups $SU(2)_R \bigotimes U(1)_R \bigotimes SU(2)_L \bigotimes U(1)_L$. These symmetries can be re-ordered into symmetries that transform chirality identically, called "vector" symmetries and symmetries that transform chirality oppositely, called "axial" symmetries: $SU(2)_V$, $SU(2)_A$, $U(1)_V$, and $U(1)_A$.

Two of these symmetries, $SU(2)_V$ and $U(1)_V$, are approximately good symmetries of nature and have associated conserved quantities. $SU(2)_V$ conserves isospin, which successfully describes the organization of hadrons of similar masses. $U(1)_V$ conserves baryon number. The $SU(2)_A$ is spontaneously broken through the formation of $u\bar{u}$ and $d\bar{d}$ quark condensates. A spontaneously broken symmetry produces massless particles called Nambu-Goldstone bosons. If the symmetry is not exact, as in this case, the resulting bosons are

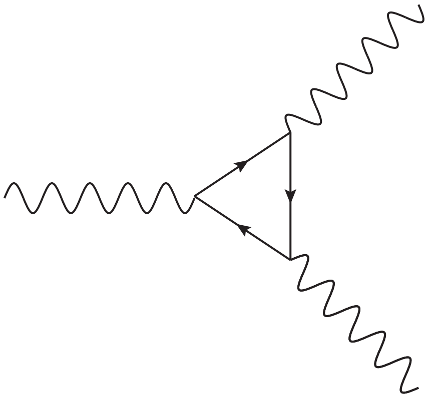

Figure 2.2: The triangle diagrams above creates the Adler-Bell-Jackiw anomaly. The self-interaction of the gauge fields create an axial current which breaks the $U(1)_A$ symmetry.

massive. The breaking of $SU(2)_A$ produces the pions: π^0, π^+, and π^-.

The $U(1)_A$ symmetry is also expected to be broken in the same manner as the $SU(2)_A$. The spontaneous breaking of the $U(1)_A$ symmetry should produce a chargeless boson, with an expected mass less than $\sqrt{3}m_\pi$. However, there is no discovered particle that matches the expected mass and quantum numbers. The closest particle with the correct quantum numbers is the η, whose mass is significantly higher than the pion masses. The large discrepancy between the observed η mass and its expected mass is only one of the facets of the $U(1)_A$ problem of QCD [11]. The broken $U(1)_A$ symmetry also creates serious discrepancies between the observed and predicted decay channels and decay rate for the η. These serious discrepancies, called the $U(1)_A$ Problem, were a serious threat to the viability of QCD.

2.1.2 Resolving the $U(1)_A$ Problem

A promising solution to the $U(1)_A$ problem is from the Adler-Bell-Jackiw anomaly [12] [13], calculated by the triangle diagram shown in figure 2.2. This anomaly introduces an axial current which breaks the $U(1)_A$ symmetry:

$$\partial_\mu J^5_\mu = -i\frac{Ng_s^2}{16\pi^2}G^a_{\mu\nu}\widetilde{G}^a_{\mu\nu} \tag{2.2}$$

where N is the number of quark flavors, g_s is the coupling strength, $G^{\mu\nu a}$ is the gluon field strength tensor, and $\widetilde{G}^a_{\mu\nu}$ is the dual of $G^{\mu\nu a}$. However, if QCD's vacuum is trivial, with a field strength of zero everywhere, then the axial current is zero and the $U(1)_A$ problem remains.

The topological properties of the SU(3) gauge fields of QCD produce a complex vacuum. It so happens that there are an infinite set of gauge fields which minimize the action and are vacuum states [14] [15]. These vacua are characterized by an integer, n, which form the set of possible vacua $|n\rangle$. These vacua, while gauge equivalent, are isolated from one another and cannot be continuously transformed into one another: transforming one $|n\rangle$ vacuum to another continuously requires intermediate gauge fields which are not vacuum states. However, these energy barriers are finite and tunneling events, called instantons, connect the vacua together [16]. Shown if figure 2.3, instanton solutions, which minimize the action for tunneling from one vacuum to another, are characterized by an integer q which connects a $|n\rangle$ vacuum to a $|n+q\rangle$ vacuum. The gauge fields for these instanton solutions satisfy:

$$q = \frac{g_s^2}{32\pi^2} \int G^a_{\mu\nu} \widetilde{G}^a_{\mu\nu} d^4x \tag{2.3}$$

Note that for the q=1 case, integrating equation 2.2 results in an axial charge violation of $2N$. The QCD vacuum, with instanton tunneling events, breaks the $U(1)_A$ symmetry, solving the $U(1)_A$ problem [17]. Since any single $|n\rangle$ vacuum is not stable, the true vacuum is a superposition of them:$|\theta\rangle = \sum e^{in\theta}|n\rangle$ for any $0 < \theta < 2\pi$. Each value of θ defines a unique, gauge-invariant vacuum. The parameter θ characterizes the intensity of vacuum to vacuum tunneling, with $\theta = 0$ equivalent to the trivial vacuum, with its associated $U(1)_A$ problem.

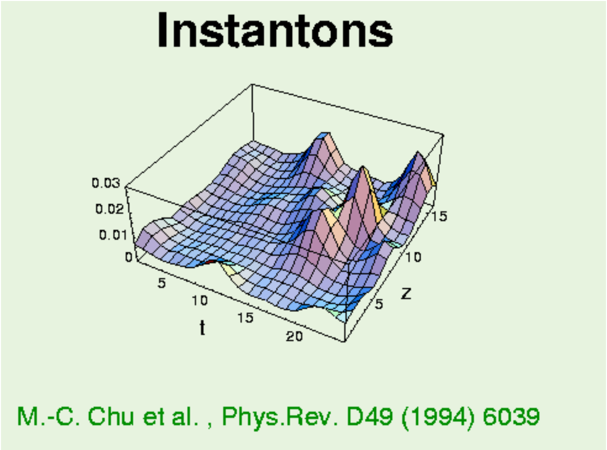
Instantons

M.-C. Chu et al. , Phys.Rev. D49 (1994) 6039

Figure 2.3: Visualization of Instantons. This 3 dimensional slice of a 4 dimensional Euclidean space shows a simulation of the QCD vacuum. Two spacial dimensions, x and y, are fixed. The action density of the gluon configuration is mapped for a single spacial dimension, z, and time, t. The localized excitations illustrate the concept of instantons as psuedoparticles. Instantons in real time are tunneling events where the QCD vacuum changes. These changes do not conserve Parity or Time symmetry. As the density of instantons, parametrized by θ, increases, the gluon vacuum has more parity and time violation. Instantons are represented as peaks on the plot.

The θ vacuum adds an effective term to the QCD Lagrangian:

$$\mathcal{L}_\theta = \theta \frac{g_s^2}{32\pi^2} G^{\mu\nu a} \widetilde{G}^a_{\mu\nu} \tag{2.4}$$

This term breaks axial chiral symmetry by $-2\theta/N$. Therefore, axial chiral rotations of the QCD Lagrangian by $e^{i\gamma_5\epsilon}$ transform θ to $\theta - 2\epsilon/N$. When the quarks are given masses, then axial chiral rotations also transform the quark mass matrix. In the physical world, the quark's all have real masses. Therefore, the observable, $\overline{\theta}$, is defined when the quark masses are made real by axial chiral rotations:

$$\overline{\theta} = \theta + \arg\det M \tag{2.5}$$

where M is the quark mass matrix.

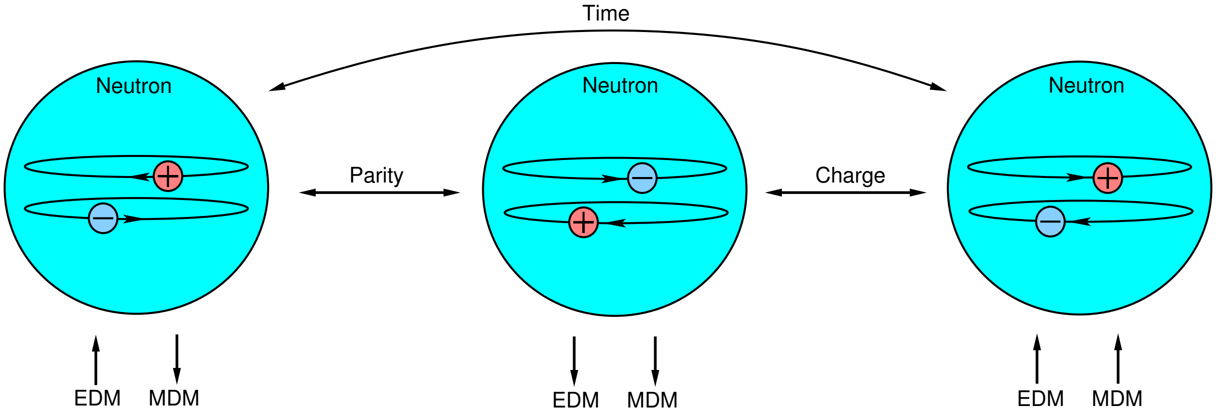

Figure 2.4: Model of a neutron with both electric and magnetic dipole moments. Under parity transformation, where the two charges switch positions, the electric dipole moments change direction while the magnetic dipole moment stays the same. This results in an anti-symmetric parity transformation. Additionally, in a time-reversal there is also an anti-symmetry. Charge, however, is conserved. Therefore, if the neutron possessed an electric dipole moment it would be CP violating. By measuring the neutron's electric dipole moment, experiments have placed limits on the degree of CP violation in QCD.

2.2 CP Violation ($\not{C}\not{P}$) in QCD

The θ vacuum introduced in the solution to the $U(1)_A$ problem produces an observable parameter of the Standard Model, $\bar{t}heta$. $\mathcal{L}_{\overline{\theta}}$ conserves charge symmetry, C, but violates conservation of parity symmetry, P, and time symmetry, T, for all $\overline{\theta} \neq 0$. This means that the equations of motion remain unchanged under inversion of charge, but not parity or time.

By measuring the P and T violation of baryons, the value of $\overline{\theta}$ can be determined experimentally. The most sensitive measurement of $\overline{\theta}$ is from measuring the neutron's permanent electric dipole moment (EDM). As shown in figure 2.4, a neutron with a permanent electric dipole and a magnetic dipole has P and T violation. The most sensitive measurement of the neutron electric dipole moment is $|d_n| < 2.9 \times 10^{-26}$ e-cm, corresponding to a limit of $\overline{\theta} < 10^{-10}$ [18].

The Strong-CP problem is: why is $\overline{\theta}$ so small when, as a phase, it is equally probable to be anywhere in the range of 0 to 2π? Furthermore, θ is from the strong interaction while $\arg\det M$ is from the weak interaction. Why would two phases, each expected anywhere from 0 to 2π so neatly cancel? The Strong-CP problem is a fine tuning problem: the universe seems extremely improbable.

One proposed solutions to the Strong-CP problem is to require one of the quarks to be massless. If there were a massless quark, then $\arg\det M$ is not defined, and $\overline{\theta}$ becomes undefined as well, making it not observable. This simple solution to the strong-CP problem is highly unlikely due to the mass measurement of the lightest quark, the up, being 1.7 to 3.1 MeV [19]. Another, more compelling, solution to the Strong-CP problem comes from Peccei and Quinn who introduce new physics to force $\overline{\theta}$ to dynamically to zero.

2.2.1 The Peccei-Quinn Solution to the Strong-CP Problem

Peccei and Quinn discovered a novel solution to the Strong-CP problem using a modified Higgs mechanism [2]. The Higgs mechanism gives fermions, like quarks, masses due to the "Yukawa" interaction between the fermion fields and the non-zero vacuum expectation value of the Higgs field. In the Peccei and Quinn model, a global U(1) chiral symmetry, called $U(1)_{PQ}$ governs the Higg's wine-bottle-shaped potential, shown in figure 2.5. The instanton term of the QCD Lagrangian tips the wine bottle as a function of θ. Since the quarks acquire their masses from this Higgs potential, their acquired masses are complex, with a phase of $-\frac{\theta}{2}$. This makes the second part of $\overline{\theta}$ in equation (2.2), $\arg\det M$, equal to $-\theta$. Hence $\overline{\theta} = \theta - \theta = 0$, solving the CP problem.

2.3 The Axion

The Peccei-Quinn Solution to the Strong-CP Problem includes a broken $U(1)_{PQ}$ symmetry. A spontaneously broken symmetry generates a Nambu-Goldstone boson. Weinberg [3] and Wilczek [4] recognized that the breaking of the $U(1)_{PQ}$ symmetry produces a low mass boson. It was named the axion after a popular laundry detergent at the time since it cleaned up the Strong-CP problem.

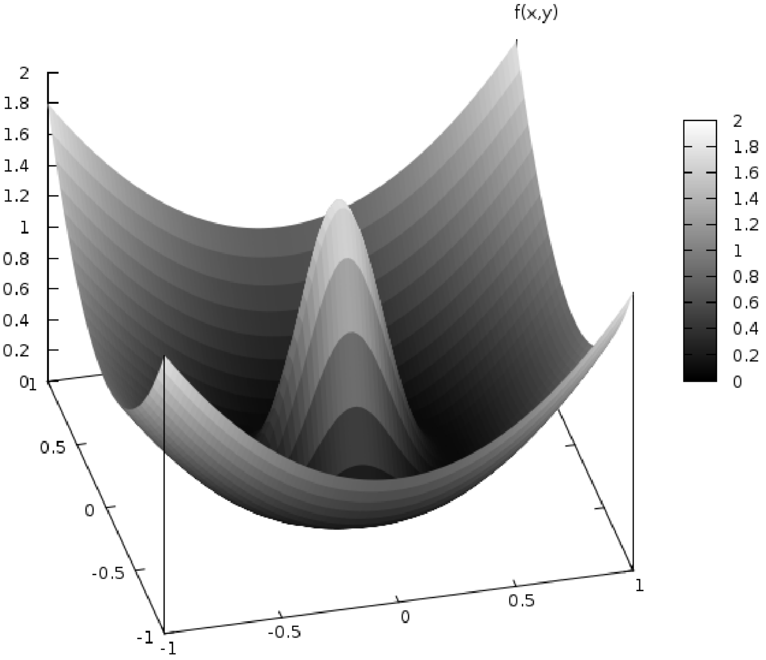

Figure 2.5: A two dimensional Wine Bottle potential. While level, there is a ring of lowest potential. In the Peccei-Quinn model, the effects of instantons via the θ term in the Lagrangian tip the potential, reducing the ring of lowest potential to a single point. This point gives the quarks complex masses, exactly canceling out the P and T violating effects of QCD.

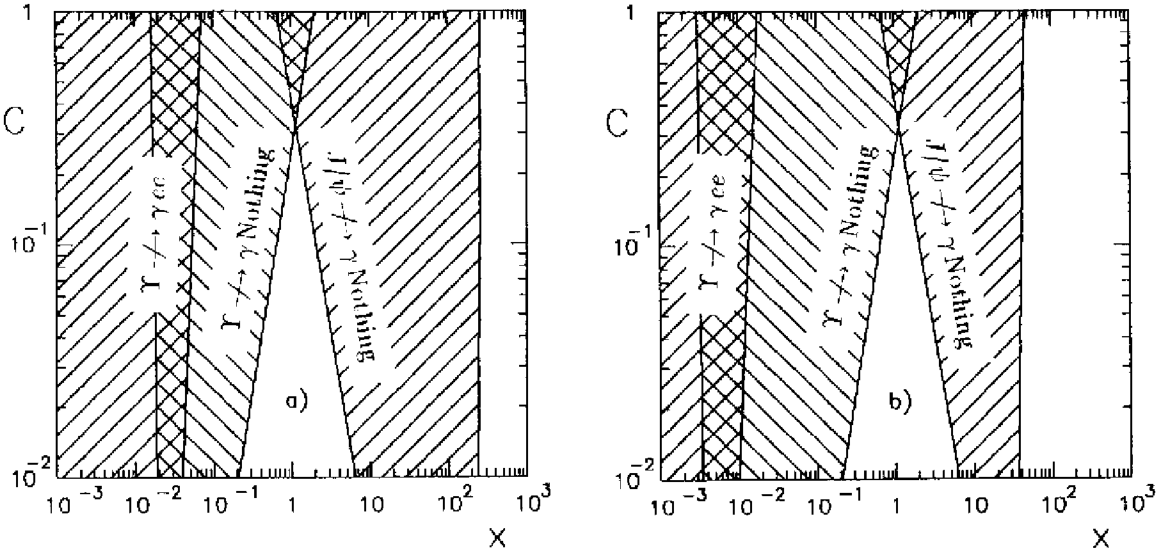

Figure 2.6: Experimental elimination of the PQWW Axion. The vertical axis is the QCD correction factor, C, which is estimated to be around 0.5. The horizontal axis, x, is the ratio of the vacuum expectation values of the complex scalar doublet fields. The two plots illustrate experimental results for various models. The cross-hatched regions are bounds that have been experimentally excluded. This data represents the exclusion of all but the heaviest PQWW axions, shown as the unhatched area. The Crystal Ball detector at the SPEAR looked for $\Upsilon(1S)$ and J/Ψ decays to axions and found no evidence [20].

2.3.1 The Peccei-Quinn-Weinberg-Wilczek (PQWW) Axion

The PQWW axion model assumes that there are two Higgs fields that conserve $U(1)_{PQ}$, ϕ_1 and ϕ_2, where ϕ_1 couples to up-type quarks and ϕ_2 couples to down-type quarks. There is one free parameter of the PQWW axion: the ratio of the vacuum expectation values of the Higgs fields, $x = \frac{\langle\phi_1\rangle}{\langle\phi_2\rangle}$. The symmetry breaking scale of $U(1)_{PQ}$ is assumed to be the weak scale. The mass of the PQWW axion is given by: $m_a \simeq 25N(x + \frac{1}{x})$ keV, where N is the number of generations of quarks (3 in the Standard Model). High energy experiments quickly eliminated this heavy PQWW axion, as shown in figure 2.6. However, simple extensions of the PQWW model were introduced that allow for the creation of an "invisible" axion.

2.3.2 The Invisible Axion

Soon after the proposal and elimination of the PQWW axion model, new models detached the axion from the weak scale, allowing for the creation of an "invisible" axion. This is accomplished by adding high energy extensions to the PQWW axion model, which results in reducing the invisible axion's coupling and mass. The invisible axion's mass and couplings are inversely proportional to the Peccei-Quinn symmetry breaking scale, f_a. If f_a is very large, then any new physics introduced at the f_a scale are not detectable and the resulting light axion is nearly undetectable. The invisible axion's mass is:

$$m_a = \frac{z^{1/2} f_\pi m_\pi}{f_a(1+z)} \sim \frac{.01 GeV^2}{f_a} \tag{2.6}$$

where f_a is the symmetry breaking scale and z is the ratio $\frac{m_u}{m_d}$.

A promising avenue for detecting the invisible axion is by searching for the axion decaying into photons [21]. While axions have no electric charge, anomalies allow for axions to couple to photons. The interaction term for axions to photons is:

$$\mathcal{L}_{a\gamma\gamma} = -g_{a\gamma\gamma} \mathbf{E} \cdot \mathbf{B} a \tag{2.7}$$

where $\mathbf{E}$ is the electric field, $\mathbf{B}$ is the magnetic field, a is the axion field, and $G_{a\gamma\gamma}$, the anomalous coupling to photons is:

$$g_{a\gamma\gamma} = \frac{\alpha}{2\pi f_a} \left(\frac{E}{N} - \frac{2}{3} \frac{4+z}{1+z} \right) \tag{2.8}$$

where E and N are the electromagnetic and color anomalies and α is the fine structure constant. The Feynman diagram for this interaction is shown in figure 2.7. There are two primary invisible axion models, KSVZ and DFSZ.

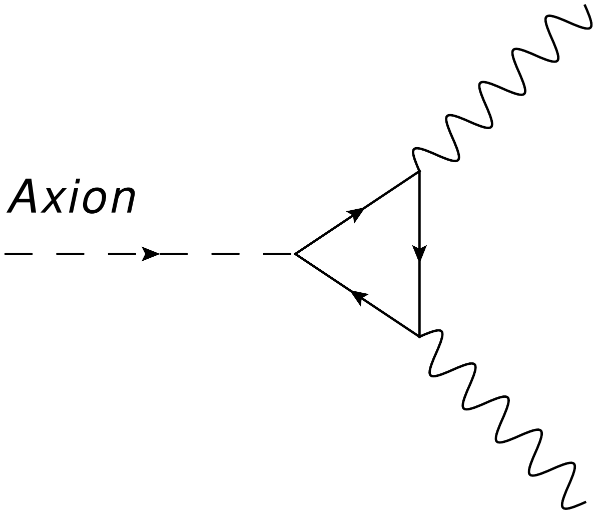

Figure 2.7: A Feynman diagram for an axion decaying to two photons. Since axions do not carry electric charge, they couple to photons through leptons and quarks. The Standard Model particles that the axion couples to is model dependent. In KSVZ, only the zero charge, heavy singlet quark couples to axions. In DFSZ, the axion couples to all quarks and leptons.

The KSVZ Axion

The first invisible axion model was proposed by Kim [22], Shifman, Vainshtein, and Zakharov [23], or KSVZ. In this model, a heavy singlet quark and a high energy singlet scalar field are added to the Peccei-Quinn mechanism. The additional quark and scalar field do not interact through the electroweak interaction, so f_a can be arbitrarily large. The resulting "hadronic" axion only couples directly to this heavy quark and scalar field, producing $E/N = 0$ for equation 2.8. Ironically, the KSVZ model couples to photons more strongly than other invisible axion models. However, the required heavy singlet quark and scalar field, while not experimentally accessible, are not compatible with most extensions of the Standard Model. A second invisible axion candidate was introduced that is compatible with many extensions of the Standard Model.

The DFSV Axion

The second major invisible axion model was proposed by Dine, Fischler, Srednicki [24], and Zhitnitsky [25], or DFSZ. This model is compatible with $SU(5)$ extensions of the Standard Model or the Grand Unified Theory, a theory that unifies the strong and electroweak interactions. In DFSZ, a singlet scalar field is added to the Peccei-Quinn mechanism. This scalar field can be arbitrarily high energy, allowing for arbitrarily high f_a, similar to the KSVZ model. The DFSZ axion couples to all fermions, producing $E/N = 8/3$ for equation 2.8. DFSZ axions have weaker coupling to photons than KSVZ, making them more difficult to detect.

This work describes the search for KSVZ-model axions. The experiment described in chapter 4 lacks the sensitivity to detect DFSZ-model axions in a reasonable amount of time.

Chapter 3

The Axion as Dark Matter

The overall matter and energy composition of the universe is now known to unprecedented precision. The majority of the universe's matter, however, has never been observed directly, only inferred gravitationally. This matter is called "dark matter", and the nature of dark matter is one of the most important questions in science today. The axion, introduced in the previous chapter, is a compelling dark matter candidate particle. Detecting the axion would identify the nature of dark matter. Furthermore, observations of axions in ADMX would provide a detailed history of the Milky Way Galaxy's formation.

This chapter begins with an introduction to cosmology. It then discusses evidence for the existence of dark matter. This chapter then provides an overview of possible dark-matter particles. The axion as a dark-matter candidate is described. Finally, the structures formed from dark matter are then described in the context of detecting dark matter directly within our Milky Way Galaxy.

3.1 Introduction to Cosmology

While the general understanding of particle physics has only slowly evolved over the last few decades, cosmology has changed radically. I feel that the most dramatic advances in our understanding of nature have come from cosmological studies. These advances have given us tremendous insight into the creation and evolution of our universe.

Early in the 20th century, the emerging field of general relativity provided a rigorous basis for understanding the gross structure of the universe. Specifically, general relativity connected the mass and energy density of the universe with its geometry and history. The kinematics of the universe can be described with just a few parameters, and a major achievement of science has been the accurate determination of these parameters. We have entered the epoch of precision cosmology, in particular, we know the overall density of matter in the universe to good precision, at the 1% level. As described later, normal "baryonic" matter cannot constitute the majority of the matter of the universe. Therefore some exotic form of matter, named "dark matter", is required.

3.1.1 Model of our Universe

Cosmological models generally assume that the universe is homogeneous and isotropic. Although this is a poor assumption on the human scale, on cosmological scales these assumptions appear valid. The combination of homogeneous and isotropic space with general relativity generate the equations of motion for the universe's size or scale, called the Friedmann equations:

$$\frac{\dot{a}^2}{a^2} = \frac{8\pi G\rho + \Lambda}{3} - \frac{\kappa}{a^2} \tag{3.1}$$

$$\frac{\ddot{a}}{a} = -\frac{4\pi G}{3}(\rho + 3p) + \frac{\Lambda}{3} \tag{3.2}$$

where $a(t)$ is the relative size of the universe called the scale factor, ρ is the total matter and energy density, κ is the geometry factor of spacetime, described in the next section, p is the pressure exerted by matter and energy on $a(t)$, and Λ is the cosmological constant, which acts as an extra pressure. Λ was introduced to counteract the gravitational collapse in the

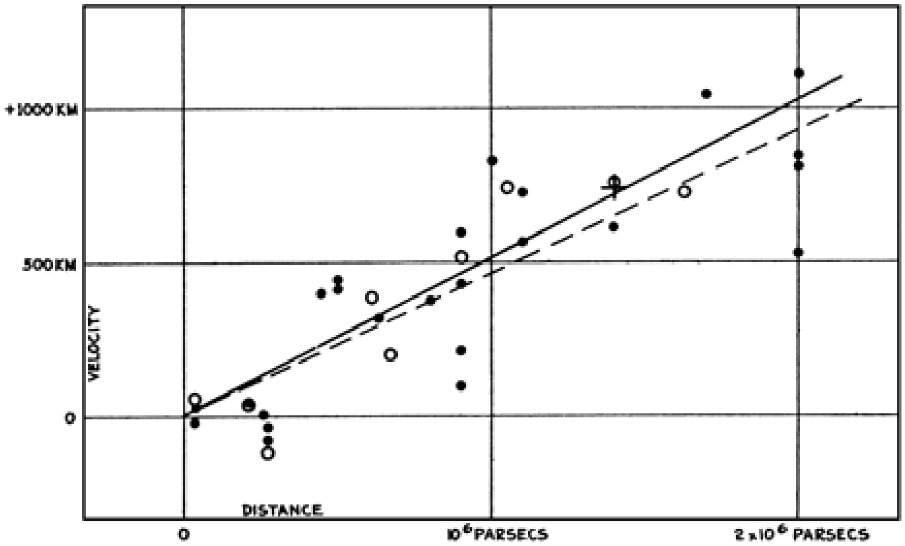

Figure 3.1: The original Hubble flow plot showing galaxy speeds versus distances. The speed of regression of various galaxies is measured accurately by Doppler shifts in spectroscopic measurements. These velocities are plotted verses their distance from earth in parsecs. Distance was calculated based on comparing the measured apparent magnitudes to the known absolute magnitude of “standard candle” Cepheid variables inside of these galaxies. Hubble’s arbitrary fit lines indicates that galaxies further away are moving at a faster velocity. While his measurement had enormous systematic errors, the trend of more distant galaxies moving faster is robust. [26]

observed matter-dominated universe, allowing for a cosmological model of a static universe. In the 1920s, however, Hubble discovered that the universe was expanding (figure 3.1). The rate that galaxies moved apart was parametrized with the Hubble Constant, $H_0 \equiv \dot{a}/a$ in the Friedmann equations [26]. Early evidence of a universe where galaxies moved away from each other challenged the static universe cosmology. Instead, the universe was evolving over time.

The future of the universe depends on its normalized matter and energy density, given by $\Omega \equiv \rho/\rho_c$, where $\rho_c = 3H^2/8\pi G$. Ω also controls the universe’s shape, which is parametrized by the geometry factor, κ. If $\Omega > 1$ then $\kappa = 1$ and the universe is spherical, with parallel lines eventually intersecting. A spherical universe will eventually collapse on itself in a “Big Crunch”. If $\Omega = 1$, then $\kappa = 0$ and the universe is “flat” or Euclidean, with parallel lines remaining parallel to infinity. A flat universe will expand and asymptotically approach some

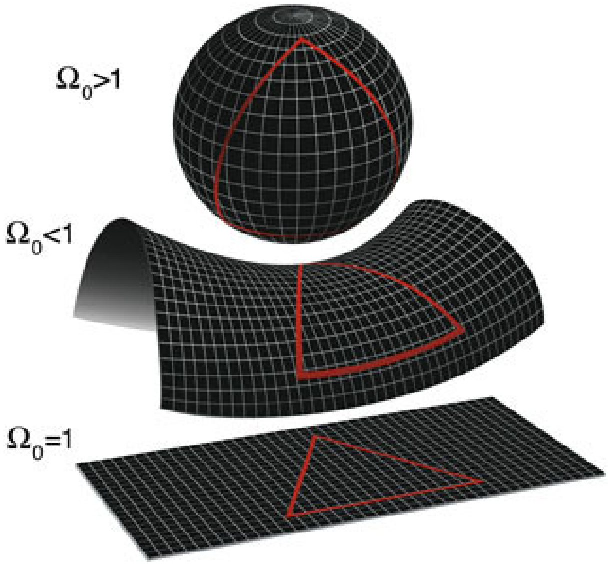

Figure 3.2: This diagram shows how the geometry of the universe is dependent on the energy density of the universe, Ω. For $\Omega > 1$ the universe is spherical, and parallel lines eventually intersect. For $\Omega < 1$ the universe is hyperbolic, and parallel lines diverge. For $\Omega = 1$ the universe is flat or Euclidean, and parallel lines remain parallel. [5]

finite size. If $\Omega < 1$, then $kappa = -1$ and the universe is hyperbolic with parallel lines eventually diverging. A hyperbolic universe expands indefinitely. Figure 3.2 demonstrates the effects on geometry for these different scenarios.

3.1.2 The Big Bang Theory

If the galaxies are moving away from each other, then, if time is reversed, they are flying towards each other. Therefore, some time in the past, all matter in the universe appeared to originate at a point. The birth of this point was called the Big Bang.

During the Big Bang, the universe expanded and cooled into a predominantly hydrogen plasma. This plasma acted as a thermal black-body, hosting a population of photons with a Maxwell-Boltzmann distribution characterized by the temperature of the plasma. As the universe continued expanding and cooling, the hydrogen plasma combined with free electrons to become neutral hydrogen roughly 300,000 years after the Big Bang. The neutral hydrogen no longer interacted strongly with the black-body photons, leaving a primordial population

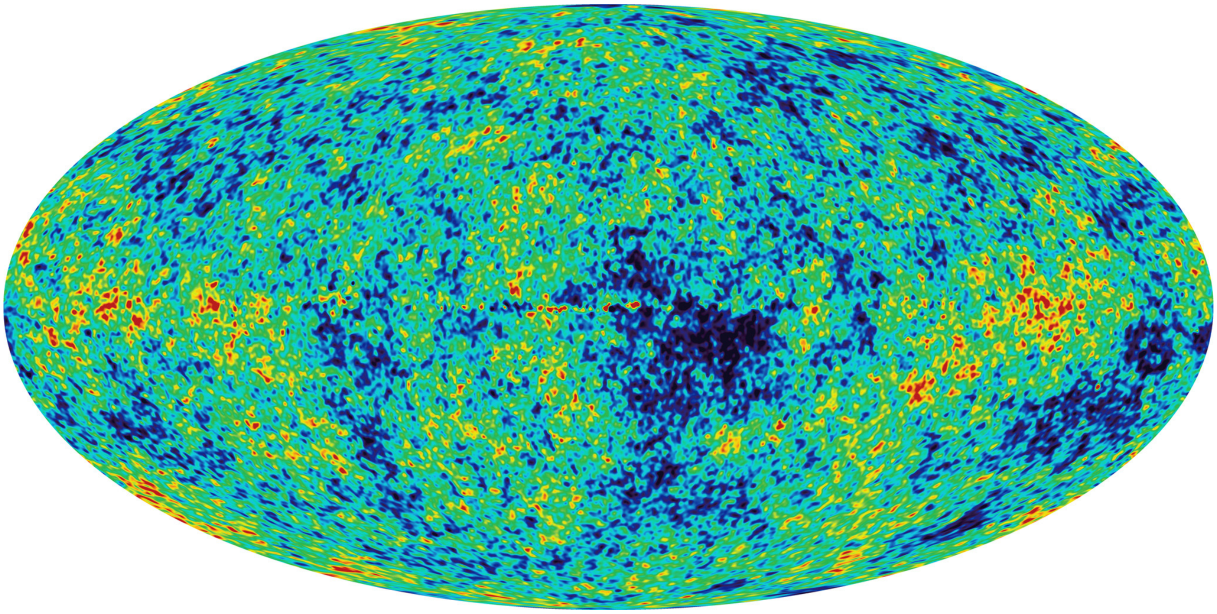

Figure 3.3: The microwave background across the sky. The colors correspond to variations in temperature with colder temperatures represented in blue and red representing hotter temperatures. The foregrounds imparted by the Milky Way and other structures have been removed as has the dipole shift from the detector's motion through the universe. The average temperature of the microwave background is 2.725 K with RMS variations of 18 μK. [5]

of photons with a black-body temperature coinciding with the recombination temperature of hydrogen ($\sim$ 3000 K). These photons are able to propagate without much scattering through the universe. Today, these observed primordial photons are the highly red-shifted afterglow of the Big Bang, the "microwave background". The microwave background was first identified in 1964 by Penzias and Wilson [27] and is shown in figure 3.3.

The most accurate measurement of the microwave background to date comes from the Wilkerson Microwave Anisotropy Probe (WMAP), a space based telescope operated at the Earth-Sun L2 Lagrange point [5]. By measuring the size and intensity of the temperature variations or "anisotropies" of the microwave background across the sky, WMAP studied the properties of the early universe. The size and intensity of the temperature variations are governed by the dynamics of the hydrogen plasma present during the early universe. The early universe contained perturbations that dispersed through this plasma as acoustic waves. The relative proportions of photons, baryons, and dark matter changed the dispersion and

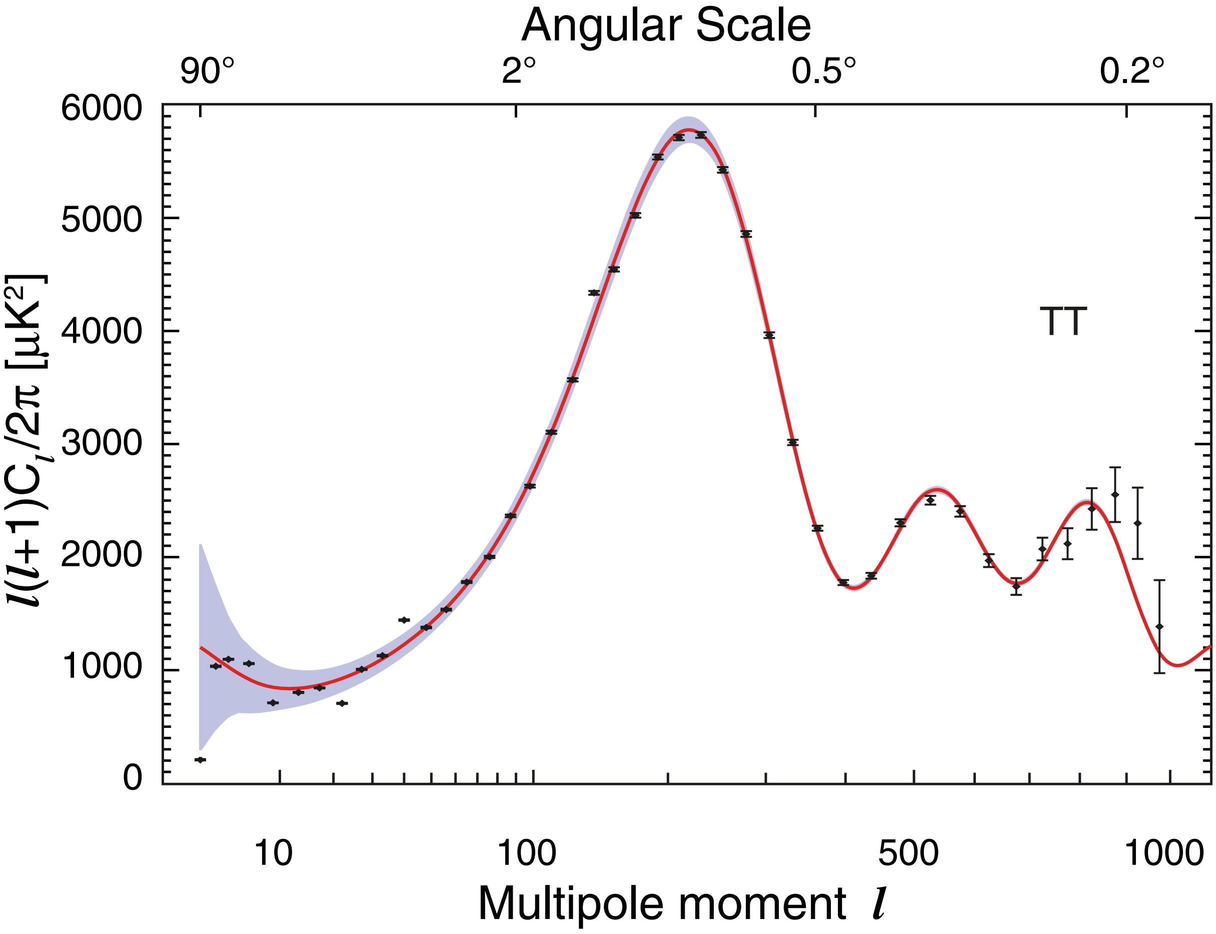

Figure 3.4: The multipole expansion of variations in the microwave background. The vertical axis is the intensity of variations. The horizontal axis is the multipole moment, with corresponding angular size given above. The black dots are the data points with associated error bars. The red line is the theoretical fit and shaded gray region the associated uncertainty. The size and location of the peaks in this plot are governed by the relative proportions of baryons, photons, and dark matter during the early universe. [5]

propagation of these acoustic waves, leaving an imprint on the microwave background of the relative proportions of photons, baryons, and dark matter present during the early universe. By measuring the angular size and intensity of anisotropies, shown in figure 3.4, WMAP determined that the universe was flat ($\kappa = 0$), with a total energy density $\Omega = 1.08 \pm .09$.

The microwave background has a peculiar property. Even though opposite sides of the microwave background are billions light-years apart and are not causally connected, the temperature of the microwave background varies across the sky by roughly one part per 100,000. How could two areas of the universe that have never been in contact be almost identical? This peculiarity is called the horizon problem. A good solution to the horizon problem is provided by "cosmic inflation". Inflation stipulates that our observable universe was once causally connected and very small. During the Big Bang, this small region of space underwent a period of superluminal expansion and became larger than the observable universe, producing the uniform microwave background. While no direct evidence of cosmic inflation has been found, it remains perhaps the most compelling solution to the horizon problem.

3.2 The ΛCDM model

Analogous to the Standard Model of particle physics, cosmologists have developed a consensus cosmology model that agrees well with most observations. The current, consensus cosmological model is named the Λ Cold Dark Matter model (ΛCDM). The ΛCDM model became well established during the late 1990's, when astronomers attempted to measure the Hubble constant at long distances with type Ia supernova. Type Ia supernova have well characterized light curves, which plot brightness over time. It happens that the shape of the light curve establishes the energy output for a type Ia supernova, allowing them to be used as "standard candles". A standard candle has a known energy output, so its distance is inferred by its brightness. By measuring the brightness and red-shift of type Ia supernova, the Hubble constant, H_0, was measured as a function of distance. It was discovered that the universe was accelerating in expansion, requiring a non-zero Λ (figure 3.5), or cosmological constant. The combination of type Ia supernova measurements, WMAP, and Baryon Acoustic Oscillations[1] have determined the overall composition of the universe to unprecedented accuracy. The largest component of the universe, 73% of the total energy density, is Λ's vacuum pressure named "dark energy". Only about 5% of the universe's energy density is

---

[1] Baryon Acoustic Oscillations are the same sound waves in the early universe, but measured by telescope surveys. The distribution of galaxy and galaxy clusters leave a trace of for the scale and spacing of density fluctuations in the universe. While the microwave background is a snapshot from 300,000 years after the big bang, Baryon Acoustic Oscillation surveys can measure structures in the universe over the last 12 billion years of galactic evolution.

normal matter or “baryons”. The remaining 23% is “cold dark matter” (CDM).[2]

3.3 The Discovery of Dark Matter

While the ΛCDM model requires a universe dominated in dark matter, the story of dark matter is much older than modern cosmology. As the first cosmological models were being formulated, the first hints were found of a hidden component of the universe.

3.3.1 Early Evidence

The first evidence of dark matter was discovered in the 1930’s with two separate observations, one at kiloparsec scales and one at megaparsec scales. Jan Oort studied the red-shifts of local stars. The stars’ motions implied a galactic disk three times heavier than that implied by counting the masses of the observed stars [28]. In an unrelated study, Fritz Zwicky studied the red-shifts of galaxies within galactic clusters. His 1933 paper applied the virial theorem to the Coma cluster of galaxies (figure 3.6). His measured ratio of gravitationally-implied mass to light was 500× what would be expected if stars solely made up the mass of the cluster [29]. These inconsistencies in gravitationally implied mass and luminous mass were largely ignored by the scientific community. The sense was that these discrepancies were either systematic errors or were from unseen non-luminous baryonic matter such as brown dwarfs and hydrogen gas.

3.3.2 The Dark Matter Revolution

The first systematic and compelling evidence for dark matter was discovered in spiral galaxies’ rotation curves, the rotational speed versus distance from the galactic center. If the

---

[2] Dark matter with non-relativistic velocity during the early universe is called “cold”. While extremely uniform, the early universe contained many small density fluctuations. Cold dark-matter settled into these fluctuations and provided a positive feedback for structure formation. In this way, CDM accelerated small-scale structure formation, leading to an early universe filled with small galaxies. These small galaxies merged and grew to become larger galaxies and eventually galaxy clusters. Computer simulations with CDM develop structures that closely match those seen in astronomical surveys.

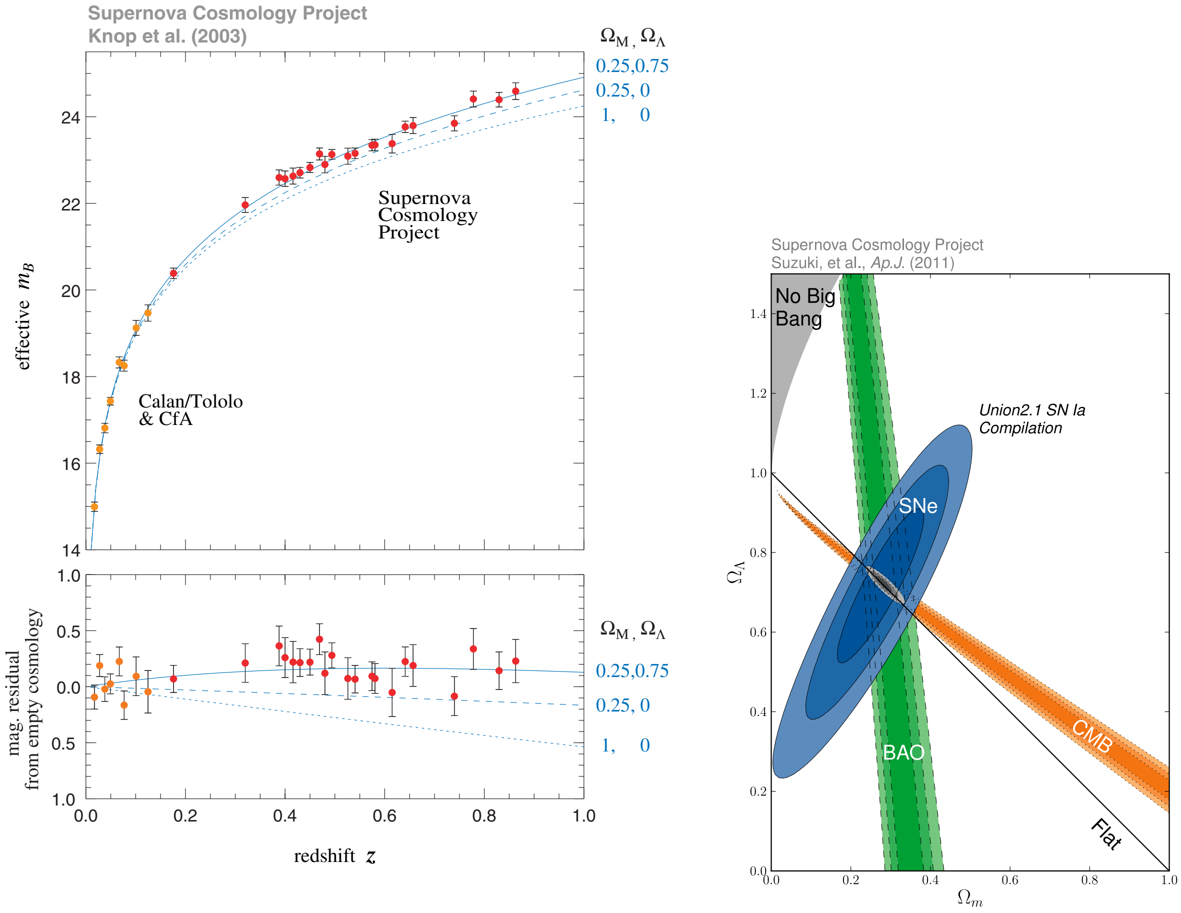

Figure 3.5: Left: A plot of effective magnitude of type Ia supernova versus redshift. The type Ia supernova fit a curve with a corresponding $\Omega_\Lambda = 0.75$. Since type Ia supernova are standard candles, their absolute magnitude is calculable from their light curves. The effective magnitude, corrected for dust and absolute magnitude, is linearly related to distance. Far away, type Ia supernova look brighter than they should in the flat, cosmological constant free, universe expected at the time of discovery. This result was the first to produce a dark energy dominated model of the universe, called ΛCDM. Right: The ΛCDM model is reinforced by redundant measurements. The vertical axis is the cosmological constant content of the universe. The horizontal axis is the matter content of the universe. Three independent measurements over-constrain our universe's composition. The WMAP (CMB) and supernova (SNe) show that we live in a flat, dark matter dominated universe. Surveys of large scale structure development (BAO) create an independent measurement that overlaps with the supernova and WMAP result.

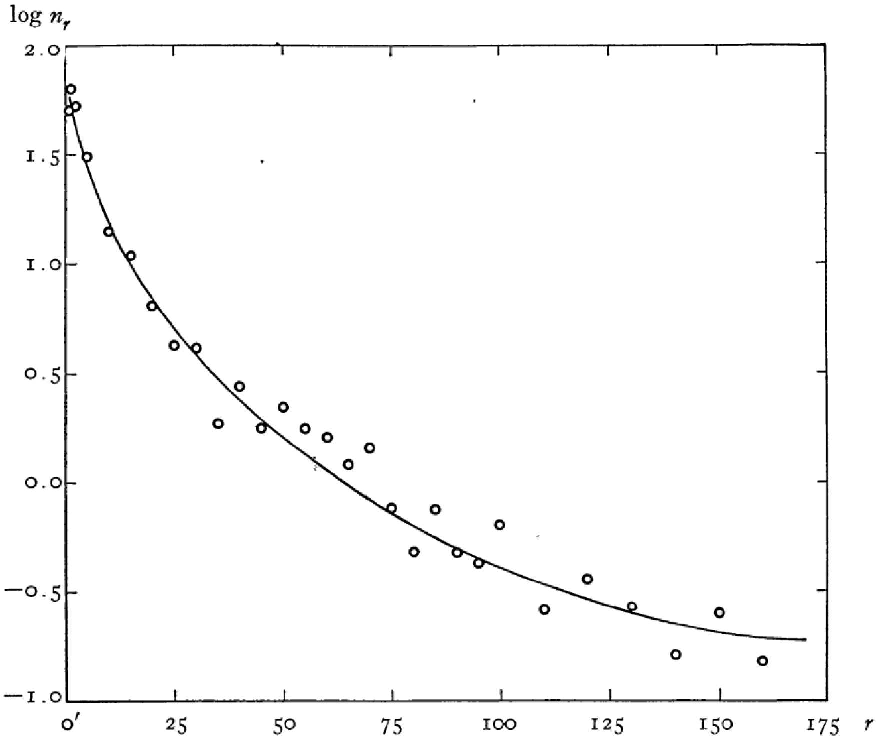

FIG. 4.—Counts of nebulae in the Coma cluster

Figure 3.6: Coma Cluster's distribution of galaxies versus their angle from the center of the cluster, r in minutes of arc. More galaxies are located at the center of the galaxy cluster and the distribution follows a line consistent with a well virialized cluster. Combining this data with the velocity distribution of the galaxies yields a virial mass. When compared to the implied mass from the combined luminosity of the galaxies, Zwicky found a $500x$ discrepancy. [29]

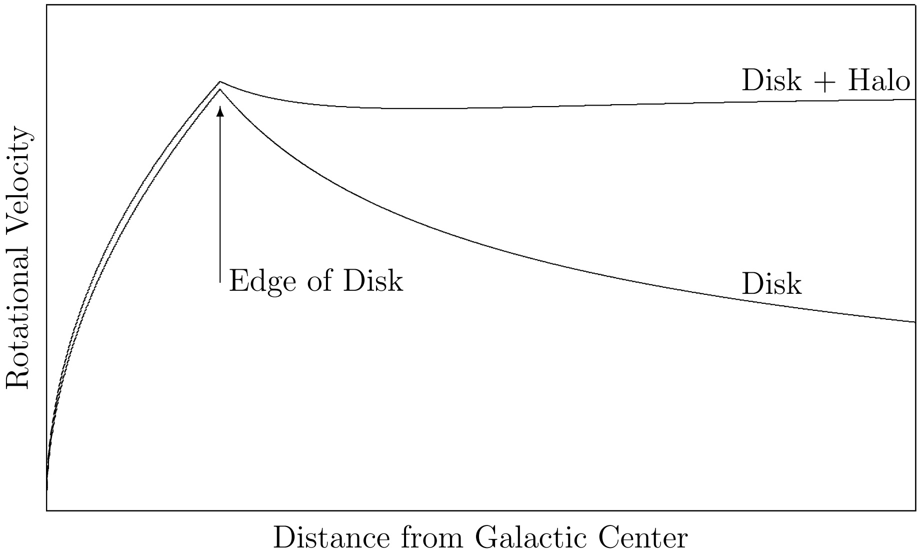

Figure 3.7: The rotation curves of two toy galaxy models. The horizontal axis is distance from galactic center. The vertical axis is rotation speed. The first model is a galaxy with a disk of uniform density. The rotation curve rises inside the galaxy, then falls off outside the galaxy. The second model is the same as the first but includes a diffuse halo of matter. Again, the rotation curve rises inside the galaxy, but remains flat outside of the galaxy.

mass of a galaxy was distributed according to the observed luminous stars, then most of the mass in a galaxy would be concentrated in the galaxy's bright core and disk. The resulting rotation curve would rise sharply within the galaxy then fall off outside the galaxy, like the Keplarian rotation curve of our solar system. If instead, the majority of the mass of a galaxy was in an extended, diffuse, and invisible dark-matter halo, then the galaxy's rotation curve would not fall off as quickly, but remain relatively flat with all radii rotating at roughly the same velocity.

With optical astronomy, only the optically luminous components of galaxies are accessible. As figure 3.7 illustrates, the rotation curve of the luminous galactic disk alone, which is dominated by baryonic matter, is mostly unaffected by the inclusion of a dark-matter halo. The brightness of the nearby Andromeda galaxy allowed for the optical measuring of the rotation curve beyond its bright disk, but measuring the rotation curve much beyond the bright, baryon dominated disk was not possible.

In the 1960s, radio astronomers began measuring spiral galaxies' rotation curves using neutral hydrogen's 21 cm wavelength spectral line, allowing spectroscopic measurements beyond the optical disk of galaxies. This new technique allowed for the systematic observation of rotation curves for many spiral galaxies. By the early 1980s, dozens of spiral galaxy's extended rotation curves had been measured (figure 3.8), and all these curves were non-Keplarian [30]. These rotation curves imply that spiral galaxies have large, diffuse halos of dark-matter. Today, there are thousands of measured spiral-galaxy rotation curves, and none match the Keplarian model: all require a dark-matter halo [31].

Of course the most conservative hypothesis about the gravitationally inferred dark-matter is that it is made of normal, baryonic matter, and no extensions of the Standard Model of particle physics are necessary. Since the most numerous stars are also the least massive, this model suggests that there are enough sub-stellar, non-luminous objects, or Massive Compact Halo Objects (MACHOs), to constitute all of the dark matter. It has been determined, however, that MACHOs cannot constitute all of dark matter for two reasons. The simplest reason is that micro gravitational lensing surveys, which look for the brightening of stars when objects pass in front of them, failed to detect enough MACHOs to account for a significant fraction of dark matter [32]. Furthermore, the density of baryons is measurable from its imprint on the early universe's evolution.

Baryon Density

During the Big Bang, the universe contained a hot plasma of quarks and gluons. This plasma cooled and formed the hadrons that eventually become the atomic nuclei in the universe. The process of forming light elements during the Big Bang is called Big Bang Nucleosynthesis (BBN). Nuclear and particle physics allows for the accurate calculation of the relic abundances of ^{2}H, ^{3}He, ^{4}He, and ^{7}Li compared to the relic abundance of ^{1}H from the baryon to photon ratio, the number of light neutrino species, and the Hubble constant. The cosmological parameter that BBN is most sensitive to is the baryon to photon ratio or equivalently the baryon density, Ω_{Baryons}. In particular, since ^{2}H is quickly burned

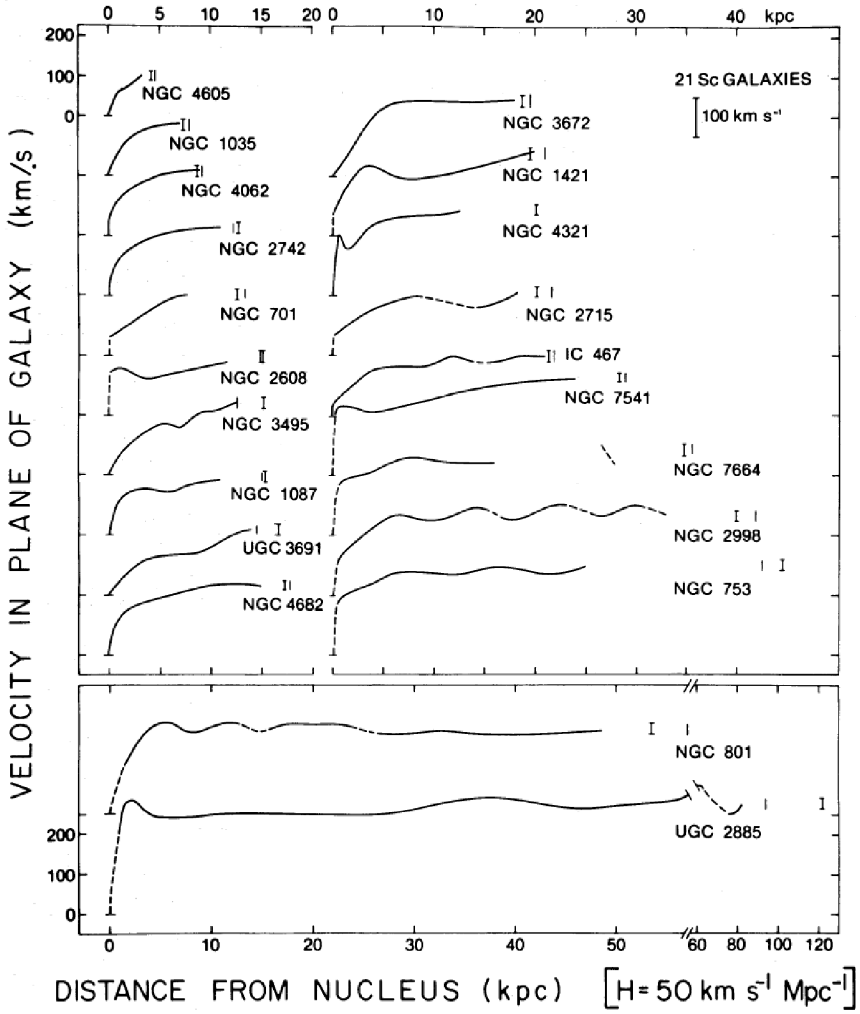

Figure 3.8: The rotational velocity curves for 21 spiral galaxies. The velocity of each galaxy is plotted against the distance from the galaxy center. None of the rotation curves follow the expected Keplarian falloff outside of their visible disk. The flat rotation curves indicate that the entire galaxy is rotating at the same speed independent of distance from the galactic center. This implies that the galaxy's mass is diffuse and not concentrated at the luminous components. [30]

in stellar fusion and is not produced by stars, most deuterium is left over from the Big Bang. Measuring the ^{2}H abundance in high red-shift gas clouds produces the most sensitive determination of Ω_{Baryon}. As shown in figure 3.9, the measurements of relic abundances of ^{1}H, ^{2}H, ^{4}He (Y_p in the figure), and ^{7}Li each produce independent measurements of the baryon to photon ratio which statistically agree with one another. Furthermore, the relic ^{2}H abundance produces the most sensitivity measurement of baryon density of roughly 4% of the critical density ($\Omega_{\mathrm{Baryons}} h^2 = 0.0205 \pm .0018$) where $h := \frac{H}{100} \frac{MPc}{km/s}$ is the reduced Hubble constant with a value of roughly 0.7. Clearly $\Omega_{\mathrm{Baryons}}$ is too small to account for the dark-matter density, $\Omega_{\mathrm{Dark\ Matter}} h^2 = .1138 \pm .0045$ measured by WMAP [5]. WMAP also independently measured the baryon density to be in agreement with BBN's measurement ($\Omega_{\mathrm{Baryons}} h^2 = 0.0226 \pm .0006$). Dark matter cannot be made of baryons.

3.4 Dark Matter Particle Candidates

After the systematic discovery of dark matter in the 1980s, particle theorists quickly began proposing potential dark-matter particle candidates. Table 3.1 shows the candidate list from Kolb & Turner's *The Early Universe* [34] in 1990. Similarly to MACHOs and baryons discussed previously, many other dark-matter candidates were eventually ruled out. As the field of dark matter candidate particles became more limited over the last two decades, three candidates have persisted: sterile neutrinos, WIMPs and axions.

3.4.1 Neutrinos as Dark Matter

The neutrino is a Standard Model particle that has been proposed as a dark matter candidate [35]. However, the 13.7 billion year history of structure formation in the universe suggests otherwise. If dark matter is "cold", meaning it was moving non-relativistically in the early universe, it would seed smaller structures that then grow larger. If dark matter was relativistic, or "hot", like a population of primordial neutrinos would be, then smaller

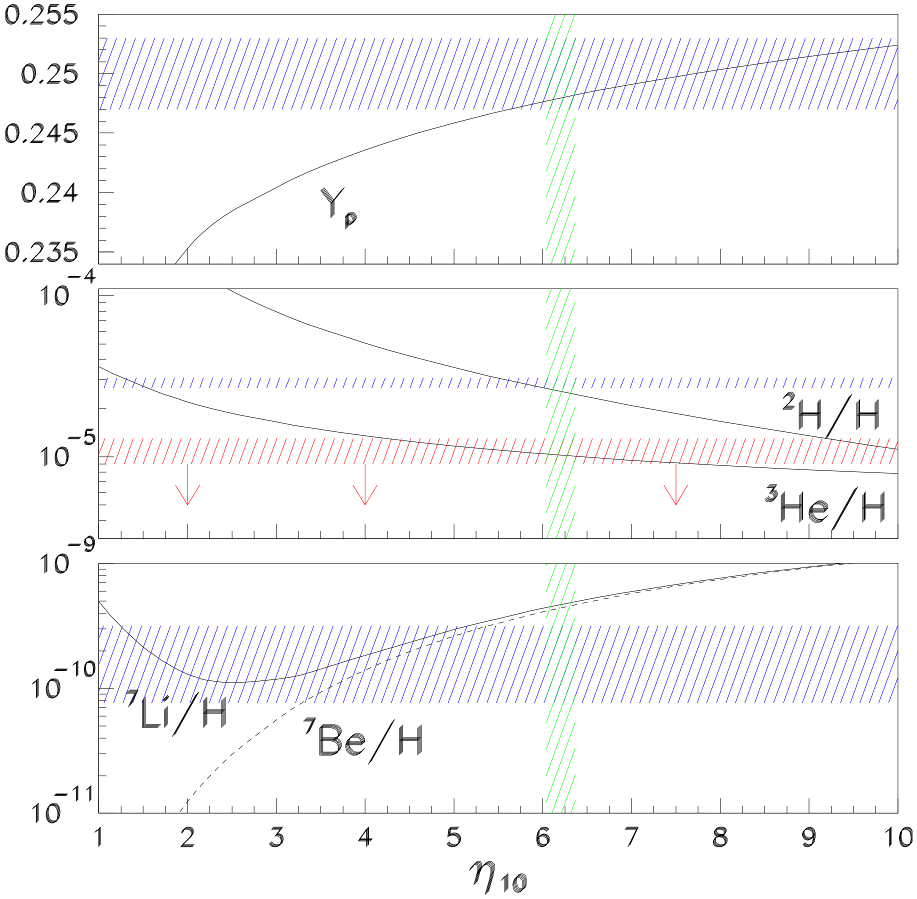

Figure 3.9: The relic abundances of light elements from the Big Bang. Values are divided by the hydrogen abundance to be unitless. The horizontal axis is the baryon to photon ratio. The horizontal hatched regions are the 1-σ wide spectroscopically measured primordial abundances of light elements. The vertical hatched region is the 1-σ baryon to photon ratio from the WMAP. The black lines are the theoretically predicted values for the 3 light neutrinos of the Standard Model. Except for Lithium, the theory lines pass through the intersection of the spectroscopically measured relic abundances with the WMAP measured baryon to photon ratio. At 2-σ, all measurements are consistent. [33]

Suspect Relic	Mass	Origin (t, T)	Abundance (cm^{-3})
Invisible Axion	10^{-5} eV	10^{-30}sec, 10^{12} GeV	10^{9}
Light Neutrino	30 eV	1 sec, 1 MeV	100
Photino, Gravitino	keV	10^{-4} sec, 100 MeV	10
Photino, Sneutrino, Neutralino, Axino, Heavy Neutrino	GeV	10^{-3} sec, 10 MeV	10^{-5}
Magnetic Monopoles	10^{16} GeV	10^{-34} sec, 10^{14} GeV	10^{-21}
Pyrgons, Maximons, Newtorites	10^{19} GeV	10^{-43} sec, 10^{19} GeV	10^{-24}
Quark Nuggets	$\simeq 10^{15}$ g	10^{-5} sec, 300 MeV	10^{-44}
Primordial Black Holes	$\gtrsim 10^{15}$ g	$\gtrsim 10^{-12}$ sec, $\lesssim 10^{3}$ GeV	$\lesssim 10^{-44}$

Table 3.1: A dark matter candidate table from 1990 [34]. Most candidates have either been eliminated or become very unfavorable. The two prominent exceptions are the axion and the WIMP (Neutralino).

structures would develop after larger ones. The observation that the largest structures, such as galactic clusters, formed in the last few billion years while the small structures, such as stars and dwarf galaxies, formed within the first billion years suggests that dark matter is cold. Cosmological evidence requires that the sum of the masses of all neutrino flavors be less than 0.3 eV [36]. Since they are thermally produced during the Big Bang, their kinetic energy would necessarily be > 1 eV, greater than their rest mass. Big-Bang-produced neutrinos are relativistic and were "hot" dark matter instead of cold dark matter. Hence, Standard Model neutrinos cannot be cold dark matter.

Even if standard model neutrinos were produced non-thermally during the Big Bang, their fermionic nature combined with their small masses would prevent them from forming massive halos, due to a lack of available quantum states. For example, a 0.1 eV rest-mass neutrino from the Milky Way's galactic halo would have a de Broglie wavelength of roughly 1 cm and roughly 6 available quantum states, allowing for a halo density of roughly .6 eV/cc, around one billionth of the expected density.

There are ideas for non-Standard Model neutrinos. Standard Model neutrinos have left-handed chirality and interact through the weak force. A right-handed neutrino would not interact through the weak force, so it would be "sterile". A heavy, sterile neutrino is a possible dark-matter candidate. There is conflicting experimental evidence over the possibility of extra neutrinos [37].

3.4.2 Weakly Interacting Massive Particles (WIMPS)

Perhaps the most well known dark-matter particle candidate is the Weakly Interacting Massive Particle (WIMP) which arises from an idea called the "WIMP miracle". In this idea, the WIMP was pair-produced during the Big Bang and existed in thermal equilibrium with all other particle species. As the universe expanded and cooled, the WIMPs thermally decoupled, leaving a large primordial WIMP population. If the WIMP has a mass greater than 10 GeV and weak interaction cross sections, the relic WIMP density closely matches that

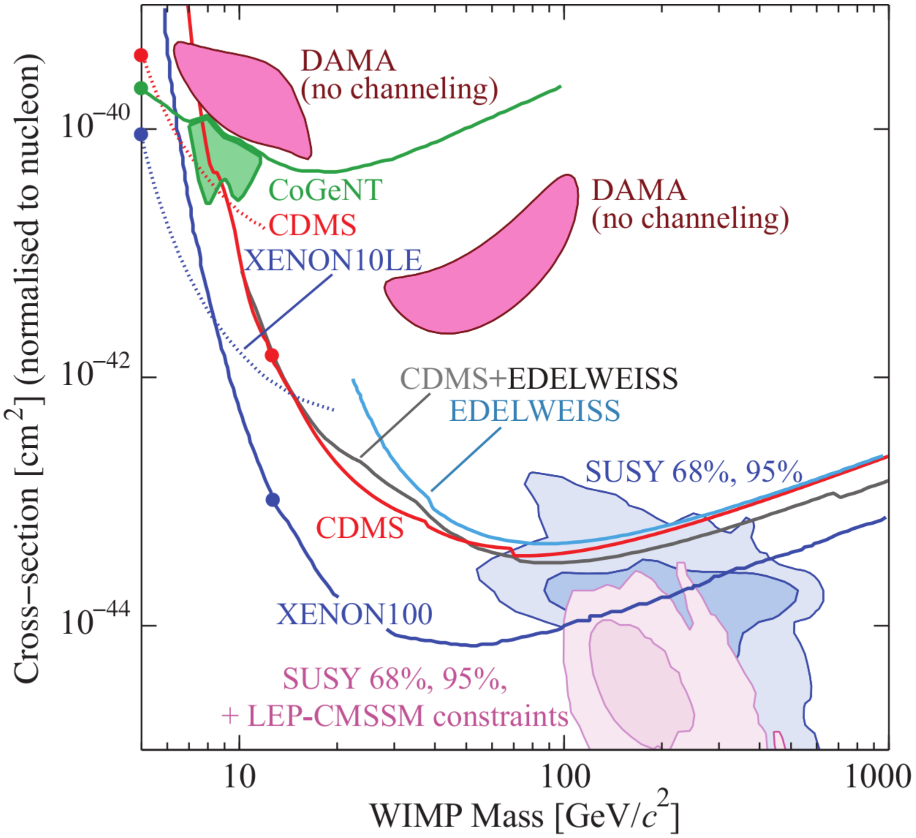

Figure 3.10: Spin-independent cross-section versus mass for WIMP dark matter. Lines are exclusion limits from various experiments. The solid, shaded regions at the top are detected signals or excesses, but more sensitive experiments have excluded them. The lower shaded regions are regions predicted by different classes of SUSY models. [38]

currently observed for dark matter [38]. One particle physics motivation that produces a particle with WIMP-like properties comes from an idea called SuperSymmetry (SUSY).

A class of extensions to the Standard Model, SuperSymmetry (SUSY) doubles the number of fundamental particles by introducing partners to all of the fundamental Standard Model particles. These new particles, called “super-partners”, are much heavier and obey opposite spin-statistics than their standard model partners. The “neutralino” is the lightest, stable super-partner and has expected mass and coupling that roughly agree with the WIMP miracle [38], allowing for the possibility of SUSY WIMP dark matter. However, detection of a SUSY WIMP is complicated by the SUSY WIMP’s substantially unbounded mass and coupling.

Dozens of experiments are currently searching for SUSY WIMPs [38]. At the basic level, the Large Hadron Collider (LHC) is searching for evidence of SUSY. Direct searches for SUSY WIMP dark matter search for the rare collisions of WIMPs with atoms. The results of the most sensitive such searches are shown in figure 3.10. While the mass and coupling of SUSY WIMPS are relatively unconstrained, the light Higgs mass and the relic density of dark matter require that some models of SUSY be very fine tuned to produce a WIMP miracle [39]. This work doesn't further investigate WIMP dark matter.

3.4.3 Axions

The invisible axion, introduced in the previous chapter, is a highly compelling dark-matter candidate.[3] The invisible axion couples to many of the Standard Model particles, but these coupling strengths are generically incredibly weak. For instance, a 1 μeV axion would have an extraordinary long lifetime of perhaps 10^{54} seconds. It happens that the invisible axion's mass and couplings are rather tightly constrained, allowing for the possibility of a definitive search for dark-matter axions which would either detect or exclude the possibility of a dark-matter axion with high confidence.

There are a variety of proposed Axion-Like Particles (ALPs) that don't have the QCD axion's well defined mass-coupling relationship [40]. While any number of ALP models provide a viable dark-matter candidate, their unconstrained masses and couplings complicate experimental searches. This work doesn't further investigate ALP dark matter. All references to axions are strictly QCD motivated axion models.

3.5 Axion Dark Matter

The invisible axion, described in the last chapter, is a compelling dark-matter candidate. Axion dark matter is produced during the Big Bang from the PQ symmetry breaking. While

---

[3] Amusingly referred to by Michael Turner as the "thinking man's" dark matter candidate

the temperature of the universe is above the PQ symmetry breaking scale, f_a, the U$(1)_{PQ}$ symmetry is preserved. Once the universe cools below f_a, the U$(1)_{PQ}$ symmetry breaks from the effects of instantons on the QCD vacuum. These effects produce an effective potential which dynamically forces the CP violating phase, $\overline{\theta}$, to zero. This potential, on cosmological scales, produces an equation of motion for $\overline{\theta}$ identical to that of a damped pendulum [34]:

$$\ddot{\overline{\theta}} + 3H(t)\dot{\overline{\theta}} + m_a^2 sin(\overline{\theta}) = 0 \tag{3.3}$$

where $H(t)$ is the Hubble constant and m_a is the mass of the axion. The energy of the oscillating $\overline{\theta}$ field is manifested as zero-temperature dark-matter axions. With roughly a factor of 2 uncertainty, the relic density of axions today, Ω_a, is given by [34]:

$$\Omega_a h^2 \simeq .7 \left(\frac{10\mu eV}{m_a}\right)^{7/6} \left(\frac{\overline{\theta}_i}{\pi}\right)^2 \tag{3.4}$$

Whether cosmic inflation occurs before or after the PQ symmetry breaking produces different constraint for equation 3.4 in the initial $\overline{\theta}$ angle, $\overline{\theta}_i$. For PQ breaking before inflation, $\overline{\theta}_i$ can be any value between $-\pi$ and π, with an expected value of $\overline{\theta}_i = \frac{\pi}{2}$, which generates the expected dark matter density, $\Omega_a = 0.23$, when $m_a \simeq 14\mu$eV. Since $\overline{\theta}_i$ varies across the entire universe, $\overline{\theta}_i$ could happen to be very small in our relatively tiny, observable universe, allowing for $m_a << 14\mu$eV. However, ultra-light axions require that the majority of the unobservable universe is saturated with axions, with our relatively small, observable universe being special. Since life could not exist in most of a universe with ultra-light axions, these models are said to be anthropic axions [41].

For PQ breaking after inflation, $\overline{\theta}_i$ is a field of different values throughout our universe, with an RMS value of $\overline{\theta}_i = \frac{\pi}{\sqrt{3}}$, which generates the expected dark matter density when $m_a \simeq 18\mu$eV. However, there are models where topological defects occur in the $\overline{\theta}_i$ field which produce additional dark-matter axions [34]. These models have a wide range of additional dark-matter axion production, ranging from roughly $0 - 100\times$ of equation 3.4. Topological defect axion production allow for much heavier dark-matter axions with masses of up to 10 meV [42].

3.5.1 Overview of Dark-Matter Axions

Figure 3.11 shows the current bounds on the axion mass and coupling from experimental, cosmological, and astronomical observations. The QCD axion's coupling strength is mostly restricted to the narrow range between the DFSZ or KSVZ model lines.[4] Also, the axion's mass is rather tightly constrained. If the axion is too massive, it becomes too strongly coupled and its effects would be detectable in a variety of astronomical measurements. Observation of White Dwarf Cooling and supernova 1987a together limit the axion's mass to be less than roughly 10 meV. If the axion is too light, roughly 10 μeV, too much dark-matter axions would have been produced in the Big Bang, as governed by equation 3.4. However, this lower bound can be substantially lowered by applying an anthropic argument.

The only known experimental technique to detect dark-matter axions, which is described in the next chapter, detects the rare decays of axions from the Milky Way's dark-matter halo. This is the method used by ADMX, where the axion's total energy is converted into a microwave photon. The axion's total energy depends on the local velocity dispersion of the Milky Way's dark-matter halo. Since the dark-matter halo is not directly observable, the local velocity dispersion is approximated by a halo model.

3.6 The Milky Way's Dark-Matter Halo

While astronomical observations have determined that spiral galaxies like our Milky Way are dominated dark matter, the detailed structure of galactic dark matter halos is difficult to determine. By measuring rotation curves, the enclosed mass is determined. However, whether

---

[4] Finely tuned axion models can eliminate axion-to-photon coupling entirely. However, since the axion was proposed to solve a fine tuning problem, a finely tuned axion without any anthropic motivations is a strange construct.

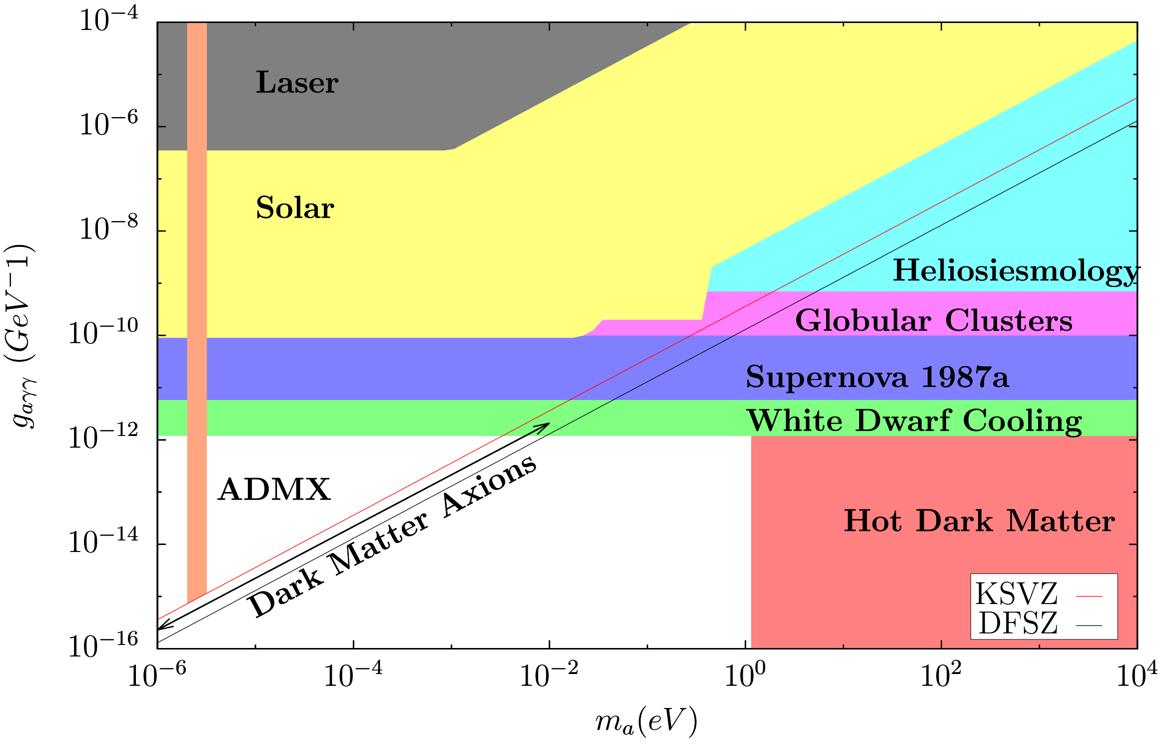

Figure 3.11: Bounds on the axions. The vertical axis represents the axion to two photon coupling strength. The horizontal axis is the axion mass. The KSVZ and DFSZ lines represent benchmark axion models. Various experimental, cosmological and astronomical results have produced limits on the axion mass and coupling. The white region is where axions have not been excluded. Between the KSVZ and DFSZ lines within this white region is the possible parameter space of dark-matter axions. The hot dark matter and supernova 1987a limits only apply to KSVZ model axions while the white dwarf cooling limit only applies to DFSZ model axions. A cold dark matter bound at roughly 10 meV only applies if Peccei Quinn symmetry breaking occurs after inflation. Note that axions are tightly constrained in coupling and loosely constrained in mass to the range of 1 μeV to 10 meV. Any axion within these bounds could account for all of the dark matter in the universe.

the dark matter halo is rotating, spherical, oblate, or triaxial has yet to be measured in our own halo with high confidence [43]. Since we are within the Milky Way, any measurement of the Milky Way's dark-matter halo has large, systematic errors [44] [45] in total halo mass and local dark-matter density. Our best approximations for the Milky Way's dark-matter halo structure come from galaxy-scale, high resolution, dark-matter, n-body simulations, such as Via Lactia [46], with results shown in figure 3.12, GHALO, and Aquarius. However, these detailed simulations lack baryons, an important component of galaxy evolution, especially in the baryon dominated disk of our galaxy. More recent studies have found that baryons may play a vital role in dark-matter halo formation [47].

3.6.1 Structure Formation

Dark-matter simulations attempt to replicate the 13 billion year formation of galaxies. They assume a ΛCDM universe with only cold dark matter particles. Collisionless particles can be described as an evolving sheet in position-velocity phase-space, stretching and folding as the universe ages. During the early universe's evolution, small density fluctuations seeded structure formation. As larger structures formed, the dark matter sheet began to fold into spiral structures [48], as shown in figure 3.13. At the center of a large and old dark matter structure, like a galactic halo, are a large number of folds. The high density of folds at the galactic center result in a phase space nearly indistinguishable from a thermal distribution. In a cold dark-matter filled universe, large structures form from the merging of smaller structures. This results in large structures, like the Milky Way's halo, having very complex phase-space distributions [49].

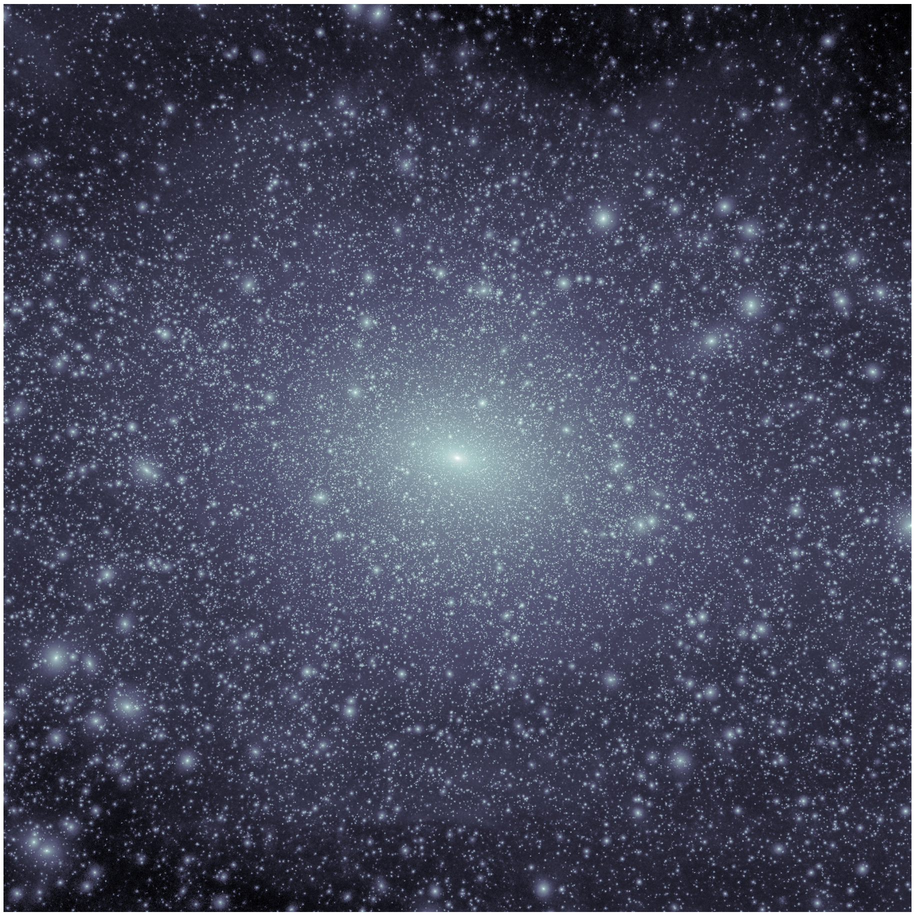

Figure 3.12: Results of the Via Lactia simulation that attempts to recreate the Milky Way from the Big Bang. The image shows the hierarchy of many small to few large structures that likely formed the Milky Way's halo. Since dark matter is non-dissipative, it tends to form persistent, diffuse structures, unlike gas which can cool and collapse into stars and collide inelastically.

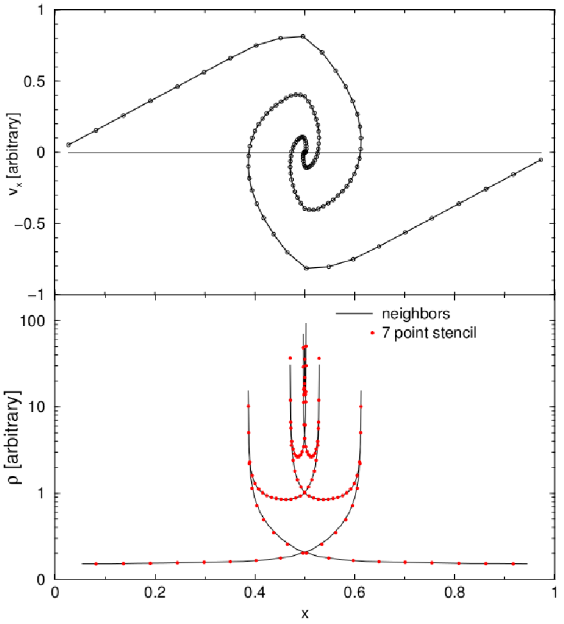

Figure 3.13: A model of cold dark matter halo formation. The upper plot shows a 2D slice of velocity, v, as a function of position phase space, x. It shows how the dark matter flows fall through each other without interaction. The sheet of phase space, a line in this projection, curls up as it forms the galactic halo. The lower plot shows density, ρ as a function of position, x, for each flow. Outside of the halo, there is only one flow of low density. Inside of the halo, at certain points, the flows slow and turn around, becoming caustics of large overdensity. [48]

3.6.2 The Isothermal Model

At the simplest level, dark-matter halos can be approximated as an isothermal sphere. While an isothermal sphere model has significant issues[5] and halos are better described by either an "NFW" profile or an "Einasto" profile [50], the isothermal sphere has an easily calculable velocity dispersion. As shown in figure 3.14, the local velocity dispersions of 6 n-body, Milky Way sized, dark-matter simulations are shown to be in rough agreement with that of an isothermal sphere. Therefore, the isothermal sphere model is used as the basis for the analysis described in chapter 5.

3.6.3 The Dark Disk

Simulations that include a disk of baryons, like that found in spiral galaxies, tend to produce a disk of dark matter [7]. In these models, a merging subhalo's dark matter is drawn into the baryonic disk, producing a dark disk. The presence of a dark disk would substantially alter the the local velocity dispersion compared to dark-matter only simulations like those of figure 3.14. Figure 3.15 shows the local velocity distributions for several dark disk models. While a very dense dark disks appear to be observationally unfavored [52], a light dark disk remains theoretically motivated. However, the parameters for such a dark disk are largely unbound, preventing a targeted search. Instead, a toy dark disk model is investigated in chapter 5 to demonstrate the possibility of enhanced dark-matter detection sensitivity.

3.6.4 Fine Structured Dark Matter

As discussed earlier, the relic dark matter between galactic halos is a dense or "cold" sheet in velocity-position phase space. When this relic dark matter first falls into a halo, it forms a flow. A simple model of this first infall flow is investigated in chapter 5. Furthermore a cold flow will form a high overdensity, called a caustic, at its closest point to the center of

---

[5] The rotation curves of spiral galaxies have excluded the isothermal halo model: dark matter halos have significantly lower density around their galactic cores than the isothermal sphere model predicts.

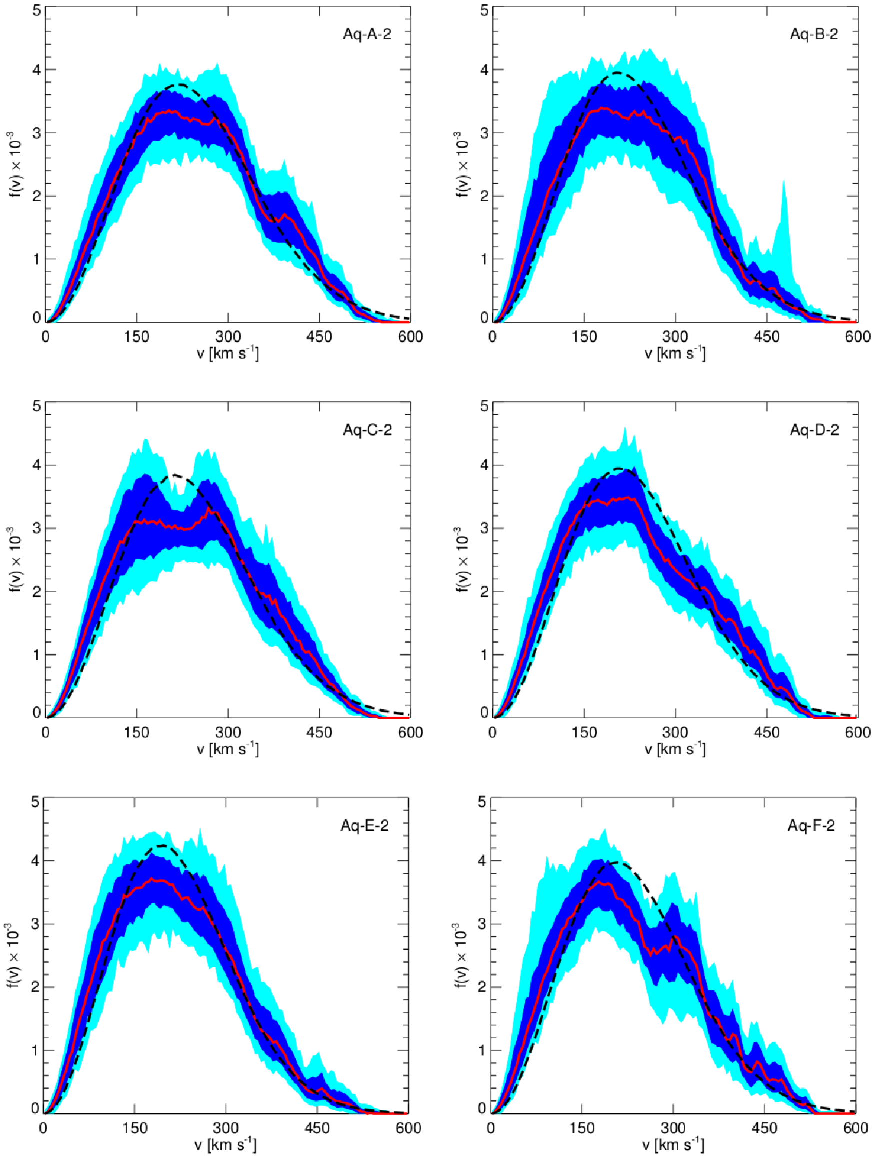

Figure 3.14: Local dark matter velocity dispersions from 6 Aquarius simulations. The fractional densities, f(v) are plotted as a function of velocity, v, in red. The shaded regions represent 1σ (dark blue) and 2σ (light blue) error bounds. The dashed black line is a Gaussian fit to an isothermal halo. Each halo shows some deviations from an isothermal distribution. The upper right plot, Aq-B-2, shows a dense narrow spike near 450 km/s from a merging subhalo. [51]

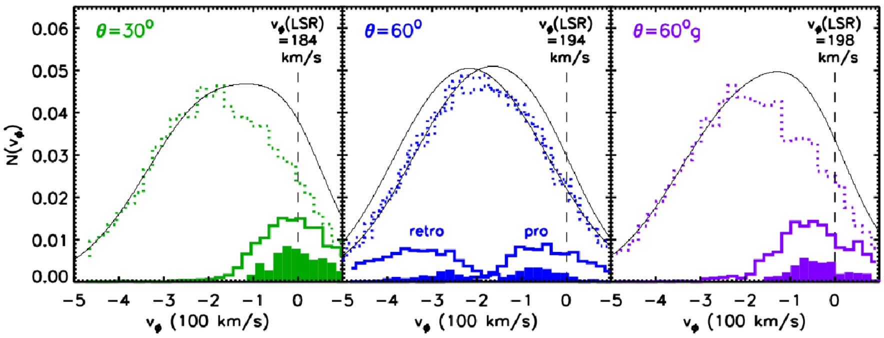

Figure 3.15: Local velocity dispersion in a dark disk model. The dark shaded regions are the contributions from the dark disks formed by a single subhalo merging at various angles to the galactic baryon disk. The resulting dark disks are significantly less dispersed than the main halo, shown as a dotted line. [7]

the galaxy. In the "Caustic Ring" model, the symmetry of the galaxy produces a system of overdensities corresponding to the number of times each flow has fallen into and out of the galaxy. According to [8], the earth happens to be near the n=5 caustic ring. The caustic ring model is investigated further in chapter 5.

In the ΛCDM universe, structures like the Milky Way form from merging with smaller structures. The density of these smaller structures may create chaotic caustic structures. The Aquarius n-body simulations model the formation and evolution of Milky Way sized dark-matter halos. Figure 3.16 shows the radius-radial velocity phase space in an Aquarius dark-matter halo. The folding of phase space is clearly visible, as is the hierarchical population of structure size. In this simulation, the location and density of each caustic were tracked for every dark-matter particle. From the result of this simulation, there are expected to be very few dense caustics in the sun's neighborhood, as shown to figure 3.17. The most massive flow that has an expectation value of 1 is only .005% of the total halo density. Chapter 5 investigates how to search for signals from these caustics.

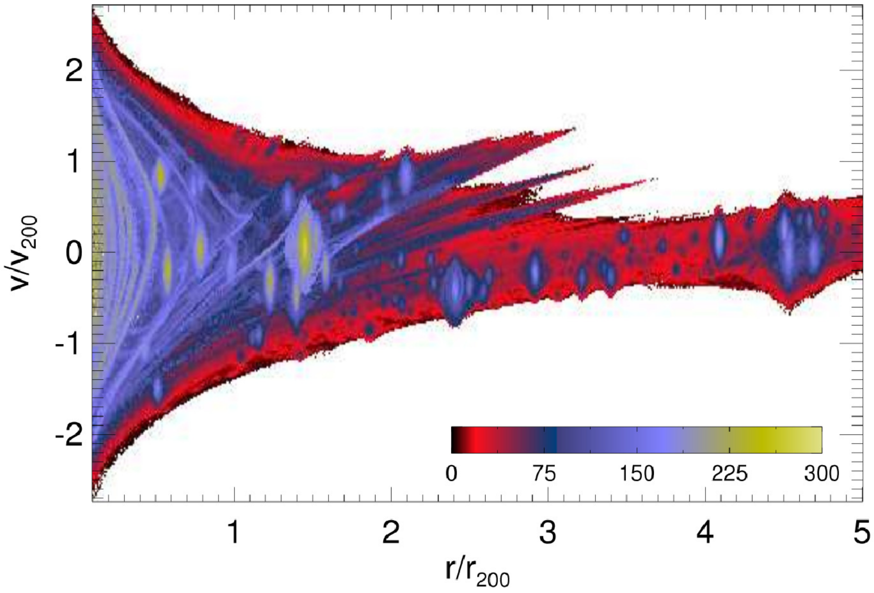

Figure 3.16: A 2D slice of the phase space of a halo formed in the Aquarius simulations. The scaled velocity, v, is plotted against the scaled distance from the galactic center, r. The coloring is the number of infalls or caustics each dark matter particle has experienced. Small halos have quick orbital periods, so the dark matter is highly wound. [49]

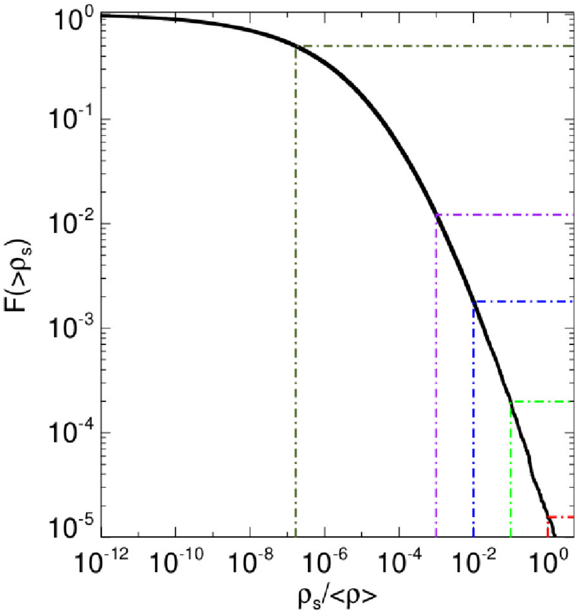

Figure 3.17: The distribution of caustic flows, F, as a function if the fractional density of a flow ρ_s, to the density of the bulk halo, $< p >$. While there are thousands of flows of tiny densities, there are very few dense flows. There is only a 20% chance of a local flow of .01% halo density and an expectation of 1 flow of .005% halo density. [49]

Chapter 4

The Axion Dark Matter Experiment (ADMX)

As discussed in chapter 3, the available window for a dark-matter axion's mass is from 1 μeV to 10 meV. Also, detecting dark-matter axions is highly challenging, since they interact so incredibly feebly with normal matter and radiation. Only one experimental technique, the axion haloscope [54], has the potential to be sensitive to dark-matter axions in this window. The largest and most sensitive axion haloscope is the Axion Dark Matter Experiment (ADMX). This detector provided data for this thesis.

This chapter describes the ADMX apparatus. First, the concept of the axion haloscope is described, as well as its specific ADMX implementation. The chapter then details the key components of ADMX, including the recent introduction of a microwave SQUID amplifier. Finally, the software used to control ADMX and acquire data is described.

4.1 The Axion Haloscope

The interaction of axions with photons is incredibly weak: a 1 μeV axion would have an expected lifetime of around 10^{54} seconds, considerably longer than the age of the universe. Therefore, it is nearly impossible to directly detect the photons from the very rare sponta-

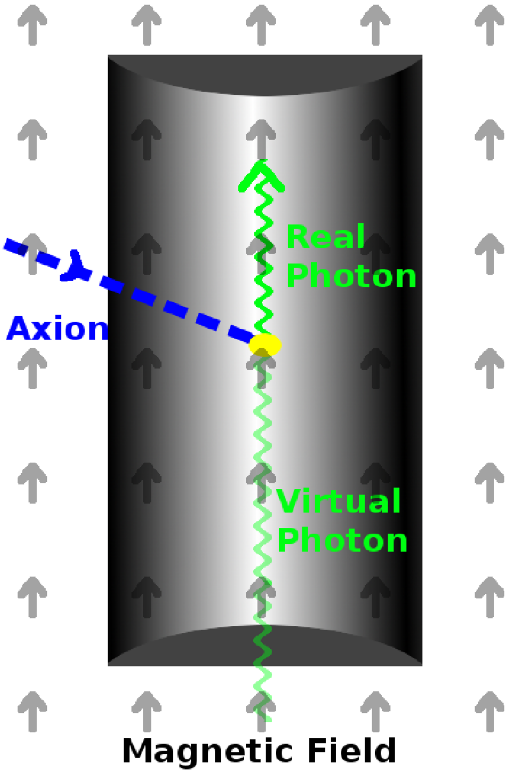

Figure 4.1: A sketch of the axion haloscope concept. An Axion from the Milky Way's halo collide with a virtual photon associated with a static magnetic field, allowing the axion to decay into a single, real photon while conserving momentum. The high density of states in a cavity mode of the same frequency as the decay photon increases the probability of axions to scatter and convert into photons.

neous dark-matter axion decays.[1] A better method to detect axions is via a detector called an axion haloscope. It greatly accelerates the decay rate of axions within the detector from the Milky Way's dark-matter halo. An axion haloscope consists of a strong, static, magnetic field threading a microwave cavity, illustrated in figure 4.1. In an axion haloscope, massive axions scatter off the magnetic-field potential, thereby converting into massless microwave photons while conserving momentum. This process is familiar in particle physics as the reverse of the Primakoff effect, where high-energy photons directed into a static target potential produce neutral pions.

The axion-to-photon conversion rate, governed by equation 2.7, depends on the applied field magnetic, with the conversion rate scaling quadratically with the field strength. Even with a multi-Tesla applied field, the conversion rate by itself is too small to detect. However, by surrounding the magnetic volume with a high quality-factor (Q) resonant, microwave cavity, the conversion rate is enhanced by the factor Q when the cavity resonant frequency is tuned to the outgoing microwave photon energy. This is because the conversion rate is proportional to the square of the oscillating electric field strength inside the cavity, which in turn is proportional to the Q of the cavity. The resulting conversion power, though minute, is detectable in principle. Appendix A derives the power developed in an axion haloscope. Summarizing that appendix, the power developed in a axion haloscope with typical ADMX parameters is:

$$P = 3.17 \times 10^{-21}\ \text{Watts} \left(\frac{V}{200\ \text{l}}\right)\left(\frac{B}{8\ \text{T}}\right)^2\left(\frac{f_{nlm}}{.5}\right)\left(\frac{\rho_a}{0.3\frac{\text{GeV}}{\text{cc}}}\right)\left(\frac{g_\gamma}{0.97}\right)^2\left(\frac{Q}{100000}\right)\left(\frac{\nu_a}{750\ \text{MHz}}\right) \tag{4.1}$$

where V is the cavity volume, B is the magnetic field, f_{nlm} is the form factor of the cavity mode and magnetic field shape(discussed in section 4.3.2), ρ_a is the local mass density of axions, g_γ is the axion-to-photon model-dependent parameter (0.97 for KSVZ, -0.36 for

---

[1] Some telescope searches have looked for the spontaneous decay of axion dark matter within large, nearby galaxy clusters. However, they are only sensitive to heavy, eV scale, axions that are already excluded for other reasons. [53]

DFSZ), ν_a is the frequency of the axion-to-photon conversion signal, and Q is the quality factor of the cavity.

As shown in equation 4.1, the expected power developed inside the cavity from axion-to-photon conversion is indeed tiny. Some of this power is extracted from the cavity in order to be measured. The optimal way to extract this power is from a near-critically-coupled field probe[2]. At critical coupling, the field probe extracts half of the power from the cavity while the other half of the power dissipates inside the cavity's resistive surfaces. Since power inside the cavity only persists for half as long when critically coupled as opposed to uncoupled, the Q of the cavity at critical coupling is $\frac{1}{2}$ that of the uncoupled cavity. The power extracted by the field probe is then amplified and processed by a low-noise, microwave receiver chain.

4.1.1 Haloscope Sensitivity

The two primary sources of noise backgrounds in the haloscope arise from the first amplifier in the receiver chain and from the cavity walls. The walls of the cavity produce a spectrum of thermal blackbody photons, Johnson noise, which, up to emissivity considerations, is identical in power spectrum density to the white noise generated by a resistor at the same temperature as the cavity walls. The first amplifier in the receiver also produces white noise[3], but as discussed later, this noise depends, among other things, on details of the amplifier technology. The total noise power underneath a typical axion signal is:

$$P_N = 5.52 \times 10^{-20}\ \text{Watts} \left(\frac{T_{\text{Cavity}} + T_{\text{Amplifier}}}{4\ \text{K}}\right)\left(\frac{B_a}{1000\ \text{Hz}}\right) \tag{4.2}$$

where T_{Cavity} is the physical temperature of the cavity, $T_{\text{Amplifier}}$ is the Johnson-equivalent noise temperature for the first amplifier in the receiver chain, and $B_a \simeq \nu_a * 10^{-6}$ is the expected axion signal bandwidth, which is halo-model dependent. This model dependence is

---

[2] While the performance (scan rate) of a haloscope is improved with an over-coupled field probe compared to a critically coupled probe, the difference is slight and achieving an arbitrary coupling is experimentally difficult compared to critical coupling.

[3] Over the bandwidth of interest.

explored in the next chapter. In order to reduce the noise to low enough levels, a haloscope must operate cryogenically and employ the quietest of microwave amplifiers.

The sensitivity of an axion haloscope is characterized by the signal-to-noise ratio (SNR), given by the ideal radiometer equation:

$$SNR = \frac{P_S}{P_N}\sqrt{B_a t_{\text{int}}} \tag{4.3}$$

Where $P_S = \frac{P}{2}$ is the signal power extracted from the cavity at critical coupling, P_N is the noise power, and t_{int} is the integration time. In order for the axion signal to be detectable with good confidence, the SNR needs to be large, ~ 10. If the axion's mass was *a priori* known, then SNR could be improved by simply integrating long enough at that known frequency. However, the axion's mass is not known *a priori*. An axion haloscope therefore has to scan over a wide range of possible axion masses. The scan rate for an reasonable axion haloscope, assuming an SNR of 10, is:

$$R = 82\ \frac{\text{Hz}}{s}\left(\frac{B_w}{10\ \text{kHz}}\right)\left(\frac{P_s}{1.59\times 10^{-21}\ \text{W}}\right)^2\left(\frac{1000\ \text{Hz}}{B_a}\right)\left(\frac{4\ \text{K}}{T_{\text{Cavity}} + T_{\text{Amplifier}}}\right)^2 \tag{4.4}$$

where $B_w = \frac{\nu_a}{Q}$ is the cavity bandwidth. In principle, a reasonable haloscope could either detect or reject an optimistic KSVZ-model axion over a range of GHz within a year, but would take around 100 years to do the same with the more weakly-coupled DFSZ-model axion. Clearly, an axion haloscope with better than "reasonable" performance is required for a reasonable experiment. This work demonstrates a stepping stone towards such a haloscope.

4.2 The development of Axion Haloscopes

Shortly after the axion haloscope was proposed in 1985, two groups: one from University of Florida [55] and one a joint effort from the University of Rochester, Brookhaven National Lab, and Fermi National Accelerator lab [56], built experiments based on the axion-haloscope

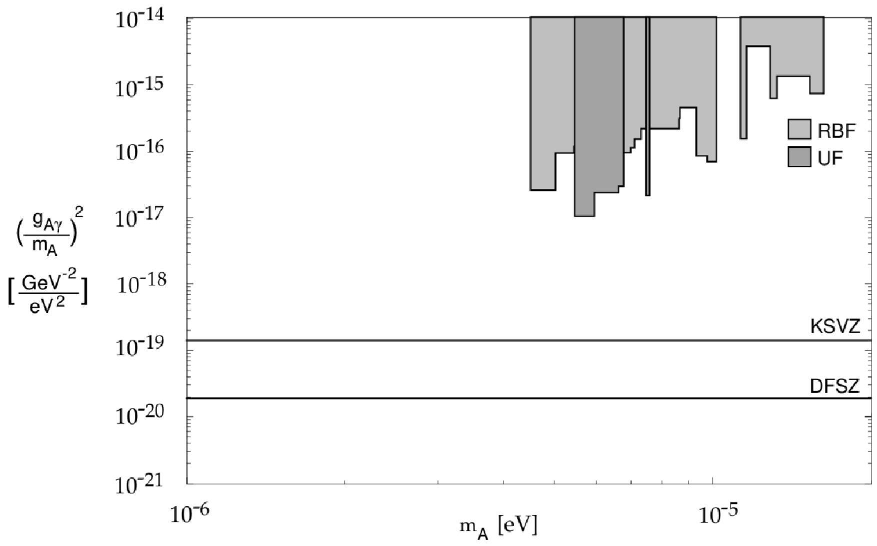

Figure 4.2: The exclusion regions for early axion haloscopes. The vertical axis is the squared strength of the axion to photon coupling constant scaled by axion mass. The horizontal axis is the axion mass. Note the two QCD axion models, represented by the horizontal DFSZ and KSVZ lines, are unattainable in a reasonable timeframe with the technologies used in the Rochester-BNL-FNAL(RBF) or University of Florida(UF) experiments. To be sensitive to the more optimistic KSVZ line, these experiments would have had to run for roughly 10,000 times longer. [57]

principle. These centimeter-scale experiments did not have the necessary sensitivity to detect plausible axion dark matter over a significant mass range. However, these experiments demonstrated the feasibility of the haloscope technique. The exclusion limits from these early experiments are shown in figure 4.2. If the axion happened to be over 10× more strongly coupled than the optimistic KSVZ-model axion, then these searches could have made a discovery.

4.2.1 Introduction of the Axion Dark Matter eXperiment (ADMX)

Those two demonstrator axion haloscopes led to the development of a much larger axion haloscope called the Axion Dark Matter eXperiment (ADMX). ADMX primarily improves sensitivity over these earlier experiments by scaling up the size of the experiment, thereby increasing B^2V in equation 4.1 by almost 100×. Most other parameters remain similar, including the noise temperature in equation 4.2, yielding an experiment roughly 100× more sensitive than the demonstrator haloscopes. The first implementation of ADMX ran from 1995 to 2005 and was the first axion haloscope to successfully set exclusion limits for KSVZ model axions in the axion mass range of 1.9 μeV to 3.36 μeV. In order to be sensitive to DFSZ model axions without requiring hundreds of years of operation, ADMX needs to improve its sensitivity by 10× or scan rate by 100×.

Looking at equations 4.3 and 4.1, one avenue of improvement would be to further increase B^2V. However, since the magnet of ADMX is the most expensive single component, roughly \$1 million dollars in 1993, a larger magnet would be very expensive and likely require ADMX to operate at lower frequencies, which are perhaps less theoretically favorable. Another possibility would be to improve the Q of the cavity, but no technology has been demonstrated to improve the Q substantially for a microwave cavity in a strong magnetic field[4]. The remaining path to improvement is by reducing the system noise temperature. Since the creation of ADMX, there has been a revolution in microwave amplifier technology. Quantum-noise-limited amplifiers cooled by a helium dilution refrigerator could improve the sensitivity of ADMX by up to 100× at reasonable costs. This is the obvious upgrade path for ADMX

Use of a Superconducting QUantum Interference Device (SQUID)

After the initial 1995 to 2005 run, ADMX was upgraded to include a Superconducting QUantum Interference Device (SQUID) configured as a microwave amplifier. The SQUID amplifier, when cooled below 100 mK, has roughly 40x less noise than the best transistor-based amplifiers, such as those used in the 1995 to 2005 operation of ADMX. The noise produced by a SQUID amplifier is nearly at the minimum allowed by quantum mechanics. Although their low noise makes SQUIDs very attractive, their extreme sensitivity to magnetic fields made their incorporation into ADMX challenging. In ADMX, the SQUID amplifier is located axially 2 meters above the center of the 8.5 Tesla solenoid. In order to shield the

---

[4] The ADMX sister collaboration, ADMX-HF is currently investigating a cavity with thin film superconducting walls, which for a high profile cavity would significantly improve Q.

SQUID from the large magnetic field, a field-free volume is established around the SQUID.

From 2005 to 2008, the ADMX experiment was rebuilt with a SQUID amplifier and associated field-free volume. From 2008 to 2010, ADMX successfully ran with a SQUID amplifier. However, since ADMX was operated at the same physical temperature as the 1995 to 2005 run, there was only a modest improvement in system noise temperature. To achieve the desired $> 20\times$ improvement in noise temperature and sensitivity, ADMX is currently being upgraded to incorporate a helium dilution refrigerator to cool the cavity and SQUID.

4.3 ADMX Hardware

Figure 4.3 shows a cross-section of the hardware of ADMX. It consists of two components: the main magnet and the experimental insert. The main magnet is an 8.5 Tesla superconducting magnet welded into a 3.4 m tall cryostat. The vertically-oriented main magnet has a 0.53 m diameter warm bore that contains the removable ~ 500 kg experimental insert.

The experimental insert is composed of three sections from bottom to top: the cavity section, the bucking coil section, and the mechanical support section. The cavity section consists of the microwave cavity itself, the vacuum can that contains the cavity, and the "1 K pot" that cools the cavity, described in section 4.3.9. There are also three gearboxes that precisely move the cavity's tuning rods, the major port, and the throttle valve to the 1 K pot. The bucking-coil section includes the bucking coil system, liquid-helium reservoir, and the SQUID amplifier package. Consisting of baffles and tubes, the support section provides the structural and thermal support of the insert.

Figure 4.3 shows the three isolated vacuum spaces within the insert by color coding. The "blue" insulation space lies between the experimental insert and warm bore of the main magnet. The insulation space is typically pumped down to high vacuum ($\sim 10^{-10}$ Torr) to isolate the cryogenic components from the room temperature top plate of the insert as well

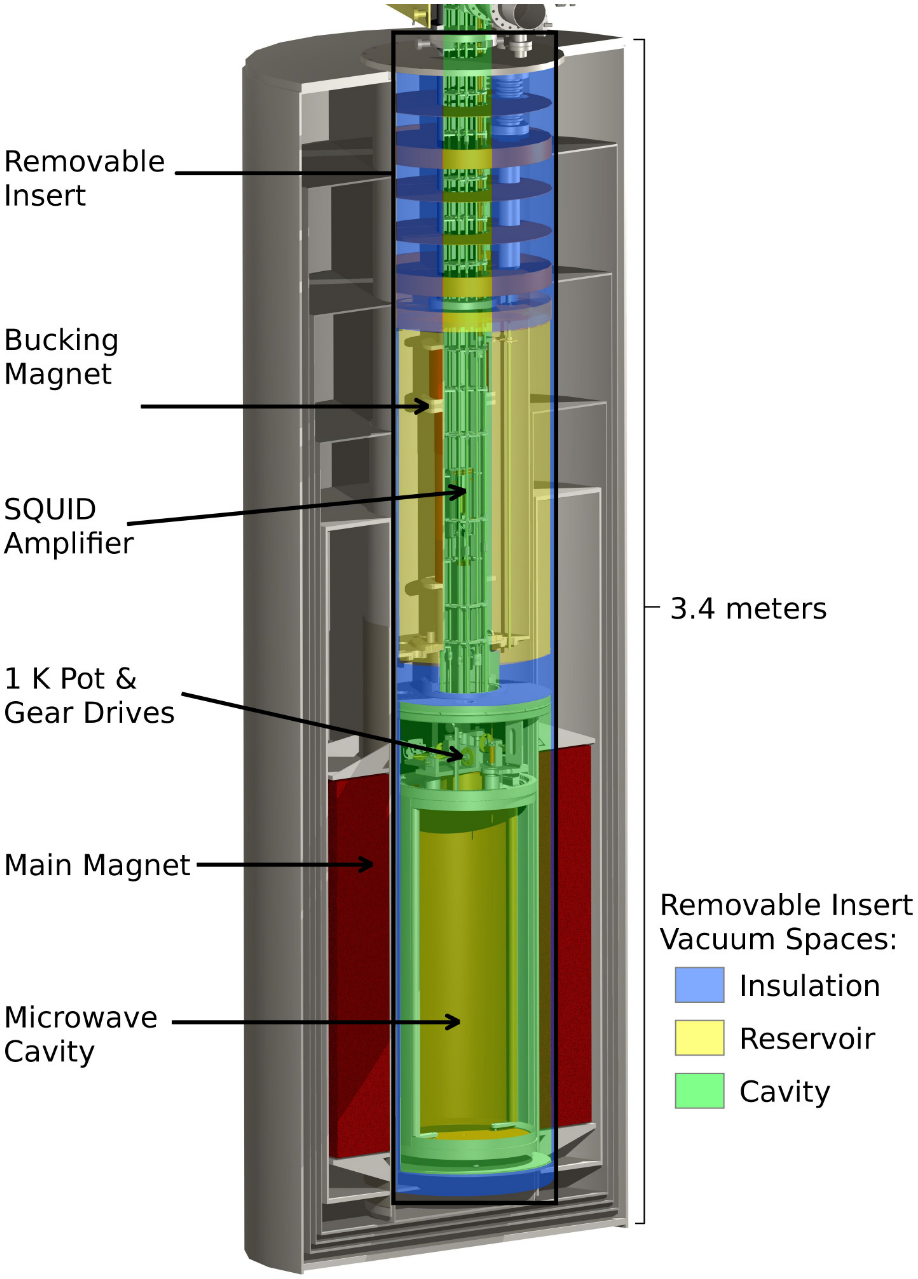

Figure 4.3: A cross-section of the ADMX experiment. There are two primary components: the main magnet and the removable experimental insert. Most of the experiment is occupied by vacuum spaces, tubes, and baffles for cryogenic operation. At the base of the insert is the copper cavity, surrounded by the large main-magnet solenoid. In middle of the insert are the bucking magnet and SQUID amplifier.

as the magnet's warm bore. The "green" cavity space contains the microwave cavity and also the SQUID amplifier and other components inside the central support of the insert. The cavity space can be operated between high vacuum, under normal running, and atmospheric pressure, during cool-down procedures and mode-crossing procedures, described later. The "yellow" reservoir space is the volume containing the insert's liquid helium (LHe) reservoir and its associated fill tube. The reservoir is maintained at atmospheric pressure. These various spaces are necessary for cooling and maintaining the experiment at liquid helium temperatures (4.2 K). The scan rate of ADMX scales inversely with the square of the cavity temperature, so cooling the ADMX cavity to LHe temperatures is essential for the ADMX search.

4.3.1 Magnet

The ADMX main magnet produced the high, static field necessary for the conversion of dark-matter axions into photons. The main magnet and its cryostat were manufactured by Wang NMR in 1993. The superconducting coil is a 1.12 meter tall solenoid with a 60 cm inner diameter, as shown in figure 4.4. The magnet winding is composed of four concentric superconducting solenoids, with the inner solenoids having progressively higher critical-current-rated wire. The 99 km of copper-stabilized niobium-titanium wire is wound around a stainless steel spool piece and potted in epoxy. The superconducting magnet alone weighs ∼6000 kg and the magnet's stainless-steel cryostat weighs ∼3000 kg.

The magnet has an inductance of 534 Henries. The rated maximum field at the center of the magnet is 8.5 Tesla at a current of 248.96 amps, with a stored energy of 16.54 MJ. The main magnet was originally designed to run in persistent mode, allowing for the leads to be removed once the magnet was charged in order to reduce cryogen consumption. However, during commissioning, the persistent switch failed catastrophically. The leads were then redesigned: instead of removable leads, vapor-cooled leads were permanently installed. The lack of a persistent switch requires that the main magnet's current be continuously

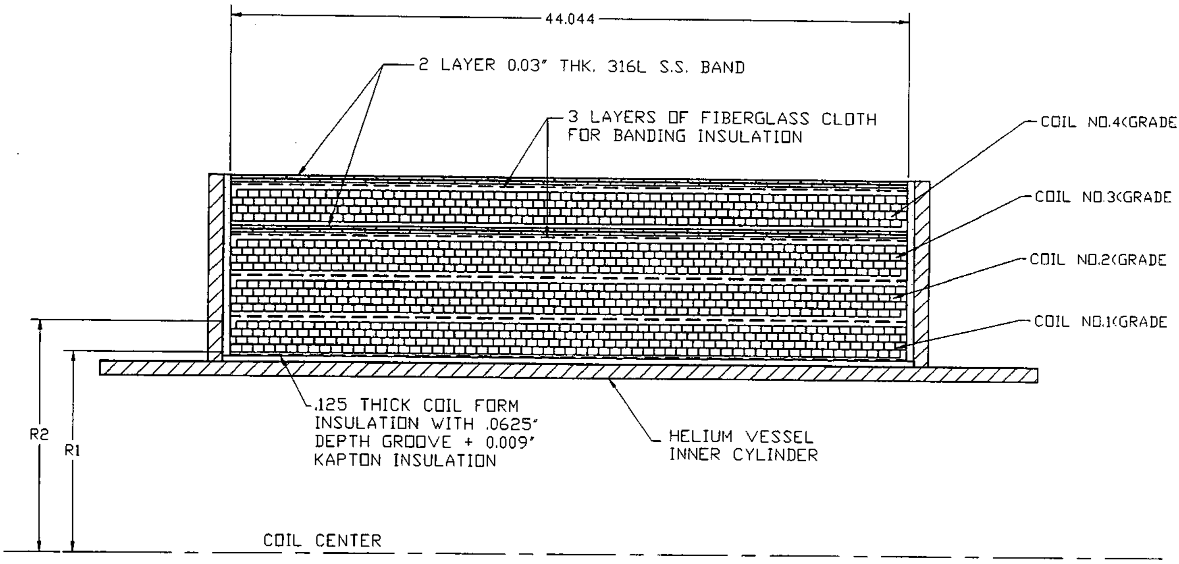

DIMENSIONS ARE IN INCHES

COIL SECT	1	2	3**	4**
R1	11.811	12.230	13.906	15.486
R2	12.230	13.906	15.427	19.416

** THIS COIL OUTER SURFACE IS BANDED WITH 2 LAYER 0.030" THICK 1/4" WIDTH 316L S.S. BAND

Figure 4.4: A horizontally-oriented cross-section of the main magnet. The main magnet is made from four concentric, superconducting solenoids connected in series.

maintained by a power supply.

4.3.2 Cavity

The ADMX cavity is where dark-matter axions would scatter off the magnetic field and resonantly convert into microwave photons. To maximize this signal, the ADMX cavity substantially fills the magnet's bore. The ADMX cavity is a large, 140 liter, copper-plated stainless steel cylinder, the inside of which is shown in figure 4.5. The cylinder is made of a tube-section forming the cavity walls plus two removable end caps. The end caps form a low-resistance connection to the walls via a knife-edge on the walls pressing firmly into the end plates[5]. The loaded quality factor, Q, of the cavity ranges from 7000 to 80000. Appendix B discusses the reason for this large range in Q. The Q of the cavity primarily depends on the resistive skin losses of the copper plating. The oscillating electric fields of the cavity

---

[5] The axion-sensitive TM_{010} mode has currents that flow between the end caps and walls. Therefore, a low-loss connection between the walls and end plates is important to the quality factor of this mode.

mode penetrate the resistive copper walls of the cavity. It's well known that for classical conductors, where the electrons behave classically, the depth of penetration is parametrized by the 1/e "skin depth" of the field penetration [58]:

$$\delta = \left(\frac{2}{\mu_c \omega \sigma} \right)^{1/2} \tag{4.5}$$

where μ_c is the permeability of the cavity walls ($\sim \mu_0$ for copper), ω is the angular frequency (roughly 2π GHz for ADMX), and σ is the conductivity of the cavity walls. The corresponding unloaded Q of an RF resonator is given by:

$$Q = \frac{\mu_0}{\mu_c} \left(\frac{V}{S\delta} \right) \times (\text{ Geometry factor } \sim 1) \tag{4.6}$$

where V is the volume and S is the surface area. At room temperature, copper has a conductivity of $6 \times 10^7 A/V$. For a 1 meter tall, 0.5 meter diameter cavity, the expected room temperature Q is roughly 20,000. At the cryogenic temperatures of the ADMX cavity, coppers with lower oxygen content have larger conductivities ($> 100\times$ larger). With such a high conductivity, the mean free path of the conducting electrons becomes larger than the classical skin depth, making equation 4.5 and equation 4.6 invalid. In this "anomalous skin depth" regime of a high frequency resonator, like the cavity of ADMX when cooled with liquid helium, the Q of the resonator becomes strongly dependent on the surface finish of the walls and less dependent on the bulk properties of the conductor [59]. For this reason, the ADMX cavity is engineered to have a very smooth and strain-free surface.

The power developed by the axion-to-photon conversions in the cavity depends on the form factor, f_{nlm}, of the cavity mode. This factor parametrizes the overlap of the external magnetic field with a cavity mode's electric field. The form factor is defined as:

$$f_{nlm} \equiv \frac{\left(\int_V dV \mathbf{E}(\mathbf{x}, t) \cdot \mathbf{B}(\mathbf{x}) \right)^2}{V B^2 \int_v dV \epsilon_r E^2} \tag{4.7}$$

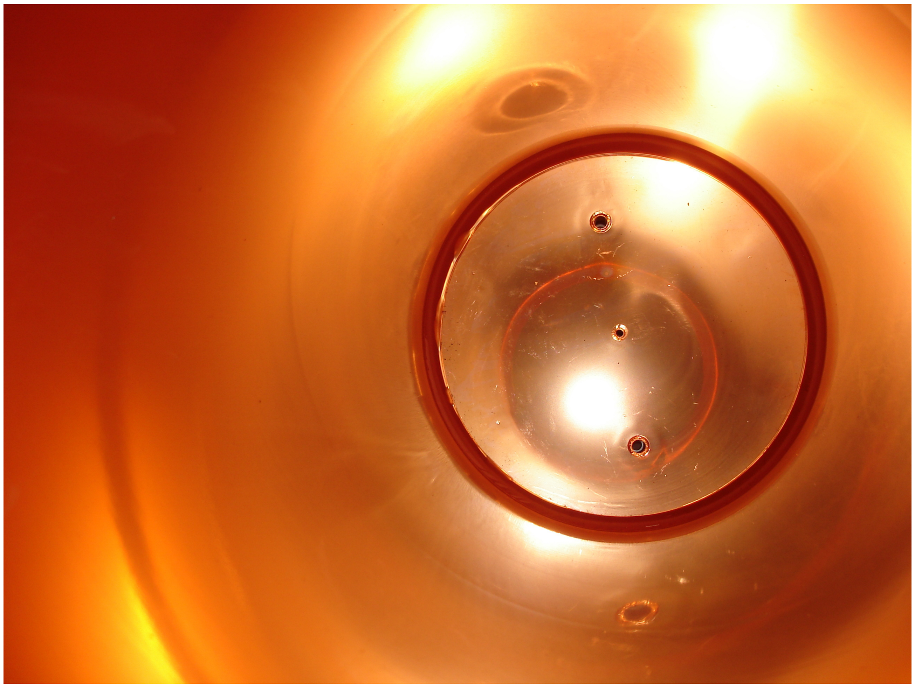

Figure 4.5: A photo of the inside of the ADMX cavity used for this thesis, with rods removed. The copper plating is optimized for high Q in the anomalous skin-depth regime.

where $\mathbf{E}(\mathbf{x}, t)$ is the electric field of the nlm cavity mode, V is the cavity volume, ϵ_r is the relative permittivity within the cavity, and $\mathbf{B}$ is the externally applied magnetic field. In ADMX, $\mathbf{B}$ is oriented more or less vertically along the cavity's axis. The shape of $\mathbf{E}$ depends on the cavity mode. For the ADMX cavity, there are, among others, transverse electric (TE_{nlm}) modes, transverse magnetic (TM_{nlm}) modes, and transverse electromagnetic (TEM_n) modes. The TE and TEM modes both lack any axial E field, resulting in negligible form factors. The axial electric field for a TM_{nlm} mode of a right, circular cylinder is [58]:

$$E_z(\rho, \phi, z) = E(t) J_m(\frac{x_{ml}}{R}\rho) e^{\pm im\phi} cos\left(\frac{n\pi z}{d}\right) \tag{4.8}$$

where $E(t)$ is the time dependent component of the field, J_m is a Bessel function, x_{ml} is the l^{th} root of $J_m(x) = 0$, R is the cavity radius, and d is the cavity height. For the cavity and magnet configuration used in ADMX, the TM_{010} mode maximizes f_{nlm} and $f_{nlm} \approx 0$ for all TM modes with $n \neq 0$ or $m \neq 0$. Therefore, only TM_{0l0} modes have substantial non-zero form factors.

In order to tune the TM_{010} mode, two copper-plated stainless steel tuning rods are mounted on rotating alumina supports inside the cavity. As illustrated in figure 4.6, rotating the rods from near the wall of the cavity to near the center tunes the TM_{010} mode from roughly 500 MHz to roughly 900 MHz. The rods are 5 cm in diameter[6]. The rods create nulls in the electric field of the cavity mode, shown in figure 4.7, effectively shrinking the cavity width and increasing the TM_{010} mode's frequency.

The rods are moved by stepper motors located on top of the experimental insert. The stepper motors are connected to long G10 shafts that drive gearboxes on top of the cavity, which in turn are connected to the alumina shafts of the tuning rods. The gearboxes consist of two anti-backlash worm gear reductions, the first 140:1, the second 300:1. Combined with the 200 steps per revolution stepper motors, the angle of the rods can be stepped by roughly 75 nano-radians. In practice, this stepping resolution allowed for tuning the cavity at roughly 100 Hz per step.

The motion of the tuning rods mostly tunes TM modes, with TE and TEM frequencies remaining nearly constant. However, when the TM_{010} mode crosses a TE or TEM mode, the modes' fields mix and share energy. This mixing degrades f_{nlm} and Q severely and complicates the analysis. As such, the axion search becomes insensitive at these frequencies. To be sensitive at these mode crossing frequencies, the cavity's permittivity is temporarily increased by filling the cavity with liquid helium. This effectively increases the cavity's size, lowering all resonant frequencies by roughly five percent. Furthermore, by only partially filling the cavity, mode crossings can be lowered by a smaller shift, up to the maximum of five percent. By lowering the frequencies of mode crossings in this manner, previously axion insensitive regions are accessible. With this technique, all of the tunable range of the TM_{010} mode is sensitive to axion-to-photon conversions. However, liquid helium is slightly lossy and is slightly more dielectric than vacuum, so Q is degraded slightly when the cavity is filled

---

[6] Larger rods would have increased the maximum tuning frequency of the cavity, but degraded Q and f_{nlm}.

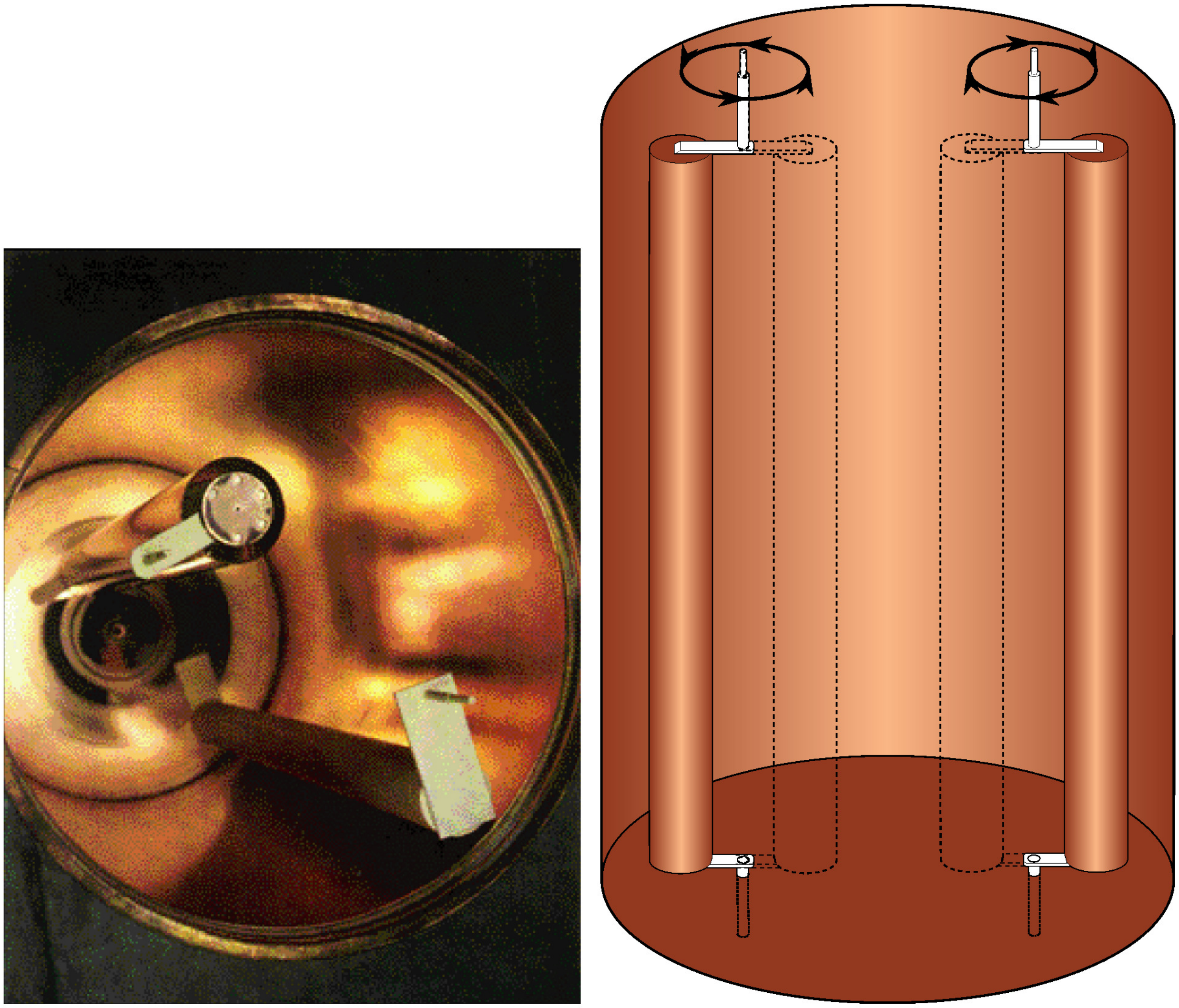

Figure 4.6: Left: a picture of the inside of an earlier ADMX cavity with tuning rods installed. Right: a sketch illustrating the tuning rods moving within the cavity. By rotating the alumina shafts of the tuning rods, the tuning rods are swung towards or away from the center of the cavity. With both rods near the center, the TM_{010} mode has a frequency of roughly 900 MHz. With both rods positioned closest to the cavity walls, the TM_{010} mode has a frequency of roughly 500 MHz.

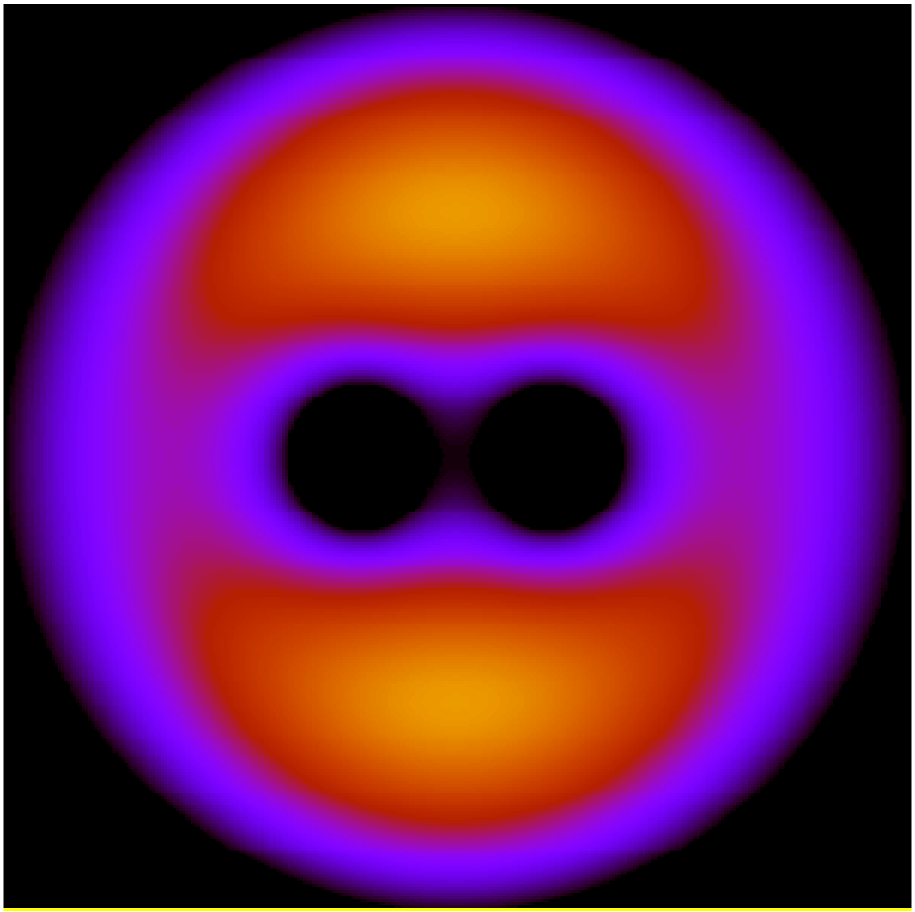

Figure 4.7: A simulation of the axial electric field at the midplane of the cavity with red regions indicating strong field, blue regions indicating weak field, and black regions with no field. The axion scattering rate in ADMX is maximized when the electric field of the cavity mode is axial and well distributed. In this configuration, the rods are near the center and the field is well distributed, producing a high form factor.

with LHe compared to when it is under vacuum. Also, if the cavity is only partially filled with LHe, the fields of the mode are slightly localized inside the liquid helium, degrading f_{nlm} slightly.

Two ports in the cavity, the “major port” and the “weak port”, located in the top plate of the cavity, allow for the extraction or insertion of RF power into the cavity. The major port consists of a movable antenna that can be inserted or withdrawn via a stepper motor attached to a linear gear drive, varying the coupling strength at the major port. Like the tuning rods, the major port’s linear drive is actuated by a stepper motor attached to a long G10 shaft which turns a 140:1 anti-backlash wormgear drive. The weak port is a fixed, short antenna that is very under-coupled to the TM_{010} mode. The weak port can inject signals into the cavity without degrading Q or extracting signal power.

To measure the TM_{010} mode’s frequency and Q, a network analyzer, illustrated in figure 4.8, measures the swept transfer function of the cavity. The transfer function is determined by injecting a tone into the weak port of the cavity and measuring the same tone’s amplitude transmitted through the major port. The frequency of the injected tone is swept across the frequency of the resonant mode. At frequencies far outside the resonant frequency of the cavity, almost none of the injected tone enters the cavity so almost none is extracted at the major port. On resonance, the injected tone enters the cavity and is extracted at the major port. The output of the network analyzer is the swept response (“transfer function”) across the cavity mode. A simulated transfer function is shown in figure 4.9. The shape of the transfer function across a cavity mode is expected to be a Lorentzian, given by:

$$TF(f) = \frac{P_{max}}{1 + 4Q^2(\frac{f}{f_0} - 1)^2} \tag{4.9}$$

where P_{max} is the peak transmitted power of the mode, f_0 is the frequency of the peak of the mode, and Q is the quality factor of the mode. As such, the recorded transfer functions of the cavity mode are fitted to a Lorentzian to determine the central frequency, f_0, and

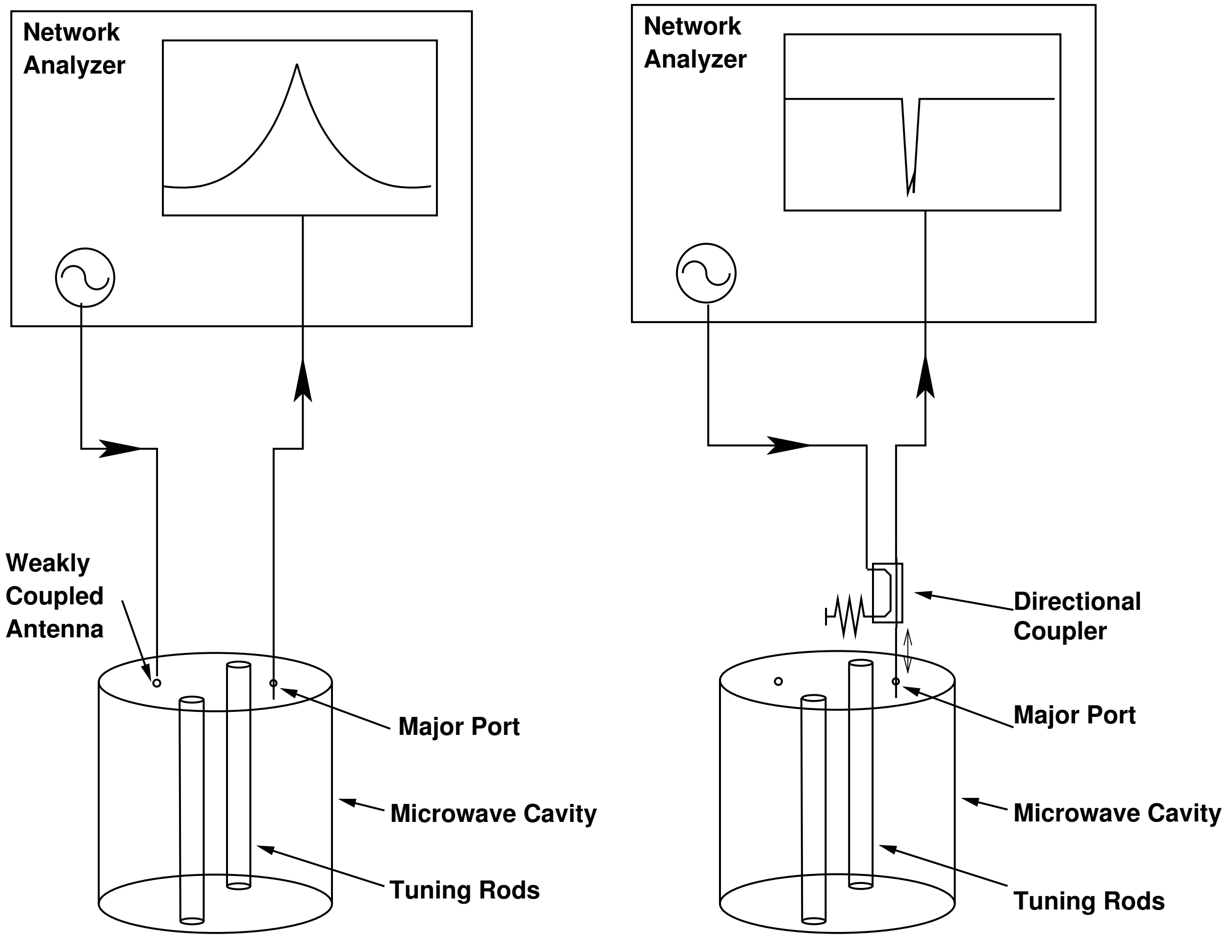

Figure 4.8: Left: The configuration for the network analyzer to measure the transfer function of the cavity. The network analyzer sends a tone to the minor port, through the cavity, and back to the network analyzer. The network analyzer measures the transmitted power across a range of frequencies, generating the transfer function of a cavity mode. The simplified plot shows the expected Lorentzian shape of the cavity mode. Right: The configuration for the network analyzer to determine if the major port is critically coupled. The network analyzer sends a tone to a directional coupler, which sends the tone towards the cavity's major port. Off resonance, all of this power is reflected off the cavity and towards the network analyzer. On resonance, when the probe is critically coupled, all of the incident power is deposited in the cavity's walls. The simplified plot shows the sharp drop in reflected power on resonance.

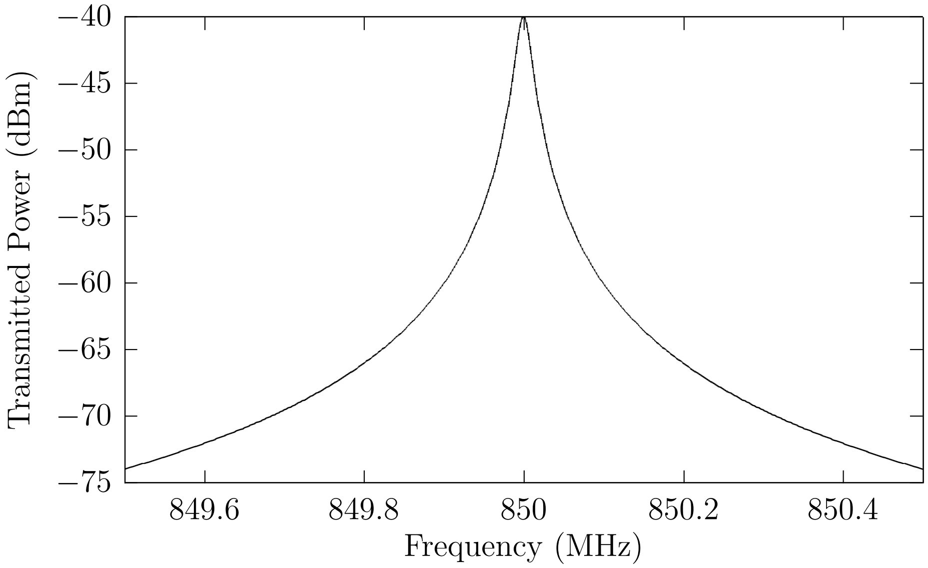

Figure 4.9: A simulated transfer function of a cavity mode. The vertical axis is transmitted power through the cavity. The horizontal axis is the frequency of the injected signal. The Lorentzian line shape, shown here, is the general result of a driven harmonic oscillator, as cavity modes are. This example has a Q of 42,500.

quality factor, Q.

The network analyzer also determines if the major port is critically coupled. As shown in figure 4.8, the network analyzer sends power towards the major port of the cavity through a directional coupler. A directional coupler allows for the small, one-directional injection of power into a transmission line. The power incident on the cavity reflects back when the frequency is either off resonance or if the major port is not critically coupled. The reflected power is measured by a network analyzer. By varying the coupling of the major port while monitoring the reflected power on resonance, the reflected power can be minimized. When the reflected power is minimized, the major port is critically coupled. At acceptable critical coupling, the reflected power is at most −30 dB.

4.3.3 SQUID Amplifier

The first amplifier in the receiver chain is a major source of noise in ADMX: equation 4.4 shows that the scan rate of ADMX improves by roughly the squared inverse of the noise

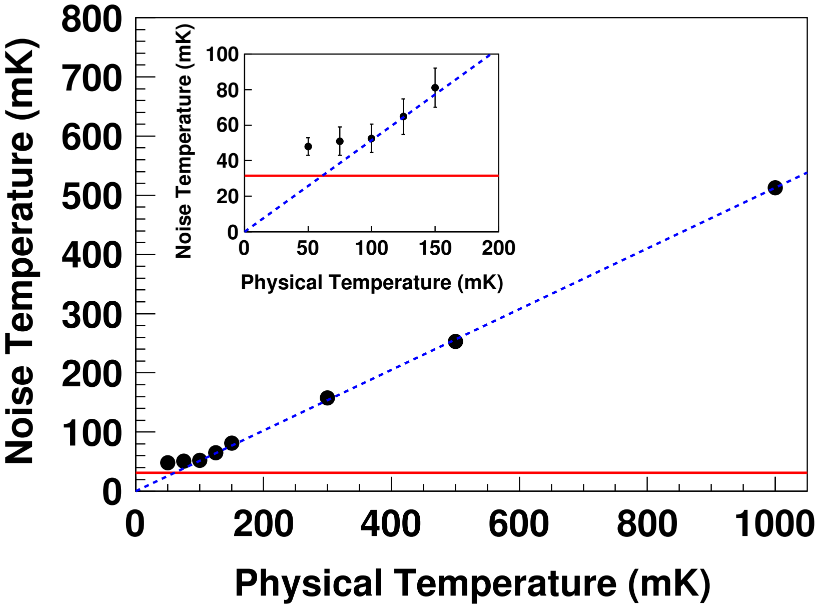

Figure 4.10: The measured SQUID noise temperature as a function of physical temperature for a 600 MHz SQUID amplifier. The dominant classical source of noise in a SQUID amplifier is the Johnson noise from the resistive shunts. As the SQUID is cooled, the noise temperature scales linearly until roughly 100 mK, where the noise flattens to less than twice the quantum limit, defined in equation 4.11 and shown here as the horizontal line. At 2 K physical temperature (not shown), where the ADMX SQUID was operated, the resulting 1 K noise temperature is half the best semiconductor based amplifier. [60]

temperature of the amplifier, hence reducing this amplifier's noise can greatly improves the performance of ADMX. The configuration of ADMX in this thesis improves performance over previous ADMX configurations by replacing the original transistor amplifier on the major port with a SQUID amplifier. The best solid-state amplifiers at ADMX's operating frequency have noise temperatures around 2 K. The source of this noise is electron scattering inside the transistor channel, which cannot be completely eliminated by cooling. In a superconducting quantum amplifier, like ADMX's SQUID, there is no scattering of the supercurrents, leaving mostly thermal noise from normal electrons. It has been found that the noise temperature of the ADMX SQUID amplifier scales as roughly half it's physical temperature. However, there is a lower limit on the noise temperature of a SQUID amplifier, arising from the uncertainty principle of number of quanta, n, and phase, ϕ of an electromagnetic wave [61]:

$$\delta n \cdot \delta\phi \geq 1 \tag{4.10}$$

A quantum-limited coherent amplifier, like ADMX's SQUID, measures both phase and power where the uncertainty of each are minimized to one [62]. Converting the uncertainty in number of quanta to a temperature leads to the coherent-amplifier quantum limit:

$$T_{\text{Quantum}} \geq hk_B\nu = 48\left(\frac{\nu}{1\text{ GHz}}\right) mK \tag{4.11}$$

Figure 4.10 shows that the noise temperature of a SQUID amplifier similar to ADMX's scales as approximately half the SQUID's physical temperature, until near the quantum limit [60].

The microwave SQUID amplifier achieves state-of-the-art noise performance due to a SQUID's fundamentally quantum nature. The following discussion is derived from *Principles of Superconductive Devices and Circuits* by Van Duzer and Turner [63]. In a superconductor, electrons form Cooper pairs, and the ensemble of Cooper pairs are a charged, Bosonic fluid described by a bulk waveform with a long-range, quantum phase, θ. The phase difference around a closed loop of superconductor must equal an integer multiple of 2π. Further, a

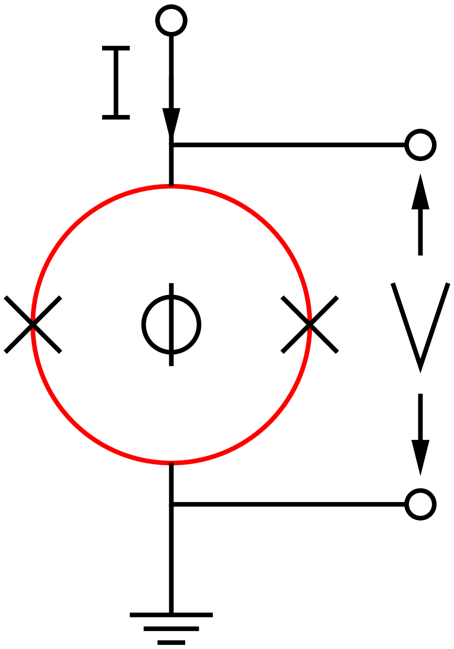

Figure 4.11: A dc SQUID. The “X”s are Josephson junctions and ϕ the flux of magnetic field threading the SQUID. If the bias current, I, through the SQUID is greater then the combined critical current of the Josephson junctions, I$_c$, then the junctions are resistive to the excess current$I -$ I$_c$, which develops a voltage, V, across the SQUID.

magnetic flux, ϕ, threaded through a loop of superconductor introduces a phase difference around the loop of $2e\phi/\hbar$. These two properties lead to flux quantization where $\phi = n\phi_0$ with $\phi_0 = \hbar/4\pi e = 2.1 \times 10^{-15}$ Webers and n any integer.

A small gap between two superconductors, called a Josephson junction, preserves the superconductivity across the gap but adds a phase difference of $\arcsin(I/I_c)$ for a current I passing through the junction and with a maximum current of I_c, above which the junction becomes resistive and develops a voltage.

A dc SQUID is a loop of superconductor weakly broken by two Josephson junctions (figure 4.11). In a dc SQUID, the total superconducting current, I_T, is the sum of the currents through the two junctions: $I_T = I_1 + I_2$. The currents through the junctions are determined by the phase shifts: $I_1 = I_{c1}\sin(\theta_1)$, $I_2 = I_{c2}\sin(\theta_2)$, where θ_1 and θ_2 are the associated phase shifts of the two junctions and I_{c1} and I_{c2} are the critical currents for the two junctions. The total phase shift around the SQUID must be a multiple of

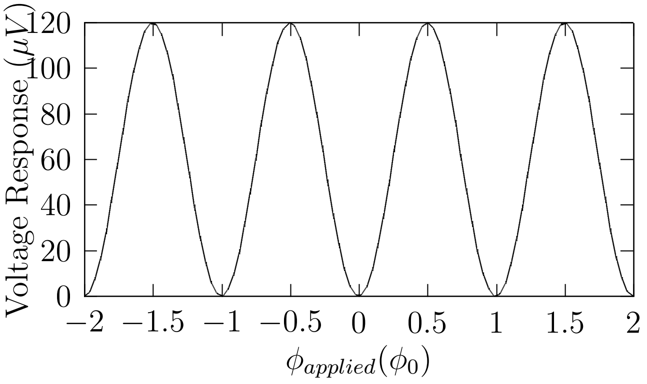

Figure 4.12: Voltage response of a typical SQUID to changing applied flux with a constant current bias. The SQUID is current-biased at its maximum critical current at zero flux. The critical current of the SQUID is maximized when $\phi = n\phi_0$, so these location, in this instance, develop no voltage as the Josephson junctions are superconducting for all current. All other values of applied flux have lower critical current, requiring some of the current to pass through resistive Josephson junctions which develop as a voltage. The flux locations where $\frac{dV}{d\phi}$ is maximized would be the ideal tuning locations for a SQUID amplifier.

2π: $n2\pi = \theta_1 - \theta_2 + 2\pi\phi/\phi_0$. Combining these and maximizing I_T leads to the solution: $I_T\phi = [(I_{c1} - I_{c2})^2 + 4I_{c1}I_{c2}\cos^2(\pi\phi/\phi_0)]^{\frac{1}{2}}$.

If the SQUID is biased with a current, I_B, that is larger than I_T, then the junctions act as resistors for the current $I_B - I_T$ and a voltage develops across the SQUID that varies sinusoidally with ϕ. This voltage is given by $V(\phi) = \max(0, (I_B - I_T(\phi))R)$, as shown in figure 4.12. This behavior makes a dc SQUID a flux to voltage transducer.

In order to use the dc SQUID as an amplifier, first a static flux of $(n + \frac{1}{2})\phi_0$ is applied to the SQUID, maximizing $\frac{dV}{d\phi}$, where a small change in flux produces a large change in voltage. Then the input signal is coupled to the SQUID through a nearby coil. In this way, a small input signal is converted to a small applied flux that threads the SQUID, and the SQUID converts this small applied flux into a large output voltage, providing a net gain. Among other factors, the gain of a SQUID amplifier depends on the mutual inductance between the input coil and the SQUID and the maximum $\frac{dV}{d\phi}$ of the SQUID.

At microwave frequencies, a simple inductive input coil becomes too reactive to make a SQUID amplifier. The impedance of the inductive coil increases at high frequencies, reflecting

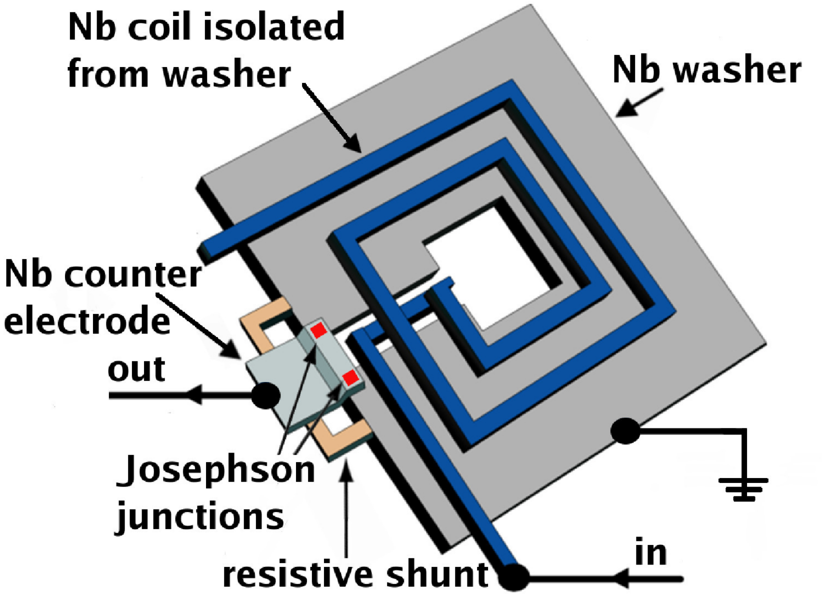

Figure 4.13: A sketch of ADMX's SQUID amplifier. It was a dc SQUID with an input microstrip resonator with a quality factor of around 10. The microstrip resonator converts the input power into applied flux. The small changes in flux from the input signal generate a large change in voltage across the SQUID, producing gain. The resistive shunts on beside the Josephson junctions eliminate hysteresis. This device is roughly a 1 mm across.

the input signal. Furthermore at high frequencies, the low impedance of the capacitance between the input coil and the SQUID effectively shorts the input coil to the SQUID. To overcome these issues, the SQUID is connected to the ground of the input signal and the end of the input coil is floated, converting the input coil into a stripline resonator. The center frequency of this resonator can be adjusted by changing the length of the coil. The Q of the coil, typically 10, can be adjusted by adjusting the impedance mismatch between the coil and the input. In this way, the input coil can be tuned to efficiently convert input power into flux across a narrow frequency range.

The ADMX microwave SQUID amplifier is manufactured with niobium as the superconductor on a silicon wafer. Figure 4.13 shows a sketch of a microwave SQUID device. The superconducting niobium washer, which is the backbone of the SQUID, has a narrow slit that breaks the loop of the washer. The loop is reconnected through two niobium, aluminum oxide, niobium Josephson junctions and a patch of niobium, called the counter electrode.

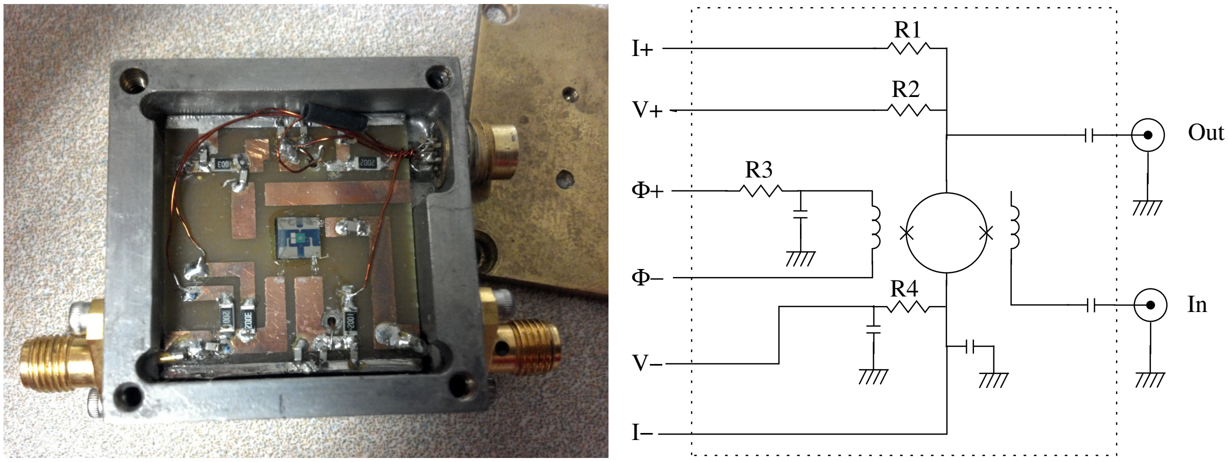

Figure 4.14: Left: the SQUID is mounted inside a lead-lined brass box. Right: the associated circuit diagram of for the SQUID box. Large resistors (R1 at 30 kΩ and R3 at 20 kΩ) reject RF from the current bias (I+ to I-) and flux bias(Φ+ to Φ-) inputs. Resistors R2 and R4 are 2 kΩ each and filter the voltage sense connectors V+ and V-, which allow for *in situ* measurement of the SQUID's I-V curve. The input and output SMA connectors are capacitively coupled, rejecting any dc component of the RF signals. Underneath the PCB (not visible) is a small coil of wire to generate the flux bias. The box is roughly 4 cm on a side. The SQUID itself is the ∼ 1 mm square at the center of the chip mounted the center of the box.

Each Josephson junction has a resistive shunt connected in parallel to protect the junction and improve the SQUID's performance[7]. A niobium coil on top of the dc SQUID allows an input signal to couple into the SQUID. On the silicon wafer supporting the SQUID, large pads for wire-bonding connect to the input coil, washer, and counter-electrode of the SQUID. Two smaller pads act as heat sinks for the resistive shunts.

The ADMX SQUID amplifier is epoxied to a printed circuit board (PCB) inside of a lead-lined brass box, as shown in figure 4.14. The static flux-bias of the SQUID is supplied by a small coil of copper wire underneath the SQUID (not visible). RF signal power enters the box through an SubMiniature version A (SMA) connector with center pin soldered to the PCB. The input power passes through a dc-blocking capacitor, then into the SQUID's input coil. RF output power exits the SQUID, then passes through another dc-blocking capacitor,

---

[7] The junctions in the ADMX SQUID are insulators. Biasing the SQUID above the critical current would necessarily generate large voltages to break down the insulating junction, potentially destroying the junctions. Furthermore, insulating junctions produce hysteretic I-V curves, which limit dynamic range and produce bi-modal behavior.

then exits through an SMA connector. The current bias of the SQUID passes though a large, 30 kΩ resistor. This resistor reflects any RF entering the SQUID box from the current-bias wire. The counter electrode of the SQUID is virtually grounded to the SQUID box via a capacitor. The washer of the SQUID is connected to the current bias and RF output. By grounding the counter electrode instead of the washer, the ADMX SQUID sacrificed gain for performance over a larger range of frequencies by degrading the Q of the stripline resonator[8].

In typical operation, this SQUID achieved around 12 dB of power gain, compared to the $\sim$ 25 dB achievable with the technology [60]. The lower gain design was intentional: sacrificing gain allowed for the SQUID to operate over a larger bandwidth. Hence, ADMX could scan the entire 80 MHz tuning range between the 812 MHz maximum frequency of the previous ADMX cavity and the 892 MHz maximum frequency of the current ADMX cavity without changing SQUIDs. Details on operating the SQUIDs are given in appendix C.1.

4.3.4 Bucking System

The ADMX main magnet produces a large, high-field region at the cavity. The ADMX main magnet does not have an iron field return, so the main magnet produces an extended fringe field: the field at the very top of the insert is over 300 Gauss. Furthermore, the ADMX SQUID needs to be close the the cavity to minimize cable attenuation losses and simplify cryogenic design, requiring that the SQUID reside in a high field environment. However, a SQUID is an exceptionally sensitive magnetometer, so a SQUID's environment must have only very small and very stable magnetic fields. Figure 4.15 shows the "bucking magnet system" used to eliminate the field within a small volume around the SQUID within ADMX.

The majority of the main magnet's field in the SQUID volume is actively eliminated with a superconducting solenoid. The solenoid produces a near-zero field volume roughly 20 cm tall by 20 cm across and roughly 1.6 m above the center of the main magnet. Since this solenoid

---

[8] This was observed empirically.

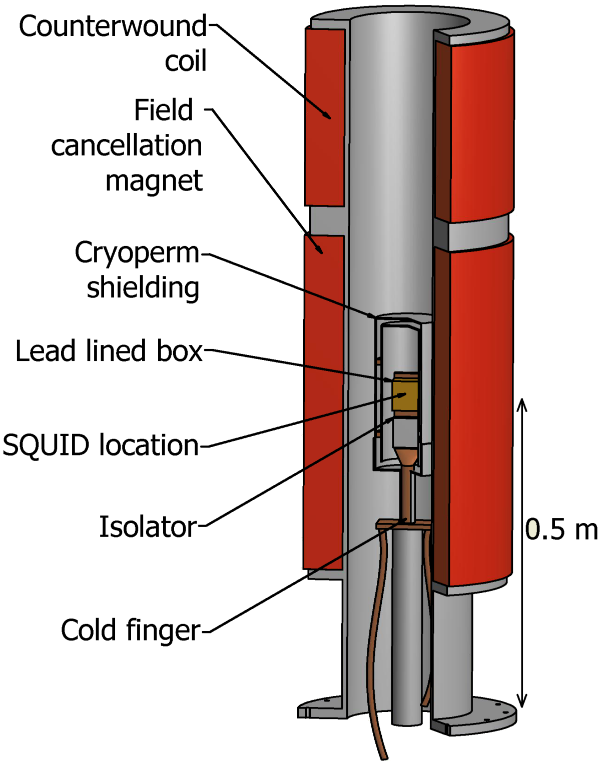

Figure 4.15: A cross section of the bucking magnet system. The lower coil produces the zero field volume necessary for the SQUID to operate. The upper coil cancels the forces between the bucking magnet system and the main magnet. The magnets reduces the field to a few Gauss in the region around the Cryoperm shield. The shielding reduces the field inside by roughly 10,000×. The SQUID itself is in a lead-lined box which becomes a superconducting shield when cooled below 9K. Thick copper cables connect the cold finger to the 1 K pot, which keeps the SQUID at 2 K while the bucking system around it is 4.2 K.

has a magnetic dipole moment in opposition to the dipole moment of the main magnet, there is a substantial repulsive force between this solenoid and the main magnet. There is also substantial mutual inductance between this solenoid and the main magnet, which may allow for a quench in one magnet to propagate to the other. To eliminate the net force and net mutual inductance between the solenoid and the main magnet, a second superconducting solenoid is mechanically connected and in series with the first, but is reversed in polarity. The mutual inductance and the force between this second solenoid and the main magnet are near equal and opposite of the first solenoid. This pair of coils together form the bucking magnet, which produces the near zero field volume near the SQUID shown in figure 4.16. The bucking magnet (figure 4.17) is a 4.6 Henry niobium titanium superconducting magnet made by American Magnetics Incorporated. The magnet is trained to a maximum current of 148 Amps. At this current, the bucking magnet can eliminate the fringe field in the SQUID volume when the main magnet is at 8.5 Tesla. The bucking magnet is thermally tied to LHe inside the reservoir by copper radiation shields which are maintained at the 4.2 K LHe temperature. Due to its small inductance of 4.6 Henry and modest current, the maximum stored energy of the magnet is only 46 KJ, allowing the bucking magnet to safely quench without cryogens.

To further reduce the magnetic fields in the SQUID volume, two concentric Amuneal Cryoperm[9] cryogenic μ-metal shields attenuate the field inside by roughly 10^4 (figure 4.18). A third, inner shield was fabricated (as shown in figure 4.18), but is not used due to space limitations. The SQUID is packaged in a lead-coated brass box that immobilizes any magnetic flux as the box is cooled below lead's superconducting transition temperature of 9 K. The box also acts as a Faraday cage against stray microwaves (figure 4.14). This system of shields is designed to attenuate small, < 100 Gauss, magnetic fields but saturate at higher fields: any excess fields penetrate. Careful control of the bucking magnet is necessary to

---

[9] Amuneal fabricated, annealed, and demagnetized the shields. Each layer was specified to provide 100× field attenuation. More details on Cryoperm at http://amuneal.com/magnetic-shielding/theory-design/magnetic-shielding-materials

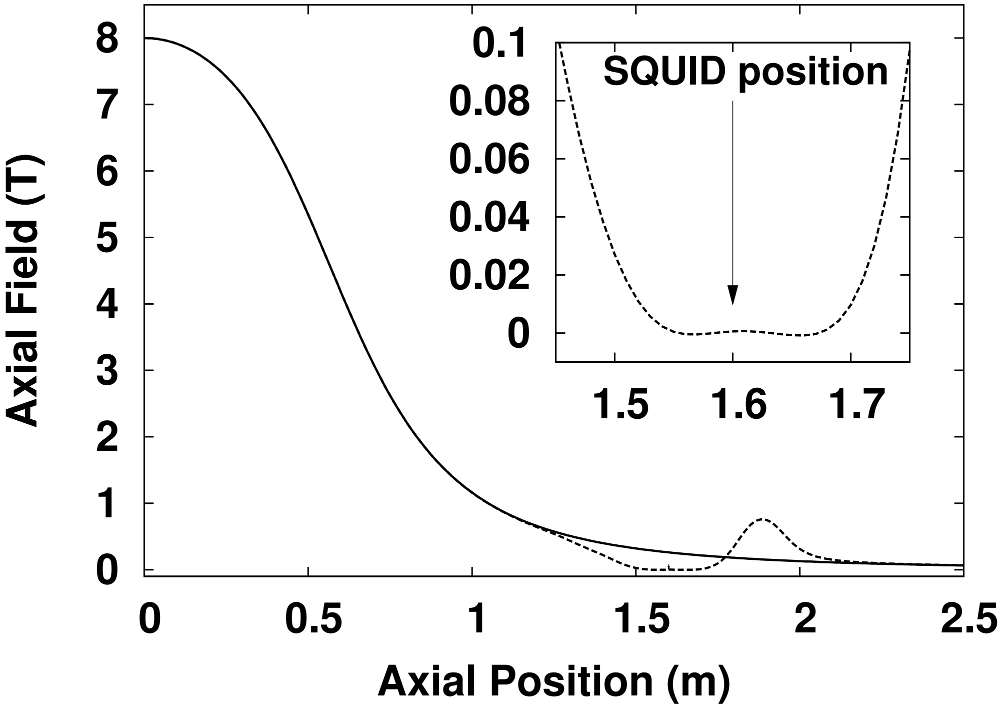

Figure 4.16: The axial magnetic field strength versus distance from the center of the main magnet. The dashed line shows the field with the bucking system operating. Without the bucking system, there would be a field of roughly 2 KG at the SQUID location, too large to eliminate with passive shielding. With the bucking coil, the field is reduced to 10's of Gauss at the SQUID position. This plot was generated from the coil plan of the magnets, not from measured data. The axial field was measured in 3 positions: at around .8 m, at 1.6 m within the shield, and at 1.7m outside of the shield. These measurements were in agreement with this field map. The near-zero field measurement within the Cryoperm shield confirmed that the bucking coil combined with the Cryoperm shielding were sufficient for the SQUID to operate.

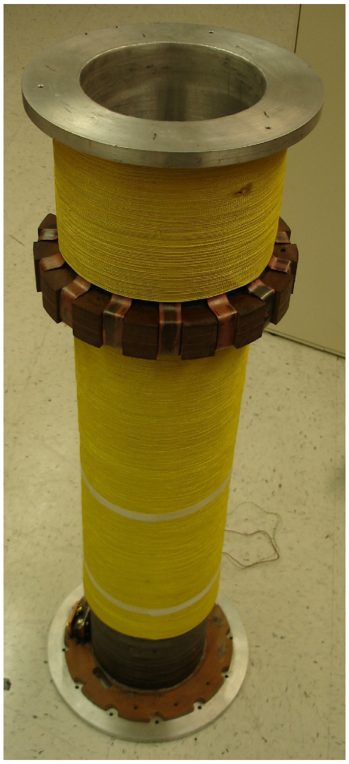

Figure 4.17: The bucking coil is a compound coil with a long, main solenoid to produce a zero-field volume and a counter-wound coil to eliminate any mutual inductance between the bucking coil and the main magnet. The epoxy potted, copper stabilized, niobium-titanium coils have a total inductance of around 4 Henries. It is welded inside the insert's LHe reservoir.

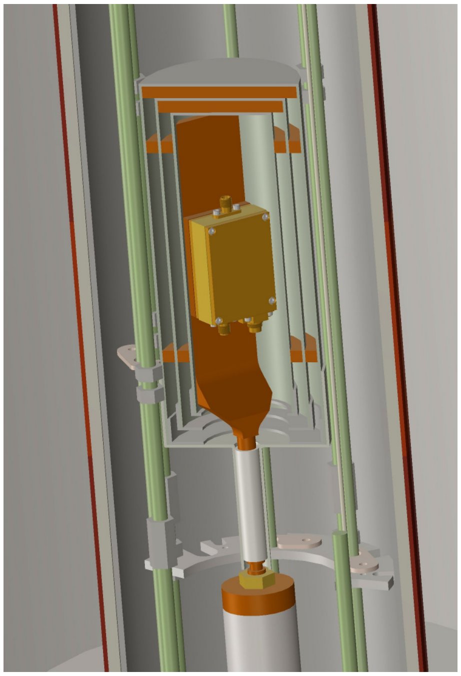

Figure 4.18: A closeup of the SQUID mounted on the cold finger. The area around the SQUID is a tight fit with the Cryoperm shielding, drive shafts, baffles, wiring, and pump-out lines packed within the bore of the bucking magnet. The shown inner third layer of Cryoperm shielding is not used, due to its interference with the isolator (not shown).

allow only small net fields in the the neighborhood of the shields. This magnet control is implemented in software, as described in section 4.4.2. Altogether, the bucking system allows the SQUID amplifier to operate successfully within the ADMX insert.

4.3.5 HEMT Amplifiers

As mentioned earlier, the SQUID amplifier produces 12 dB of gain, thereby increasing the cavity and SQUID's combined 3 K Johnson noise power to 30 K at the SQUID's output. The first room-temperature amplifier has a noise temperatures of roughly 100 K, which would dominate the SQUID's output noise: additional cryogenic amplification is therefore required. A pair of cryogenic amplifiers are installed in the signal chain between the SQUID and room temperature electronics. These high performance solid state amplifiers are repurposed from previous ADMX operations.

Previous operations of ADMX used National Radio Astronomy Observatory (NRAO)

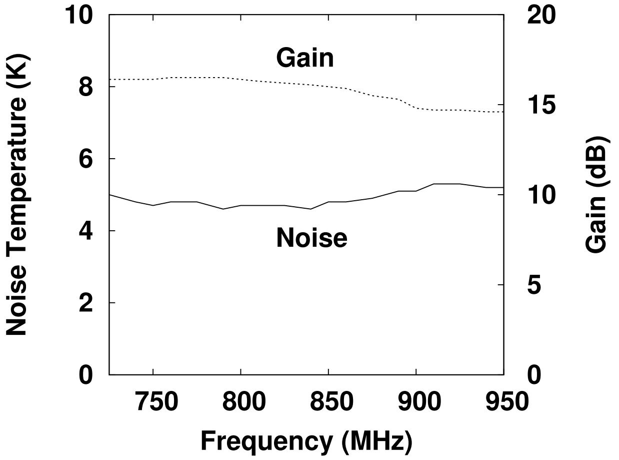

Figure 4.19: The gain (dotted line) and noise (solid line) of one of ADMX's HEMT amplifiers versus frequency. HEMT's have good bandwidth, decent noise temperature, close to ideal 50 Ω impedance, and stable operations making them ideal post amps for SQUIDs. The best HEMTs have noise temperatures of around 2 K.

High Electron Mobility Transistor (HEMT) amplifiers as their first stage amplifiers[10], which are re-purposed to amplify the SQUID's output. The HEMT amplifier installed directly after the SQUID has noise and gain performance shown in figure 4.19, which provides roughly 15 dB of gain while only adding 10% noise to the cavity signal. The second HEMT amplifier installed after the first, provides another roughly 15 dB of gain, but contributes less than 1% noise to the cavity signal.

However, the individual transistor amplifiers inside the HEMT amplifier packages are far from the ideal 50 Ω impedance that would yield zero reflections off the amplifiers' inputs and outputs. To reduce these reflections, the HEMT amplifiers are of a "balanced" design, as shown in figure 4.20. This scheme uses a matching pair of transistors and two 90° hybrids[11] to create destructive interference of reflections off the transistors at the input and output, instead dissipating the reflected power into 50 Ω terminators. The resulting balanced amplifier appears as nearly an ideal 50 Ω load at both the input and output of the device.

---

[10] HEMTs are also known as Hyterstructure Field Effect Transistors (HFETs). ADMX employed a wide variety of HEMT amplifiers from 400 MHz to 2 GHz, all balanced, gallium arsenide designs from NRAO. Further information on these amplifiers can be found at http://www.nrao.edu/engineering/amplifiers.shtml

[11] A 90° hybrid is a four port device organized into two pairs of inputs and outputs. Each input signal is split evenly between the two outputs with a 90° phase difference between the two.

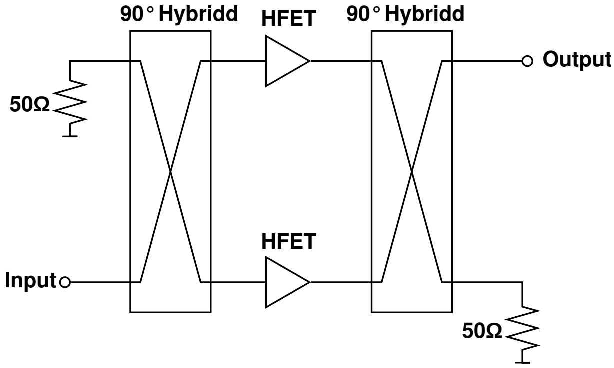

Figure 4.20: Schematic of a Balanced Amplifier. Even though the matched pair of HEMTs (HFETs) do not provide ideal, 50 Ω impedance across their frequency range, the balanced amplifier does. This is due to the two 90 degree hybrids perfectly canceling any reflections off the near-identical HEMT amplifiers. Instead, the power reflected off the matched pair of amplifiers is deposited into the 50 Ω terminator

The noise of HEMT amplifiers originates from electron scattering within the semiconducting channels. As the channels are cooled, overall there is less and less scattering, allowing for the amplifier to become quieter at cryogenic temperatures. However, the minimum amount of scattering combined with local heating of the channels produces a lower limit to the noise temperature of HEMT amplifiers of roughly 2 K. Furthermore, at cryogenic temperatures, defects are not shielded by charge carriers, generating large fields that scatter electrons and generate extra noise. To eliminate this effect, LEDs are flashed occasionally to excite and free charge carriers, which then neutralize the defects.

4.3.6 Receiver Chain

Figure 4.21 shows a schematic of the path the signal power takes from the cavity to the computer for analysis. The signal is extracted from the cavity through an electric field probe[12]. The field probe is connected to the directional coupler. Semi-rigid, SMA-terminated, copper-jacketed RG402 coax cables connect the cryogenic RF components to one another, which has a cable attenuation of 4 dB/10 m at 1 GHz. The directional coupler is connected to the SQUID amplifier. The SQUID amplifier is connected to the HEMT post-amplifiers. From

---

[12] The field probe is constructed of semi rigid copper RG402 coax cable that has a section of its outer shield removed.

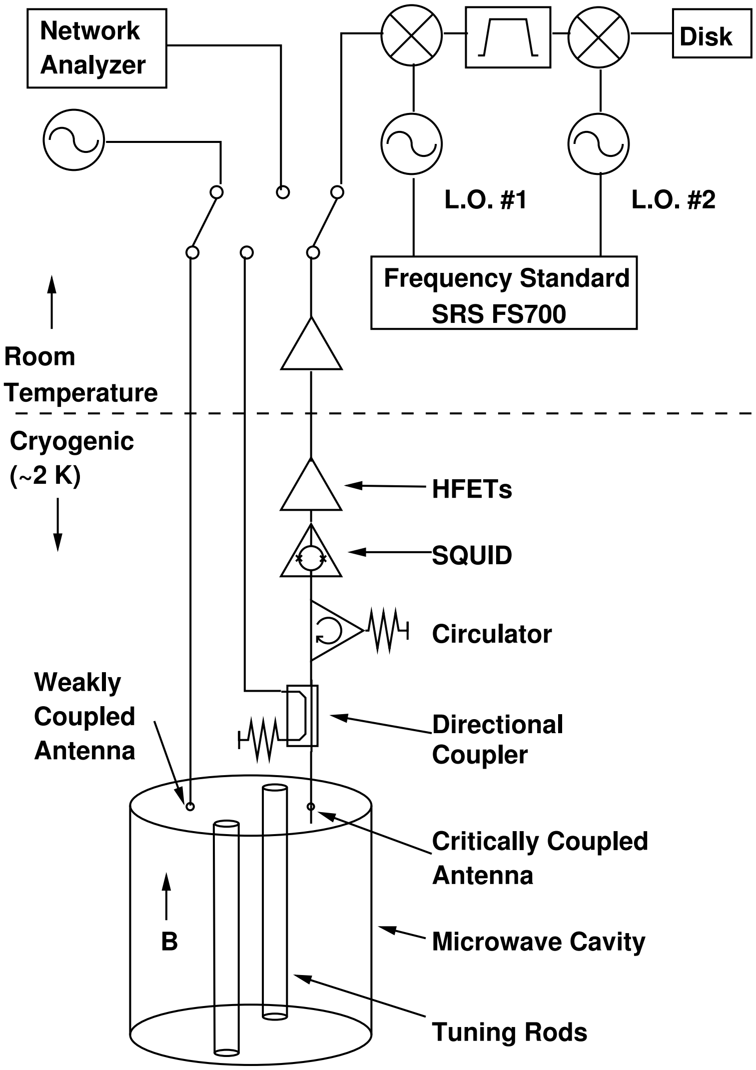

Figure 4.21: The architecture of the ADMX signal chain and receiver. The network analyzer and its associated frequency sweeper send RF power either through the weakly-coupled minor port to measure the TM_{010} mode's frequency and Q or through the directional coupler towards the major port in order to critically couple it. During data-taking, power from the cavity travels up the RF chain, through the SQUID amplifier and post-amps and into the receiver. The first major component of the receiver is an image reject mixer than shifts the axion-sensitive TM_{010} mode's frequency down to 10.7 MHz. The second major component is a crystal filter that eliminates all power outside of its 10.7 MHz centered 30 kHz wide bandpass. The third major component of the receiver is a mixer that shifts the 10.7 MHz signal down to 20 kHz. This signal is digitized and saved to disk, slowly forming the large dataset over the multi-year run.

the cryogenic HEMT post-amplifiers, the signal enters a rigid RG402 transmission line that runs to the top of the ADMX insert. This cable is has a stainless steel jacket and center pin which have been flashed with copper for low RF loss without high thermal conductivity. Outside the ADMX insert, the signal is amplified by 60 dB with two commercial post-amplifiers which drive a 30 m triple-shielded cable going into the ADMX receiver.

The first component in the receiver is an Agilent 34970 switch unit that multiplexes the signal to either the network analyzer or to the receiver's first mixing stage. The mixing stage shifts the roughly 850 MHz signal down to 10.7 MHz with an image-reject mixer[13]. The signal is then amplified 15 dB and filtered through a temperature-stabilized, eight-pole, crystal filter centered at 10.7 MHz with 30 kHz bandwidth. The approximate shape of the crystal filter's bandpass is shown in figure 4.22. After the crystal filter, the signal is amplified by 15 dB and mixed down to 20 kHz. An audio frequency distribution amplifier splits the signal into 4 outputs and rejects the 21.4 MHz image signal generated by the second-stage mixer. Two of these outputs connect to analog to digital converters (ADCs) for voltage sampling.

4.3.7 Analog to Digital Converters (ADC)

One of the two ADCs is within an SRS SR760 FFT spectrum analyzer[14]. The SR760 captures the 30 kHz bandpass of the receiver by sampling at 100 kHz and performing a Fast Fourier Transform (FFT) on the input voltage time series. The SR760 has a time series consisting of 800 samples. Since an 800 sample, 100 kHz time series only takes 8 ms to capture, the SR760 takes 10,000 800-point timeseries in 80 seconds, performs a Fast Fourier Transform (FFT) on each one, and averages them into a single, 400 point, 50 kHz wide, single-ended power spectrum. The 2010 ADMX axion limit publication [64] has results generated from

---

[13] A mixer produces two output signals for each input signal. An image reject mixer uses an architecture like the balanced amplifier described previously to separate the two image signals by using two mixers and two 90° hybrids. The MITEQ IRM045-070-10.7 image reject mixer in ADMX requires a +15 dBm local oscillator signal and attenuates the signal by 6 dB.

[14] More information available at: http://www.thinksrs.com/products/SR760770.htm

power spectra from the SR760.

The 400 point, 50 kHz power spectra produced by the SR760 have a Nyquist resolution of 125 Hz, the inverse of the integration time of 8 ms. This relatively wide resolution is unsuited for searching for possible narrower structures in the Milky Way halo. To search for these narrower structures, another ADC captured higher-resolution spectra. A National Instruments PCI-4551[15] digitizes the output of the receiver at 80kS/s for 1,906,840 samples, yielding a Nyquist resolution of 0.042 Hz. Three such 23.8 second integrations were taken for each SR760 integration. The time standard used to generate all ADMX signals, an SRS FS700, had a rated stability of 1 part in 10^{10} over the short timescales during integration, so the 812 MHz to 892 MHz dataset is assumed to have a frequency-standard limited resolution of roughly 0.085 Hz. The actual resolution was not measured due to the lack of a more stable signal source than the SRS FS700 itself as the reference. The data recorded by this ADC form the basis of the analysis given in chapter 5.

The time series recorded by each ADC are Fourier-transformed into power spectra. A typical power spectrum is shown in figure 4.22. Each component in the receiver contributes its transfer function to the spectral shape, but the vast majority of the observed structure is from the crystal filter's bandpass response. As seen in figure 4.22, the bandpass of the receiver has significant ripple structures and sharply falling skirts outside the bandpass. The crystal filter's structure is substantially removed during analysis.

4.3.8 Scanning over Frequency

The normal cadence of the experiment is: rotate a tuning rod by roughly 10 steps by the stepper motor drive, measure the new location of the TM_{010} mode, then record with the ADCs for roughly 80 seconds. The number of required steps is established by measuring the frequency shift from tuning to subsequent tuning and adjusting the number of steps until

---

[15] The National Instruments PCI-4451 has 2 inputs and 2 outputs, 204.8 KS/s maximum sampling rate and 15.5 bit sampling resolution via a delta-sigma modulated 8 bit ADC. The inputs have 10 dB increment adjustable gain with a range of -20 dB to +60 dB.

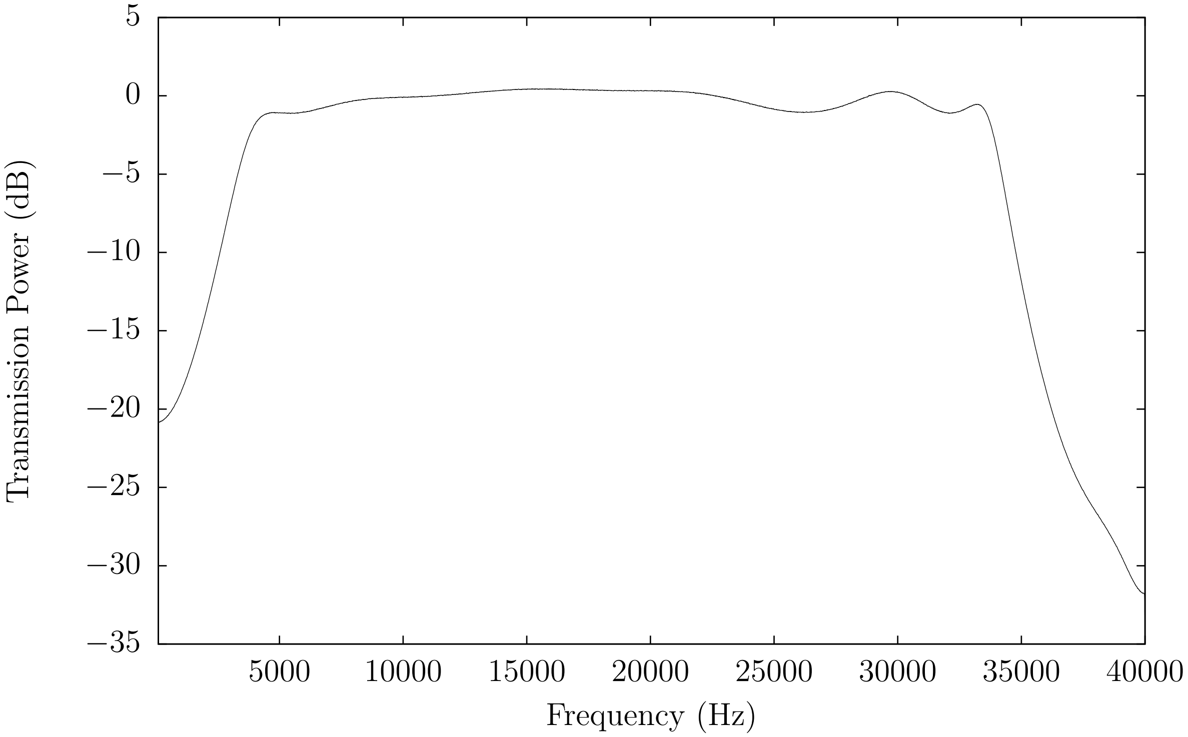

Figure 4.22: A measurement of the transfer function of the receiver. The vertical axis is power in dB, with the highest point scaled to 0 dB. The horizontal axis is frequency. This power spectrum is the average of one day's worth of spectral data. The structure seen in this spectrum is from the crystal filter's bandpass. The crystal filter's bandpass is centered at 10.7 MHz (20,000 Hz in the plot): the signal represented in this spectrum is mixed down by 10.68 MHz after the crystal filter.

there is, on average, a 2 kHz frequency shift between tunings. With a receiver bandwidth of 30 kHz, an average frequency shift of 2 kHz per tuning, and an integration time of 80 s, every frequency has a total exposure of roughly 1200 seconds. The experiment continues recording data in this manner until roughly 5 MHz of continuous data has been taken, called a "nibble". If the SNR is too low for any regions of frequencies within the 5 MHz nibble, these frequency regions are rescanned under normal cadence, stepping 2 kHz between integrations. After the entire nibble has reasonable SNR, with all frequencies roughly sensitive to a KSVZ model axion signal, any single frequencies with statistically large powers, called "candidates", are revisited, and candidate frequencies are integrated without stepping for 30 minutes. Ultimately, all candidates were identified as statistical fluctuations, which disappeared after revisiting, or external signals, which were eliminated by with additional shielding and revisiting. The presence of external signals is investigated further in section 5.3.2.

The ADMX receiver has to track the cavity's TM_{010} mode as the tuning rods move. The cavity mode structure is not trivial: the TM_{010} mode has to be identified out of dozens of other cavity modes. The TM_{010} mode is best identified by creating a mode map; where a tuning rod is rotated completely around inside the cavity while the network analyzer measures the cavity's transfer function from 400 MHz to 900 MHz. This contains the entire tunable range of the TM_{010} mode for this geometry. Due to the 42,000:1 gear reduction of a tuning rod gearbox and the slow 480 rpm stepper motor, completely revolving a rod inside the cavity takes 8 hours and 8.4 million steps. Only one mode map is taken before each new data run. The TM_{010} mode is easily identified in the mode map as the lowest frequency mode among the set of tunable modes.

4.3.9 Cryogenics

The ADMX cavity and SQUID are maintained at roughly 2 K using pumped liquid helium (LHe). Since LHe has a very small latent heat and is expensive (now, well over $4 per liquid liter) the insert is designed to minimize boil-off. As shown in figure 4.3, the insert is installed inside the main magnet's warm bore. The main magnet has two thermal intercepts to the warm bore, one at 78 K, roughly .5 m from the top, and the other at 50 K, roughly 1 m from the top. The space between the insert and the warm bore is maintained at a high vacuum of roughly 10^{-10} Torr by an external turbo molecular pump and by the cold insert's cryopumping. The insulation vacuum space near the top of the insert has 6 large superinsulated radiation baffles to isolate the 4.2 K helium reservoir from the 300 K top of the experimental insert. The inside of the central support of the insert also has baffles to intercept radiation, These also capture enthalpy from escaping He gas during cool-down and capture enthalpy from the "1 K pot's" exhaust, described later. During normal operation, the cavity space was also under high vacuum. The bucking magnet's vapor-cooled leads captured enthalpy from the LHe reservoir's exhaust gas. The experimental insert's 180 l reservoir was refilled approximately every 5 days.

The cavity is maintained at 2 K by a LHe refrigerator called a "1 K pot". A 1 K pot uses strong suction on LHe to evaporatively cool the LHe from 4.2 K at 700 Torr to roughly 1 K at 1 Torr along helium's liquid-gas phase transition. A 1 K pot is continuously operated by feeding 4.2 K LHe into the pot through a capillary tube from the LHe reservoir. Since LHe has a phase transition to a superfluid at 2.2 K, the pumping port of the pot has a small constriction to prevent superfluid helium from traveling up the pumping port. ADMX's 1 K pot is bolted directly to the top of the cavity. In order to cool the SQUID to near the 1 K pot's temperature, thick copper cables create a strong thermal link between the 1 K pot and the SQUID. The 1 K pot is fed from the LHe reservoir through an adjustable needle valve, which regulates the flow of LHe into the pot. The needle valve is adjusted by a stepper motor on top of the insert which drives a 140:1 gearbox attached to the valve shaft. The vigorous suction on the 1 K pot is provided by a large Edwards EH500 roots blower boosting an Edwards E2M80 rotary vane mechanical pump. Due to the extended fringe field of the magnet, the pumps are located around 10 m from the magnet. While these pumps have a

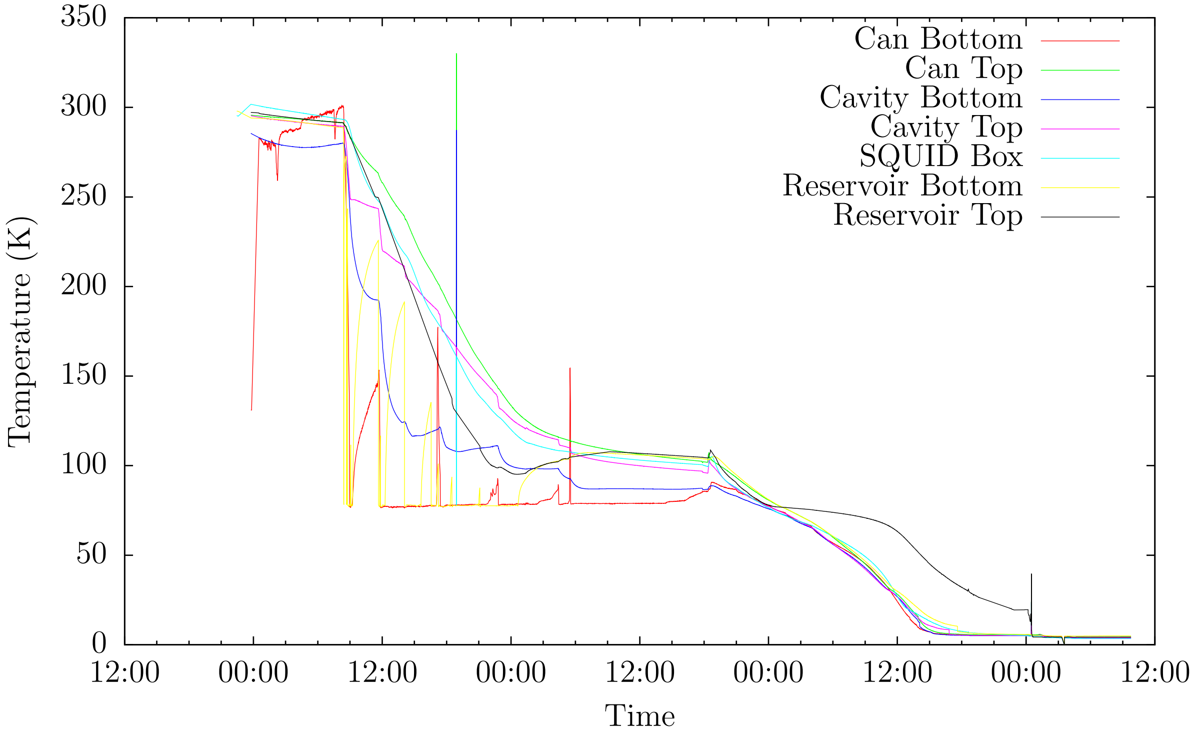

Figure 4.23: The temperatures of cryogenic insert components during a cool-down. The drop from $\sim$ 300 K to below 100 K was from the 78 K LN2 being transferred into the insert. The insert was then evacuated and LHe was used to cool down to 4.2 K. The entire operation took two to three days on average.

very large pumping capacity, roughly 600 m^3/hour at 1 Torr, the necessarily long pumpout tubes for the 1 K pot require much of this capacity. Since the pressure at the 1 K pot is higher than 1 Torr, the 1 K pot maintains a base temperature of near 1.8 K, compared to the cavity temperature of 1.2 K during the 1995 to 2005 run.

Figure 4.23 shows the temperature of the cryogenic components of the insert throughout a typical cool-down procedure. Occasional cool-downs of the experimental insert from 300 K are performed first by flowing liquid nitrogen, LN_2, down two dedicated tubes: one to the side of the cavity and one to the top of the LHe reservoir. LN_2 quickly accumulates at the bottom of the cavity and reservoir spaces, but the top of each space takes considerable time to cool (around a day). Once the top of the cavity and the top of the reservoir are < 90 K, any nitrogen, whether gas or liquid, is removed before cooling with LHe, else the nitrogen would freeze. Excess LN_2 in the reservoir space is blown out through the LHe "pre-cool" tube by overpressuring the LHe reservoir, but any LN_2 in the cavity space is slowly boiled off with heaters. When heaters at the bottom of both spaces increase the temperatures above 78 K, the heaters are turned off and both spaces are pumped down to a few mTorr. Both spaces are then filled with Helium gas, then LHe is slowly flowed to the bottom of the cavity space until the entire cavity's temperature is below 10 K. In a standard cool-down, first the cavity space is evacuated, then the reservoir is filled with LHe, and finally the 1 K pot cools the cavity and SQUID down to 2 K. The 1 K pot is started by filling it with 4.2 K LHe, then pumping the 1 K pot down in pressure and temperature while adjusting flow to prevent the pot from overflowing or running dry; this requires continuous adjustment during normal operations.

The superconducting main magnet is maintained at 4.2 K within the LHe reservoir, with a capacity of 750 liters. The main magnet requires at least 250 liters of LHe to cover the coils and provide quench protection. In a quench, a section of superconductor becomes resistive inside the coils and runaway ohmic heating eventually converts all the 16.54 MJ of stored energy into heat. This heat would destroy the magnet if it were not cooled by LHe. The 4.2 K LHe reservoir is surrounded by three radiation shields under high vacuum to thermally isolate the LHe reservoir from room temperature. A LN_2 reservoir maintains the outer shield at 78 K. The main magnet has a high LHe boil-off of 500 l every 8 days, primarily due to the highly conductive vapor-cooled leads.

Due to a funding freeze in July of 2008, the main magnet was warmed up to room temperature, requiring a subsequent cool-down in late 2008. The cool-down procedure of the main magnet is similar to that of the insert. First, LN_2 is used to cool the coils to 78 K. Unlike the insert, which has delicate gears, mirrored surfaces, and small tubes, the magnet is robust to small amounts of nitrogen ice. So, instead of evacuating the magnet before transferring LHe, He gas is blown into the bottom of the magnet to help expel some of the nitrogen gas. LHe is then transferred to the base of the magnet, slowly cooling the magnet down to 4.2 K. The six ton coils require roughly 1000 liters of LHe to cool from 78 K to 4.2 K.

4.3.10 Sensors

ADMX has around 50 sensors to monitor and diagnose the experiment. Inside the insert, temperature sensors, LHe level gauges, LN_2 level gauges, and Hall probes monitor the health of the experiment. Outside the insert, pressure gauges monitor the various spaces of the experiment. Figure 4.24 shows the approximate locations of all sensors and heaters inside the ADMX insert and inside the ADMX magnet.

Lakeshore Cernox sensors[16] measure the temperature of the ADMX insert. Calibrated sensors are mounted on the top and bottom of the cavity as well as on the SQUID amplifier. The measurements from these sensors are the basis of the noise temperature in the analysis: from ex-situ measurements, the system noise temperature is known to be at most half the SQUID temperature added to the average cavity temperature. Cernox temperature sensors are mounted on the HEMTs, vacuum can top and bottom, bucking coil, and 1K pot. Platinum sensors[17] were installed on the baffles as well. Temperature sensors are critical for diagnosing, monitoring, and calibrating the cryogenic systems.

Superconducting LHe level gauges are mounted within the vacuum can around the cavity, on the cavity top, and inside the LHe reservoir. The level gauges on and around the cavity are useful when occasionally operating with the cavity filled with LHe. The level gauge in the reservoir monitored the amount of LHe in the experimental insert. Five level gauges monitored the main magnet's LHe reservoir.

---

[16] Cernox is a proprietary thin-film resistive thermometer from Lake Shore Cryotronics Inc. Their low sensitivity to magnetic fields and monotonically decreasing resistive curve from 300 K to 100 mK make them ideal for use in ADMX. More information can be found at: http://www.lakeshore.com/products/Cryogenic-Temperature-Sensors/Cernox/Models/Pages/Overview.aspx

[17] Platinum resistive thermometers have acceptable tolerance of magnetic fields and uniform temperature-resistance curves. However, they have poor sensitivity below 30 K, limiting their usage to higher temperature locations inside ADMX. More information can be found at: http://www.lakeshore.com/products/cryogenic-temperature-sensors/platinum-rtds/models/pages/overview.aspx

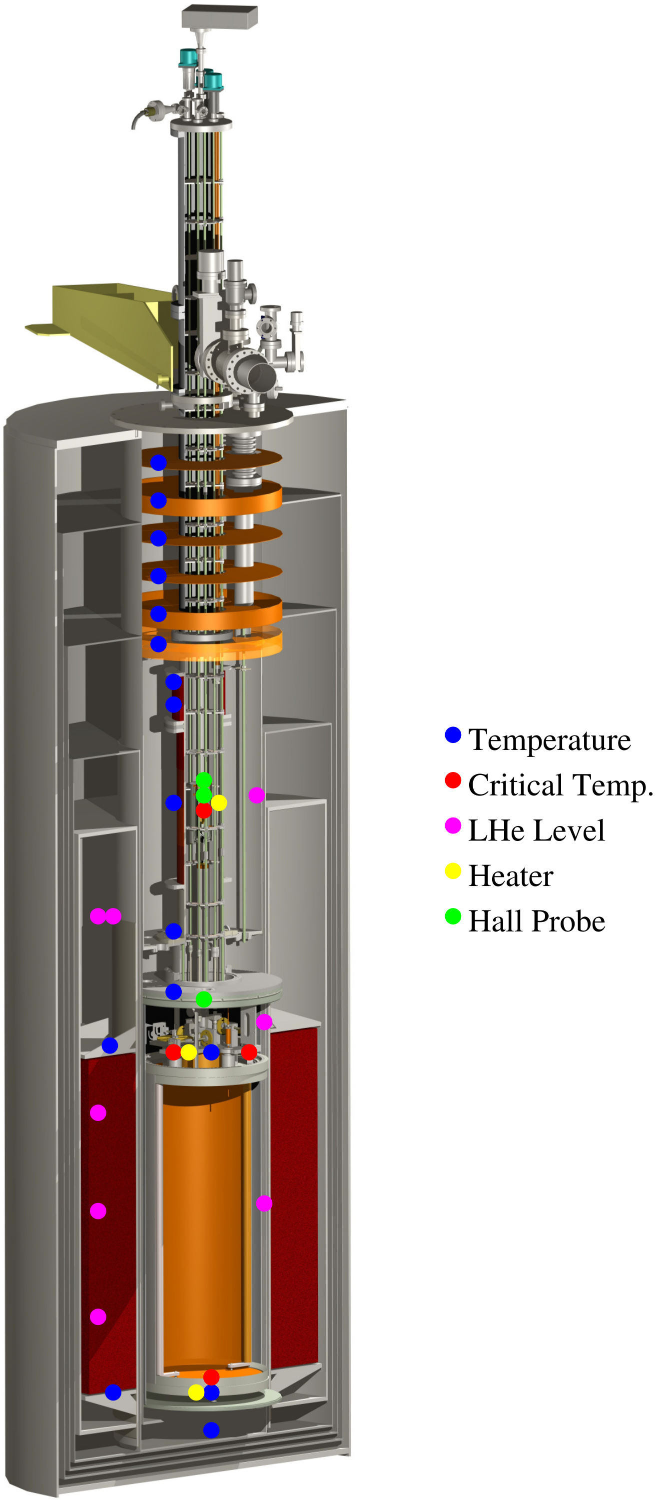

Figure 4.24: The locations of various sensors in ADMX. Science critical temperature sensors were used in the analysis to calculate the expected noise power for the cavity and amplifier system. The other temperature sensors were used to diagnose cryogenic problems. Hall effect sensors were necessary for ramping the bucking coil. Level gauges were required for monitoring the remaining LHe. Each vacuum space also had appropriate pressure gauges (not labeled).

Four cryogenic Lake Shore Hall-effect sensors[18] measure the magnetic field near the SQUID. The first is on top of the 1K pot and measures the axial component of the main magnet's field. The second measures the axial field on the top of the Cryoperm shield and detects cancellation errors in the bucking system. The third and fourth measure the axial and transverse fields on the SQUID box and detect unwanted magnetic field intrusion when the Cryoperm shield is saturated by a strong field. The Hall sensors are driven in series by a 100 mA current source for less than a second every 10 minutes. The high resistance of the Hall sensors and cabling requires roughly 20 V to drive the 100 mA current, producing 2 Watts of heating while active. The low duty cycle reduces heating, especially in the sensitive SQUID area.

Lakeshore 25 watt heaters are mounted at the bottom of the both the the insert's LHe reservoir and the vacuum can to boil off excess cryogens, especially LN_2. Another heater is mounted on top of the cavity, which was intended for an *in situ* noise temperature test via heating the cavity. However, the temperature-dependent properties of the SQUID, which is thermally tied to the cavity, made this difficult.

Pressure gauges at the top of the insert monitor the insert's four vacuum spaces. All spaces have mechanical pressure gauges, marked from -30 in Hg to 30 psig, and appropriate overpressure relief devices. The cavity space also has a 100 Torr MKS Baratron capacitive manometer[19]. The insulation space has a 10 Torr Baratron and an ion gauge. The 1 K pot space has two Convectron type Pirani gauges mounted at various positions along the pumpout line.

---

[18] The ADMX Hall sensors have extensive calibration curves at 4.2 K. However, thermoelectric voltages produce an uncalibrated offset, interpreted as roughly 10 Gauss. More information can be found at: http://www.lakeshore.com/products/hall-magnetic-sensors/pages/overview.aspx

[19] Manometers provide gas independent pressure readings, with only a slight temperature dependence and no discernible magnetic field dependence. The Baratrons on ADMX had analog outputs that produced 10 V at their full scale pressure and were typically accurate down to .1 V. More information on MKS Baratrons can be found at: http://www.mksinst.com/product/category.aspx?CategoryID=72

4.3.11 Maintenance

Many regular maintenance operations are performed during operations. The most common and routine maintenance operations are cryogen transfers. LHe is delivered in 500 l dewars roughly once a week. Double-jacketed transfer lines are installed between these dewars and the magnet or insert. An integrated heater inside the dewar pressurizes it to 4 or 8 psig, driving LHe through the transfer line to fill the main magnet's LHe reservoir or the insert's LHe reservoir. LN_2 is delivered in 150 l dewars and is transferred through a Teflon tube to the main magnet's LN_2 reservoir.

Major issues with the experiment would require a "pull-out" operation, where the insert is removed from the main magnet. In order to remove the insert, first, the magnets are ramped down to zero field. Then any LHe is removed from the insert with either heaters for small amounts or by spoiling the insulation space for large amounts. Then, the insulation space is filled with helium or nitrogen gas. Finally the insert is pulled out with a gantry crane and a counter-balanced lifting fixture. The insert is still very cold and condenses moisture. To prevent water from entering sensitive parts of the insert, the insert warms up overnight before opening. To open the insert and get to the critical cavity and amplifier components, the vacuum can around the cavity is removed. To remove the vacuum can, first a clamping ring is attached to the can, then the insert is lowered into a duplicate warm bore, resting the ring on the lip of the bore. The roughly 160 bolt circle is unfastened, breaking the indium seal at the top of the vacuum can. The insert is then lifted from the bore, leaving the vacuum can behind and exposing the cavity. The insert is mounted on its dedicated stand for maintenance. To access the SQUID area, the cavity also has to be carefully removed from the insert. These delicate procedures translate into weeks of down time for any major issue with the insert.

Installing the insert back into the warm bore incorporates a checklist to prevent a wasted cool-down. First, all sensors must be reading correctly. If the cavity was been removed, then the 1 K pot is leak checked before the vacuum can is reinstalled. Reinstalling the vacuum can requires that its associated indium seal and bolt circle are carefully remade and leak tested. The cavity space, reservoir space, and 1 K pot space are filled with a dry gas, either helium or nitrogen. Then the insert is lowered into the magnet bore. The insulation vacuum, spoiled by air, is pumped down for several days to remove any ice buildup and verify the vacuum integrity of the top plate of the insert.

4.4 ADMX Software

The experiment is controlled by a National Instrument LabVIEW Data AQuisition (DAQ) software package[20]. The DAQ controls all GPIB or RS232 attached instruments and uploaded all data off-site for analysis. The off-site analysis package, described in chapter 5, is written in C++ and allows the data to be processed with a host of libraries.

4.4.1 DAQ

LabVIEW organizes programs into Visual Interfaces, or VIs, with associated "wiring diagrams" that serve to acquire and process data. The ADMX LabVIEW DAQ uses 100's of custom VI's to control devices, run scripts, and regulate different aspects of the experiment. The primary VI consists of a directory of sub-VIs (figure 4.25). These sub-VIs allow for graphing data (figure 4.26), controlling the Network Analyzer (figure 4.27), controlling the main magnet, controlling the bucking magnet, controlling the stepper motors, controlling the ADCs, and controlling the data transfers. The primary VI's associated wiring diagram contains the main control loop that tunes the cavity, monitors the sensors, regulates the main magnet, and records the data. The primary VI also has an independent loop responsible for monitoring the bucking-system performance.

I was responsible for the maintenance and upgrading of the ADMX DAQ. While a func-

---

[20] The LabVIEW version 8 DAQ ran on a 2001 Dell Windows XP PC. LabVIEW 8 is now legacy, but the modern LabVIEW 2012 software is fully backwards compatible with the ADMX DAQ. Further information on LabVIEW can be found at: http://www.ni.com/labview

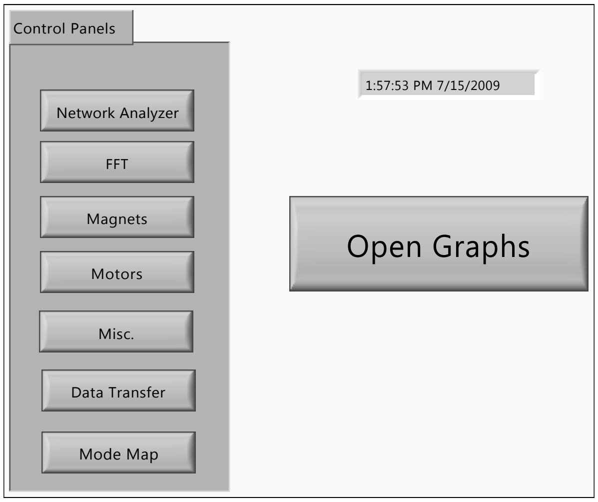

1:57:53 PM 7/15/2009

Figure 4.25: The Spartan front panel of the ADMX DAQ only provided access to other front panels, which accessed the variables and controls that operated the experiment.

tional DAQ was written for earlier ADMX operations, I completely reorganized the DAQ to be more modular. LabVIEW DAQs are composed of subroutines linked with data wires. While this architecture allows for simple parallel processing and quick prototyping, complicated DAQs, like ADMX's, can quickly become unmanageable. Originally, all output displays were integrated into the primary VI, requiring constant redrawing as the DAQ ran. By separating the displays from the primary VI, computer resources could be conserved, which were very limited on the 2001-era computer. My optimizations greatly improved DAQ responsiveness and stability. Instead of directly wiring sub-VIs within the DAQ, the DAQ called instances of sub-VIs. This allowed sections of the DAQ to be modified without having to interrupt data taking.

4.4.2 Field Control

Maintaining the zero field region around the SQUID is complicated by many factors. Current in the bucking magnet system is persistent while current in the main magnet is not. Also, the bucking coil has a much faster charging rate than the main magnet. The Hall sensors that measure the magnetic field produce heat near the temperature-sensitive SQUID, so they

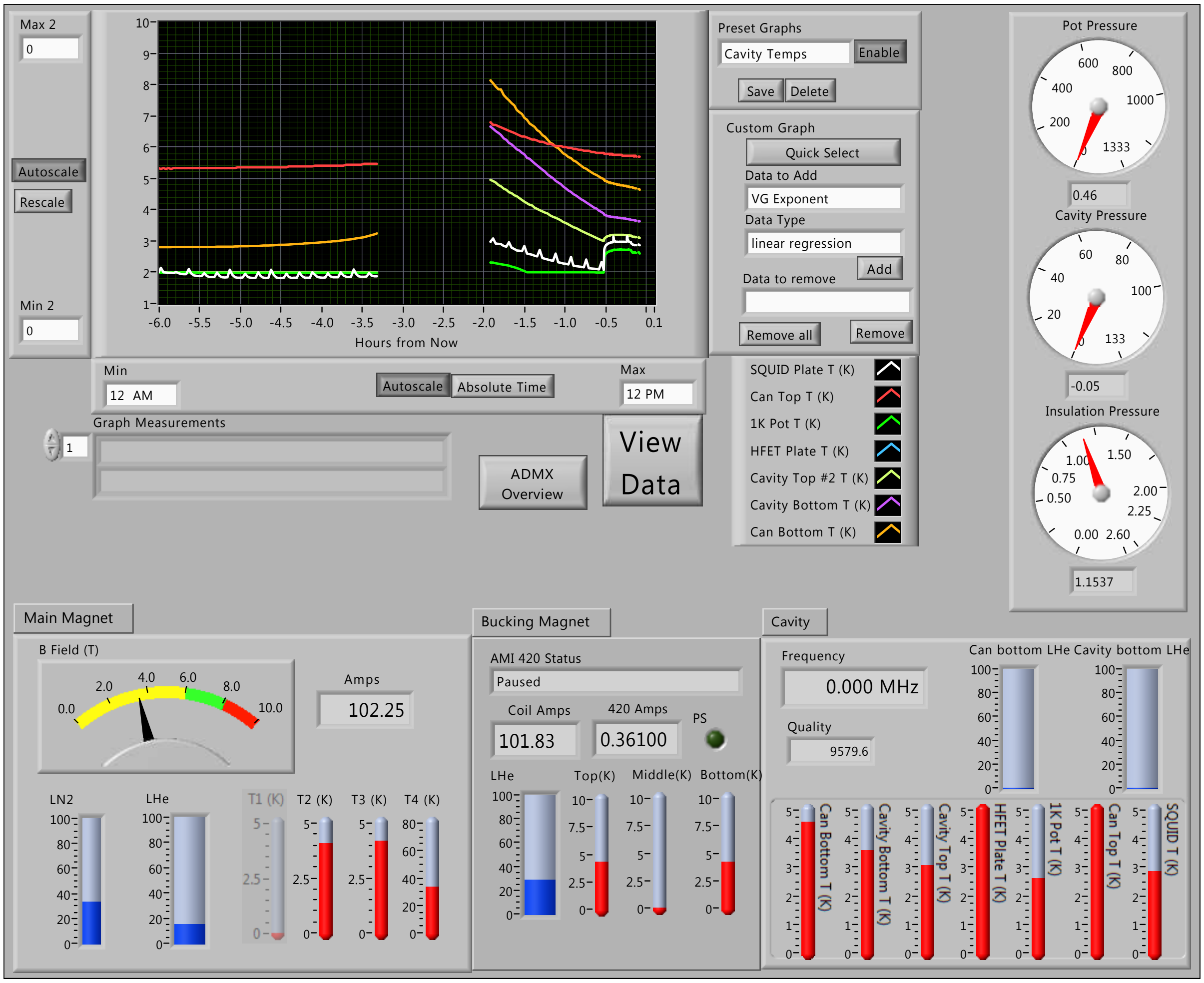

Max 2: 0

Min 2: 0

Preset Graphs: Cavity Temps

Data to Add: VG Exponent

Data Type: linear regression

Data to remove:

Min: 12 AM

Max: 12 PM

Pot Pressure: 0.46

Cavity Pressure: -0.05

Insulation Pressure: 1.1537

Amps: 102.25

AMI 420 Status: Paused

Coil Amps: 101.83

420 Amps: 0.36100

Frequency: 0.000 MHz

Quality: 9579.6

Figure 4.26: The graphs panel of the ADMX DAQ allowed for quick and easy access to all data values being recorded. Due to limited memory, only 24 hours of data was available for plotting within the DAQ.

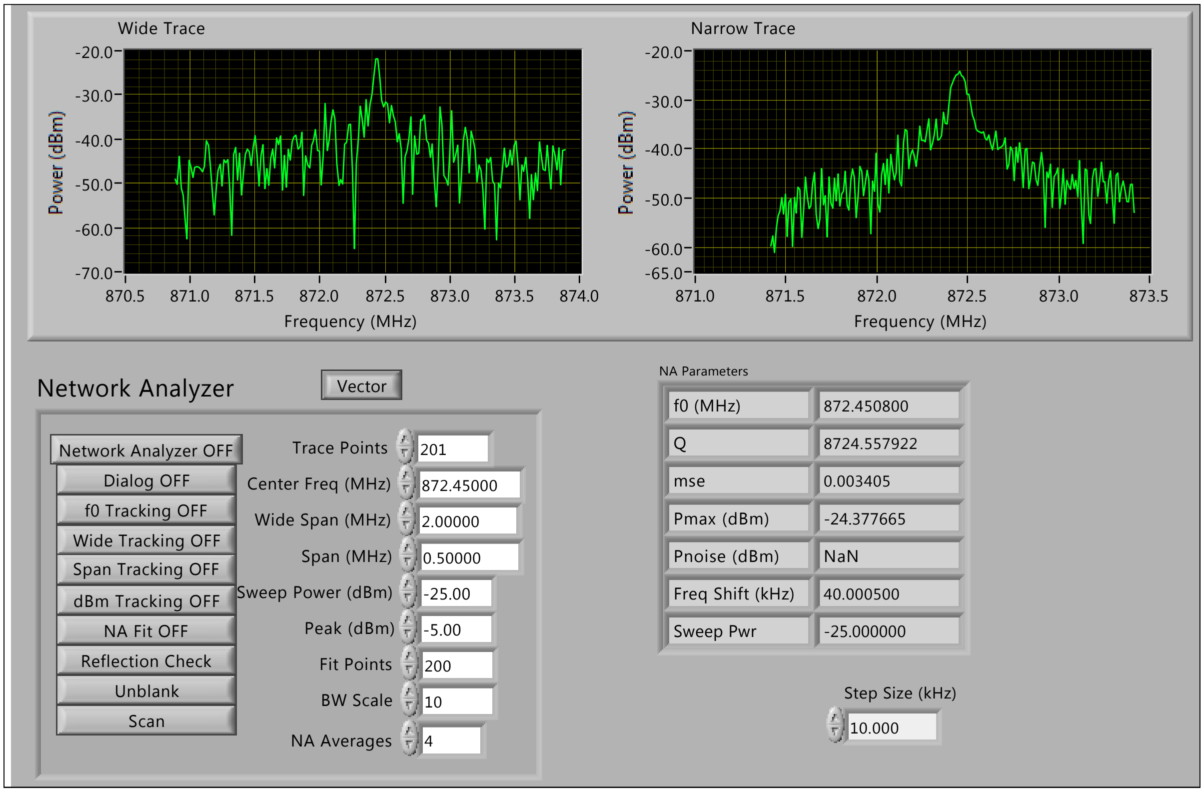

Trace Points 201
Center Freq (MHz) 872.45000
Wide Span (MHz) 2.00000
Span (MHz) 0.50000
Sweep Power (dBm) -25.00
Peak (dBm) -5.00
Fit Points 200
BW Scale 10
NA Averages 4

NA Parameters

f0 (MHz)	872.450800
Q	8724.557922
mse	0.003405
Pmax (dBm)	-24.377665
Pnoise (dBm)	NaN
Freq Shift (kHz)	40.000500
Sweep Pwr	-25.000000

Step Size (kHz) 10.000

Figure 4.27: Other panels controlled individual instruments. This panel controlled the functions and settings of the Network Analyzer.

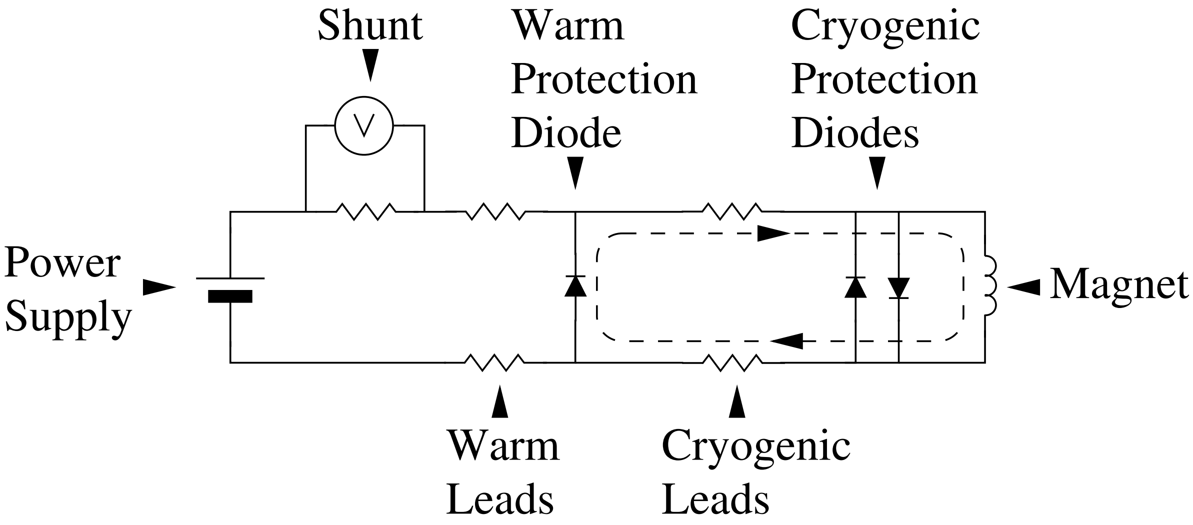

Figure 4.28: The circuit diagram of the main magnet. The continuous mode main magnet must always be supplied with current from room temperature. The power supply typically supplies this current, and the shunt resistor monitors this current. When the power supply is interrupted, the current loop looks like the dashed line, with current passing through the warm protection diode. This path does not pass through the shunt resistor, so the current in the main magnet is not directly measurable.

are only measured for a second every 10 minutes. The main magnet ramps down primarily through a protection diode at the top of its cryostat (figure 4.28), thereby removing the current-sensing shunt resistor from the circuit, which in turn prevents direct measurement of the main magnet's current during a ramp-down. The lack of a reliable way to measure the main magnet's current prevents a simpler, current-based control scheme. Instead, the Hall-effect sensors are used as the basis of the field-cancellation scheme.

The Hall-effect sensor outside of the Cryoperm shield is the most direct and reliable measurement of the applied field at the shield. Whenever the main magnet is ramping up or down quickly, this Hall sensor measures the field once a minute instead of once every 10 minutes, and whenever this sensor's field exceeds +/- 100 Gauss, the bucking magnet is ramped to over-cancel this field. The DAQ intentionally overshoots the optimal cancellation value in order to minimize the number of bucking magnet ramps since each ramp of the bucking coil has a small risk of quenching the bucking coil and halting the experiment.

The DAQ ramps the bucking-magnet circuit (figure 4.29) using a typical persistent-mode magnet ramping procedure. This procedure consists of energizing the leads to match the last measured current within the coil, then a heater warms the persistent switch above its critical temperature. This opens the persistent switch, creating a simple circuit between the magnet and power supply. The magnet is ramped to a new current, then the persistent switch heater is turned off. After the persistent switch cools back below its critical temperature, it closes, forming a continuous, near lossless, superconducting circuit. The leads are then de-energized to zero current. In order to minimize ramping the bucking coil, if the main magnet was ramping quickly, the bucking coil would overshoot the appropriate current to zero the field. This automated procedure minimizes Joule heating of the leads without compromising the zero-field region of the SQUID.

Within the LabVIEW DAQ, the main magnet's Proportional-Integral-Derivative control loop (PID) maintains a stable current or quickly ramps to a new set-point current. The PID loop uses the voltage across the main magnet, the change in current over time, and

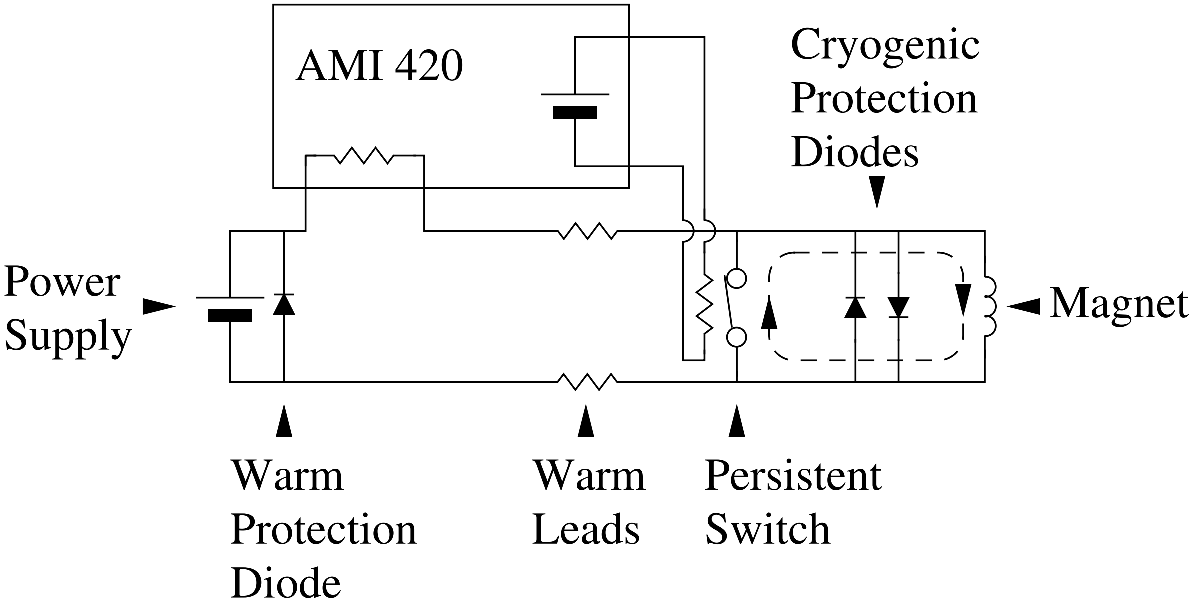

Figure 4.29: The circuit diagram of the bucking magnet. The persistent mode bucking magnet contains a superconducting circuit, shown as a dashed line, between the magnet and the persistent switch, allowing for the magnet to remain energized without an outside current supply. In order to ramp the bucking magnet, the superconducting circuit must be broken. This is accomplished by gently heating the persistent switch, driving it normal. If there is any current through the persistent switch when it is heated, then the bucking magnet may quench. As such, it is important to have smart electronic control over the bucking magnet, accomplished by an American Magnetics (AMI) 420 controller. The AMI 420 controls the persistent switch heater, measures the current going through the warm leads, and programs the power supply.

the current in order to determine the correct voltage of the main-magnet's power supply. The Hall sensors are still measured once every 10 minutes to monitor the fields. Due to the high inductance of the main magnet, if mains power is cut to the experiment, then it takes around an hour before the uncanceled field becomes large enough saturate the Cryoperm shields and enter the SQUID region. Furthermore, if the DAQ failed, the magnet supply would continue to output a constant voltage. The small, temperature-dependent changes in lead resistance would only cause a few ampere drift over the course of a day. In order to saturate the Cryoperm shield, the main magnet had to deviate 10 amps from its set point, corresponding to a 200 Gauss applied field. Once the Cryoperm shield saturates, any additional field is substantially unattenuated and enters the SQUID space. Any unattenuated field in the SQUID region eliminates the stable operation of the SQUID amplifier. At 100 Gauss of unattenuated field, corresponding to a 15 amp deviation of the main magnet, the circulator/isolator is destroyed and must be replaced before operations can resume; this requires a pull-out operation.

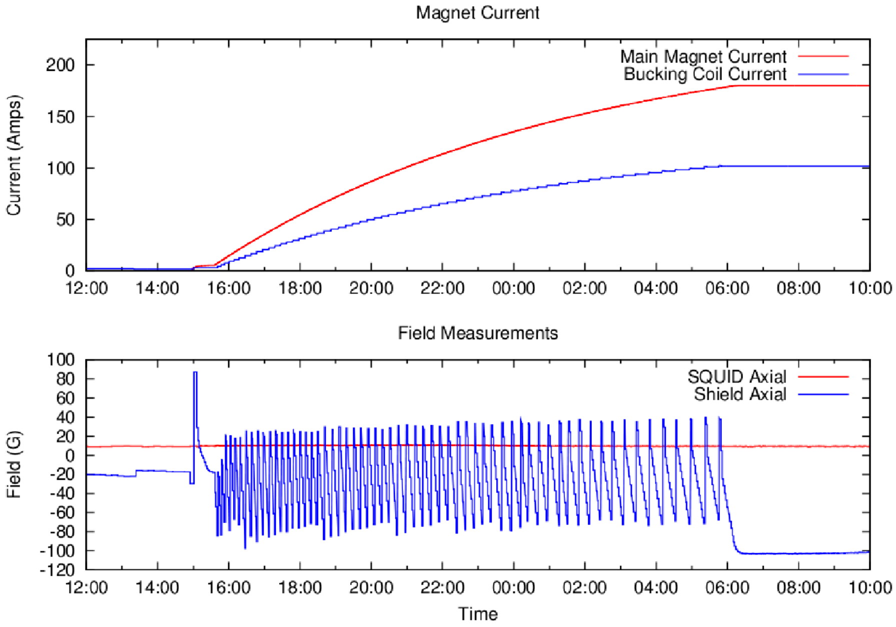

Figure 4.30: To prevent saturation of the passive shields around the SQUID, the bucking coil would have to be ramped simultaneously with the main magnet. However, the main magnet's 500 Henry coil took 24 to 36 hours to ramp. The bucking coil's vapor cooled leads were not designed for continuous operation, so it had to be ramped in stages. This was automated by the DAQ and triggered on Hall probe measurements.

Chapter 5

Data Analysis

5.1 Introduction

This chapter describes how the raw data from ADMX's LabVIEW DAQ is processed into a variety of exclusion limits for axion-to-photon coupling strength and for our Milky Way's dark-matter axion content. The DAQ saved spectral data of the axion-sensitive cavity mode for analysis. This data was filtered and processed to search for an axion-produced signal. The sensitivity of ADMX to an axion signal depends on the expected line-shape of the axion signal, which in turn depends on a model of the Milky Way's dark matter halo. This chapter applies several halo models to the ADMX search.

5.2 Data Set

The data used in this thesis was acquired by ADMX during the May 2008 to April 2010 run. During this run, ADMX searched for axions with total energies ranging from 812 MHz to 892 MHz at roughly KSVZ axion-to-photon coupling strength. The frequency of the cavity's axion-sensitive TM_{010} mode over this time is shown in figure 5.1. Overall, the DAQ generated roughly 350,000 unique spectral data files, each containing either a time series or power spectrum, altogether totaling over 2 Terabytes of raw data.

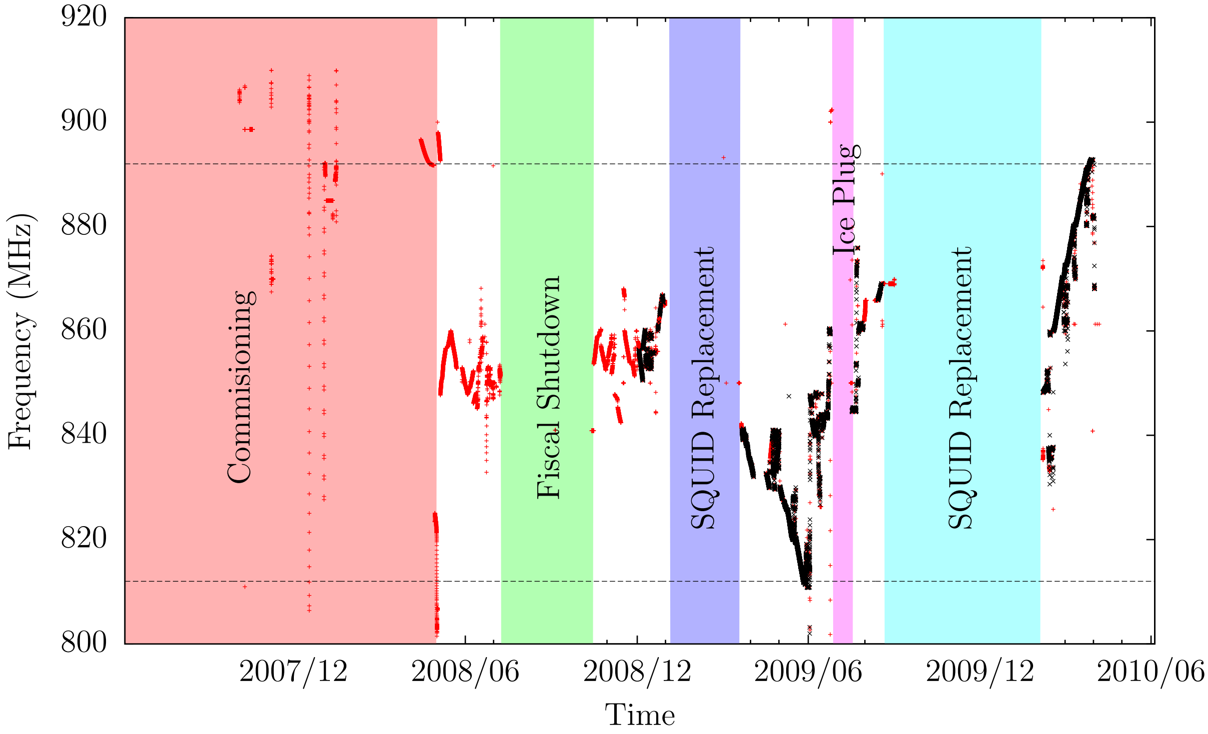

Figure 5.1: The tuning frequency of the cavity vs time for the entire data set. Red points indicate either tunings that did not capture spectra or where spectra were discarded for a variety of reasons. Black points indicate tunings where the saved spectra were used in this analysis. The shaded regions indicate periods where the experiment was inoperable, with a label giving a short explanation for the down-time. The horizontal lines indicate the upper and lower boundaries on frequency for the limits produced from this data set. Production data taking began in 2008/05, but before 2008/09, the high resolution data had too little bandwidth to be useful (8 kHz vs 30 kHz). Much of the red, cut data from 2008/05 to 2008/12 was taken on cavity modes other than the TM_{010}.

Due to a variety of reasons, data taking operations halted several times. The first major down-time was from June of 2008 to October 2008, which was due to a funding shortfall during a congressional continuing resolution that prevented the purchase of the LHe necessary to cool the magnet and insert. Operations resumed in October of 2008 and continued until November. A power failure in November caused the bucking system to de-charge and subject the SQUID and isolator to destructive magnetic fields, requiring a hardware repair. Operations resumed in December of 2008 and continued until January of 2009, when the SQUID stopped amplifying, regardless of bias setting, and it needed to be replaced. Operations resumed in March of 2009 and continued until June, when a broken o-ring caused the cavity tuning system to freeze. ADMX operated from August to September of 2009 then ended when a second SQUID failed similarly to the first. From February 2010, ADMX was operated without a SQUID amplifier, relying on the HEMTs as the primary cryogenic amplifiers, until the end of the run in April 2010.

As described later, quality controls discard questionable data, resulting in a useful data set of 277,652 unique spectra or time series processed into limits. Figure 5.2 shows the integrated number of these useful spectra or time series throughout the 2008 to 2010 operations. Table 5.2 shows the formatting of the various files used to store ADMX's data. The data format of spectra files taken before April 2009 is a 953,420 point power spectrum that is the average of 3 sequential power spectra taken with the same cavity tuning. After April 2009, time series files contain 1,906,840 sequential voltage measurements from the ADC. Appendix D describes why the data format was changed. A small "state data" file contains the measurements from all of ADMX's sensors for every cavity tuning. These state data files are loaded into an SQL database to facilitate the searching, sorting, and processing of spectra. The associated state data for any spectra is recovered by simply searching the database with the spectra's unique time stamp.

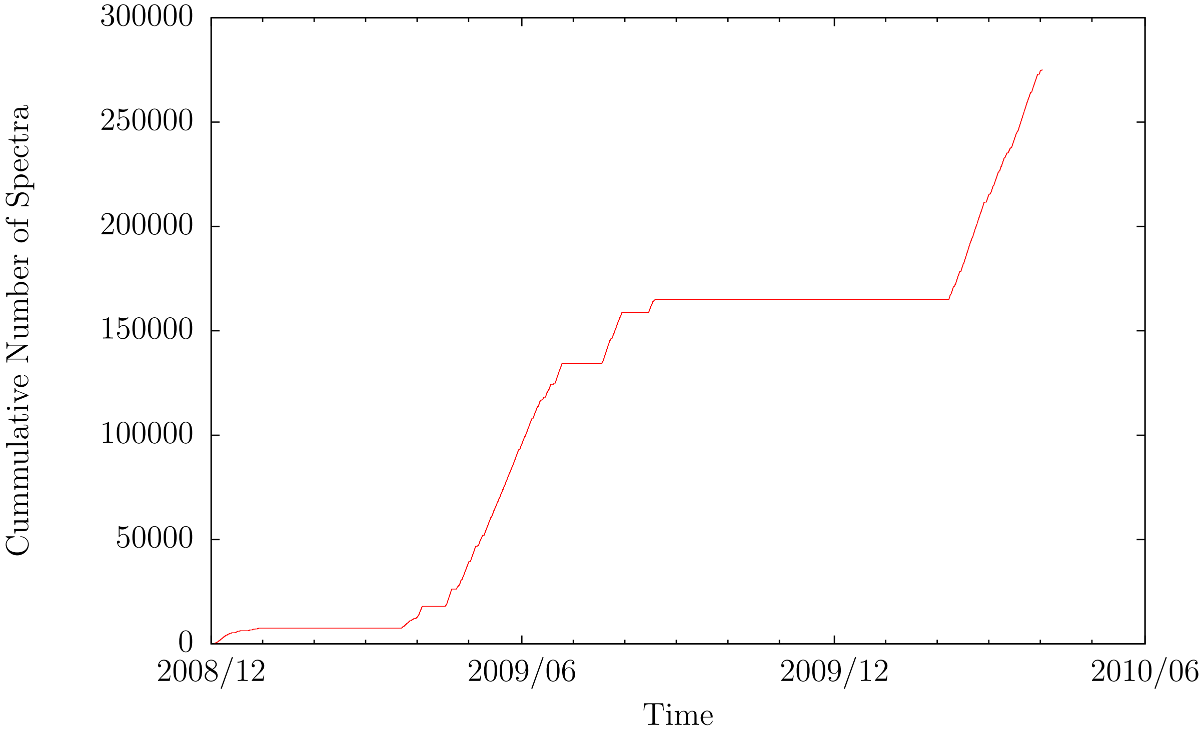

Figure 5.2: The cumulative number of spectra used in this analysis vs time. In September of 2009, the second ADMX SQUID died and could not be replaced before the end of running. Instead, the HFET amplifiers were used from February 2010 until April 2010.

Power Spectra File		
Name	Format	Size
Number of Spectra	I	1
Parameter Names	C	4002
Parameter Values	D	200
FFT Parameters	F	3
Spectrum Points	F	953,420

Time Series File		
Name	Format	Size
Parameter Names	C	4002
Parameter Values	D	200
Time Series Points	F	1,906,840

State Data File		
Name	Format	Size
Number of Sets, N	I	1
Parameter Names	C	4002
Parameter Values	D	200
Repeat above line N times		

Formats		
Type	Symbol	Bytes
Character	C	1
Integer	I	4
Float	F	4
Float	D	8

Table 5.1: The organization of the data files produced by ADMX's DAQ. All stored numbers are in big endian byte order. While the power spectrum files supported having more than one spectrum inside of them, all such files stored a single spectrum. For the time series files, an error in Labview produced garbage data in the parameter values, requiring the state data files to read appropriate parameter values. Typically, a single state data file saved all of the parameter values for a day. Note that the size column refers to the number of instances in a given format, not the number of bytes.

5.3 Data Processing

5.3.1 Analysis Software

The analysis package consists of thousands of lines of C++ code. Originally developed to handle the small (roughly 1 kB in size) spectra produced by the SRS Spectrum Analyzer, the analysis package was modified to process the much larger files (roughly 1 MB) from the National Instruments ADC. The analysis package is written with object-oriented code, with the end goal of integration into a DAQ for real-time analysis. The code is organized into directories: data management, which contains structures and functions for storing and manipulating spectra; math functions, which contains the often complicated functions necessary for analysis; graphing, which contains the graphing and plotting functions; spectrum processing, which contains filters and flattens the raw spectral data from the DAQ; and spectral analysis, which contains the algorithms necessary to generate the science results.

A significant addition to the analysis package is the integration of an SQL database, PostgreSQL, which allows for the organizing, searching, sorting, and management of all ADMX data. Originally, the analysis package was controlled by BASH shell scripts. This method became unwieldy with the large data-sets, long analysis times, and several analysis channels. The SQL database allows for quick selection of spectra or data based on a variety of factors, eliminating the need to maintain list files and eliminating the need for most BASH scripts in the analysis package.

All analysis is performed in frequency space by performing a Fast Fourier Transform (FFT) on the voltage time series recorded by the ADC. The ADC records 1,906,840 sequential 16 bit voltage samples at a sampling rate of 80,000 Samples/second. The LabVIEW DAQ performs an FFT with a Hann window on each time series, average three sequential spectra together, then saves the resulting power spectrum. From April 2009 onward, each individual time series was also saved. These time series were later transformed with FFTW v3.3[1] using a square window, improving the effective integration time relative to the Hann window of LabVIEW's FFT by a factor of 2. Appendix D demonstrates this improvement of the FFTW-generated power spectra compared to the LabVIEW generated power spectra.

The default frequency resolution of a spectrum is defined by its Nyquist resolution, which is the inverse of the integration time (23.8355 seconds). By adding each N adjacent points, or bins, within a spectrum, the frequency resolution of the spectrum is decreased by N. Reducing the resolution of a spectrum by N only increases the noise by $\sqrt{\mathrm{N}}$, increasing SNR by $\sqrt{\mathrm{N}}$ for a signal N bins wide. However, decreasing the resolution beyond a signal's expected width adds noise to the signal and decreases the Signal-to-Noise-Ratio (SNR). These two effects require that, for optimal SNR, the analysis must be performed with the same resolution as the expected signal's bandwidth, as demonstrated by figure 5.3. A difficulty for this analysis is that the signal's expected bandwidth has a range of possible values from various models, so much of the analysis is performed at the full Nyquist resolution of .04195 Hz.

---

[1] FFTW is an open source discrete Fourier transform package for C++. It quickly and exactly transforms data with fast O(N log N) algorithms. More information is available at http://www.fftw.org/

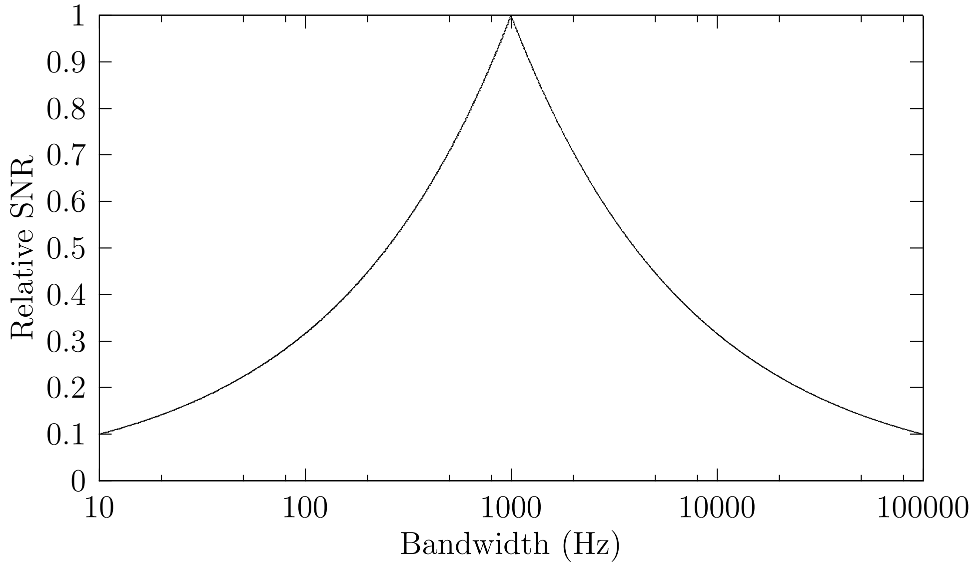

Figure 5.3: For a square signal, the maximum sensitivity is achieved on a knife edge in bandwidth, in this case 1000 Hz. Since the axion signal bandwidth is not well defined, multiple bandwidths are analyzed.

The analysis package processes the raw spectra into exclusion limits with several steps. First, all spectra are "conditioned", which removes any instrument related structures from the spectra, as described later in subsection 5.3.3. During the conditioning step, spectra are saved or discarded according to a rule-set, as described in subsection 5.3.2. The resulting conditioned and quality-controlled spectra are saved to disk. These spectra were then combined into a "grand" spectrum, as described later in subsection 5.3.4. From this grand spectrum, various exclusion limits are calculated.

5.3.2 Quality Control

The LabVIEW DAQ saves all data: any spectra that is successfully recorded is saved to disk. Many of these spectra are insensitive to an axion signal for a variety of reasons. Including these spectra in the analysis would, at best, lengthen analysis and, at worst, misrepresent the sensitivity of ADMX; therefore, these spectra are removed from the analysis by checking each spectrum against a list of quality-control rules. Table 5.2 shows the full list of quality-control cutting rules, which discard any data for which the rule is true. These rules are organized

Cut Rule	Reason
Level 1	
Any Value = NaN	Data is malformed
Level 2	
$f0 < 600$ or $f0 > 1100$	Frequency outside of data set range
$Q < 10$ or $Q > 100000$	Quality factor far outside of typical cavity Q
Cavity Bottom T< .1 or Cavity Bottom T> 10	Science based temperature either anomalously cold or too hot to be sensitive
2008-12-02 to 2010-01-01 with $FFT_{AVG} < -55$	SQUID gain was too low for SQUID to be effective amplifier
B Field < 1 or B Field > 10	Magnetic Field was either too low for science data or anomalously high
2009-06-24 to 2009-07-14	Data was taken during Chameleon search
2008-10-01 to 2008-11-16	Data taken with cavity on wrong mode
2008-11-15 to 2008-12-02	Bucking system failed, resulting in SQUID death
2008-12-18 and 2008-12-22	Peak injection test caused too much sideband noise to be useful
2010-02-19 to 2010-03-01 with radio peaks	A large list of cuts to eliminate large radio peaks introduced by a broken cable
Level 3	
Receiver fit $\chi^2/DOF > 1.2$ or $\chi^2/DOF < 0.8$	Poor receiver fit produces excess structure

Table 5.2: The cut rules that discard data when true. The level 1 rule is checked first and discards malformed data. Level 2 rules are checked before "conditioning" while the level 3 rules are checked after conditioning.

in 3 levels, which are applied at various stages of conditioning. First-level rules discarded spectra that contain "bad" values. For example, whenever the Labview DAQ is initially executed, some instruments might be recorded as the default ISO (International Organization for Standardization) NaN (Not a Number), which is the floating point representation of a non-finite value.

Second-level rules remove spectra based on their experimental parameters. For example, data taken with the magnet off would not contain an axion signal. While most second-level rules test sensor readings, some only remove data within a range of times. The most numerous of these time-based rules are in response to a broken RF cable, which allowed for local radio signals to enter the receiver during running from late 2009 to early 2010. These

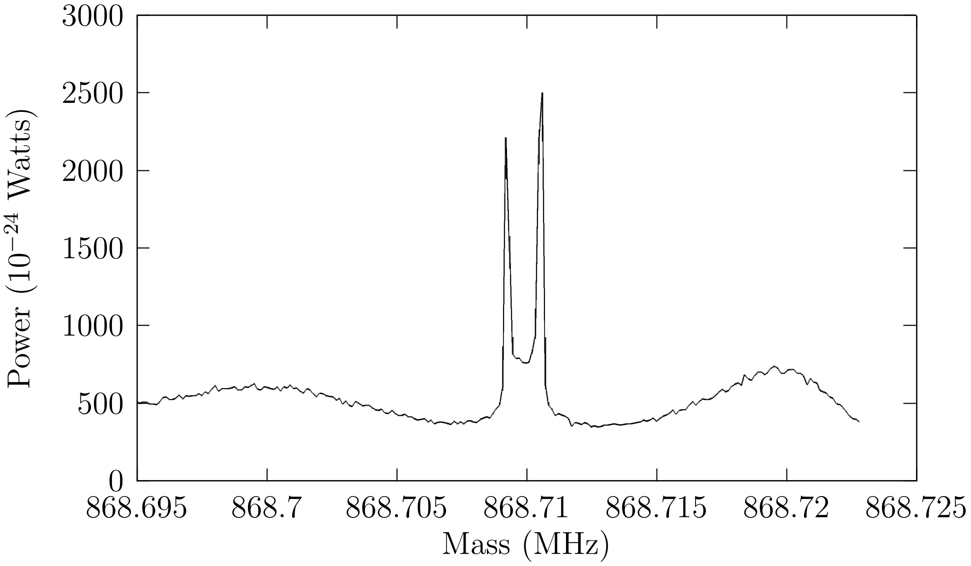

Figure 5.4: A processed spectrum with a huge radio peak. A broken cable during some of running introduced dozens of large external signals into the data set. These radio peaks were identified by their extreme signal levels with multiple sidebands, as shown in this plot. All spectra were discarded during times when the cavity was tuned to a discovered radio peak, creating holes in the data set. Once the cable was replaced, the holes had to be revisited to be filled in.

large radio signals, like those shown in figure 5.4, dwarf any potential axion signals and often saturate the receiver's dynamic range. The large amplitude of the peaks, $> 10\times$ the expected axion signal, allow for simple identification and elimination without compromising the integrity of the axion search. The frequencies with these excessively large signals were revisited after the cable was repaired and no peaks were found.

As discussed in the next section, spectra contain structures imparted by various components of the receiver. These structures are removed. The success of this removal is parametrized by a χ^2/DOF goodness of fit. Any spectra with a large χ^2/DOF is discarded, like the spectrum shown in figure 5.5. Spectra discarded from third-level rules were typically recorded when the receiver overheated and its transfer function became unstable.

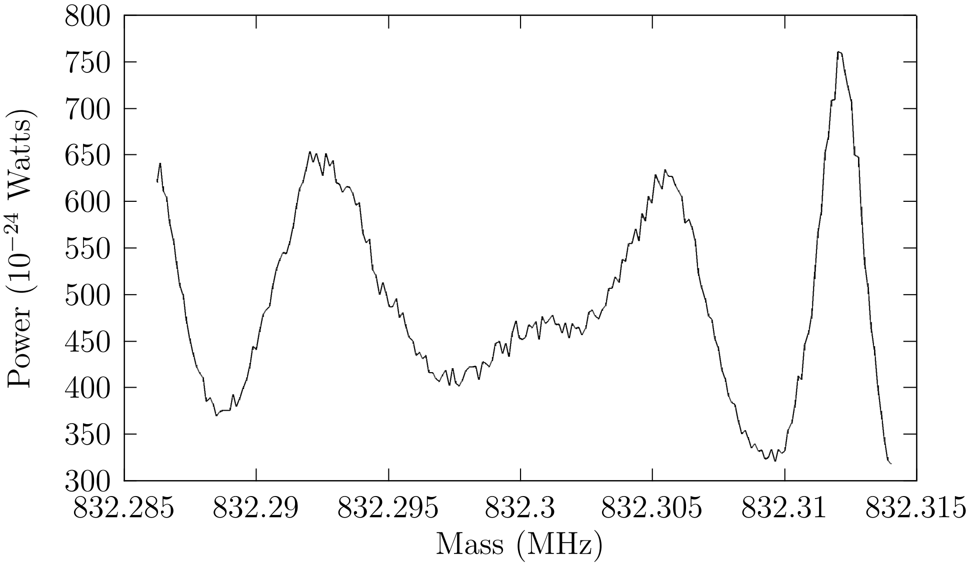

Figure 5.5: A conditioned spectrum with excessive structure. Even if this spectrum contains an axion signal, the receiver structures would dwarf the axion signal, so this spectra is discarded.

5.3.3 Spectral Processing

Table 5.3.3 shows an overview of the analysis steps. The power spectra record the power vs frequency output of the receiver. In order to measure the power of an expected axion signal, the "raw" recorded spectra needs to be processed into flat spectra with units of expected axion signal power. The first step of this process is to remove the transfer function of the cavity-amplifier-receiver chain from the spectra. An axion signal might be masked by the non-uniformities in a raw spectrum, so these structures are removed.

Figure 5.6 shows a typical raw spectrum, which has an obviously non-uniform transfer-function on top of the noise distribution. This structure is removed in two steps: first the large "static" structure is removed then the small "dynamic" structure is removed. The large, static structure originates from the receiver, primarily the crystal filter inside the receiver, so the static structure is parametrized by an "xtal" spectrum. An xtal spectrum is calculated by averaging all of the spectra for a single day. The "static" structure slowly changed over time[2], requiring daily calculation of xtal spectra. The raw spectra are divided

---

[2] The xtal filter has been measured to change over time, but the xtal filter is also temperature sensitive.

Spectrum Name	Units	Description	Figure
Raw	nW	The unprocessed power spectrum	5.6
Xtal	Normalized	The time-averaged shape of the receiver	4.22
Postxtal	Normalized	The Raw divided by the Xtal	5.7
Trimmed	Normalized	The Postxtal spectrum with edges discarded	5.8
Fit	Normalized	A 5th order polynomial fit to the Trimmed	
Post-fit	Normalized	The Trimmed spectrum divided by the Fit	5.9
Power-in-cavity	Yoctowatt	Trimmed multiplied by the Nyquist noise	5.11
Excess-power	Yoctowatt	Power-in-cavity with its mean subtracted	
Excess-axion-power	Expected Signal	Excess-power divided by the expected signal strength	
Grand	Expected Signal	All Excess-axion-power spectra added together in ν-space	

Table 5.3: The spectra in the analysis. They are organized in order of usage through the analysis. Spectra saved to disk are Raw, Power-in-cavity, and Grand. All other spectra are typically discarded from memory after processing is complete.

by the xtal spectrum from the same day, resulting in a mostly flat, “postxtal” spectrum shown in figure 5.7. The edges of the “postxtal” spectrum are outside of the bandpass of the receiver, so they are discarded, generating the “trimmed” spectrum shown in figure 5.8.

The cavity, transmission line, and SQUID amplifier produce a transfer function that changes with each tuning of the receiver, generating a dynamic structure in the spectra. The dynamic structure is removed from the trimmed spectrum by a polynomial fit of order five. The choice of a 5^{th} order polynomial is a compromise: it removes most structure without attenuating potential signals. The MIGRAD minimization function of the MINUIT package is used to fit the polynomial to the trimmed spectrum[3]. The resulting fit parameters generate a fit spectrum, which is divided from the trimmed spectrum to produce a flat, “post-fit”

During summer running, the receiver box sometimes overheated, producing a changing xtal structure

[3] The full 0.042 Hz resolution spectrum is not directly fit: instead a lower resolution spectrum is generated by averaging adjacent bins until the resulting spectrum has less than 100 points. This is necessary for two reasons: the fit is 1000 times faster without sacrificing quality and the MIGRAD minimization function assumes Gaussian statistics, which the full 0.042 Hz resolution spectrum did not have, but the ¡100 point spectrum did.

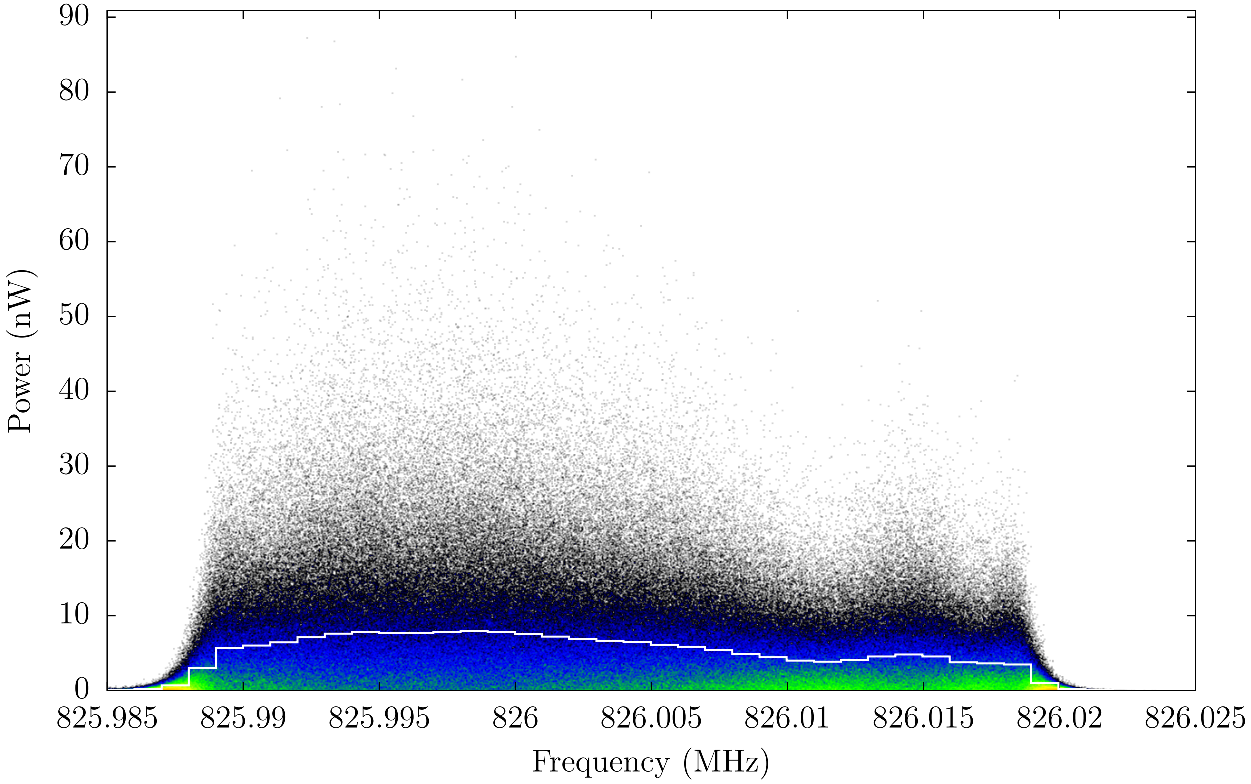

Figure 5.6: An unprocessed or "raw" power spectrum. The background of the plot is to a 1200 point wide by 800 point tall logrithmic 2D color-coded histogram of a spectrum with a frequency resolution of 0.042 Hz. The horizontal axis is frequency and covers the 40 kHz wide bandwidth of the ADC. The vertical axis is power in each bin. The 2D color-coded histogram is base 10 logarithmic with 0 as white, 1 as black, 10 as blue, 100 as green, 1000 as yellow, 10,000 as orange, and 100,000 as red. The white line is derived from the same spectrum that generated the histogram, but with every 23808 adjacent bins averaged to generate a frequency resolution of 998.846 Hz. The ADMX receiver imparts the noticeable non-uniform structure seen in the spectrum.

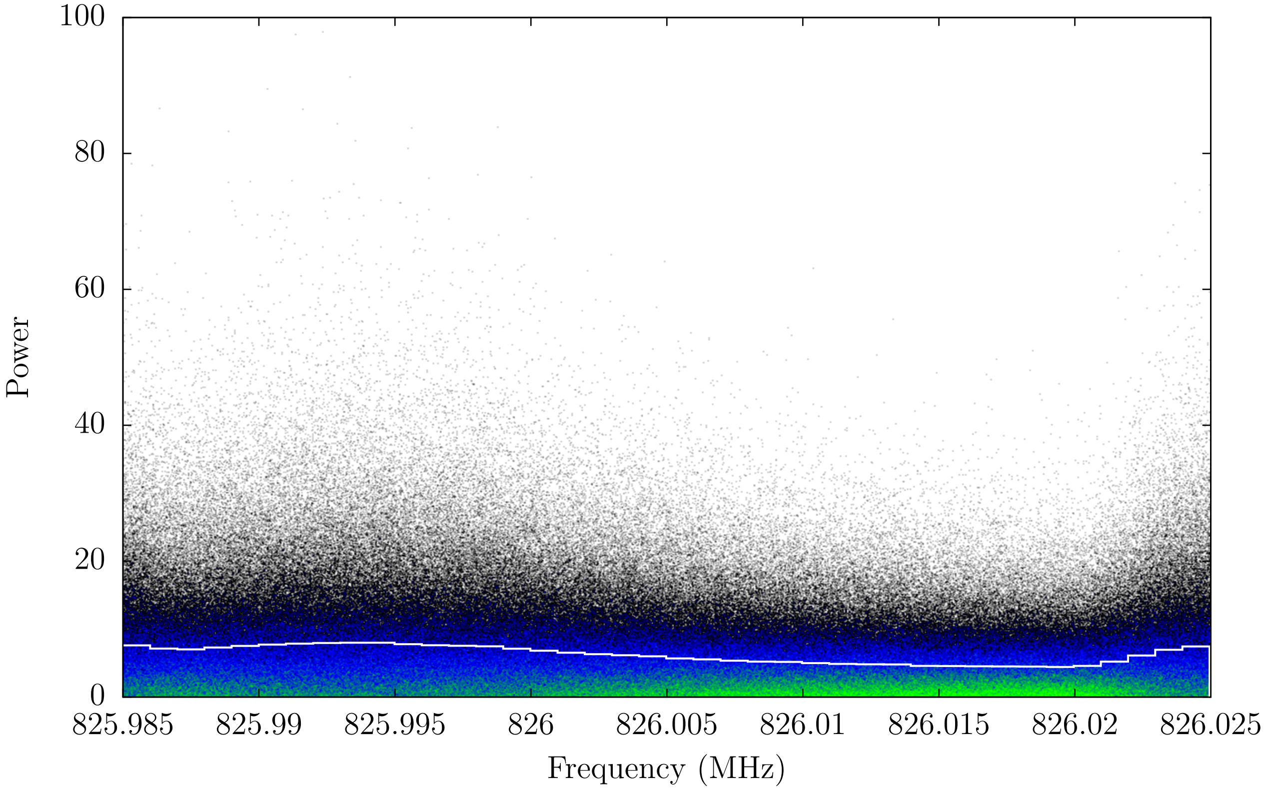

Figure 5.7: The spectrum in figure 5.6 after removing the static component of its receiver-related structure, generating a "postxtal" spectrum. The axes are the same as in figure 5.6 except that vertical, power axis is now in arbitrary units. This spectrum is generated by dividing the raw spectrum in figure 5.6 with a daily average of all raw spectra.

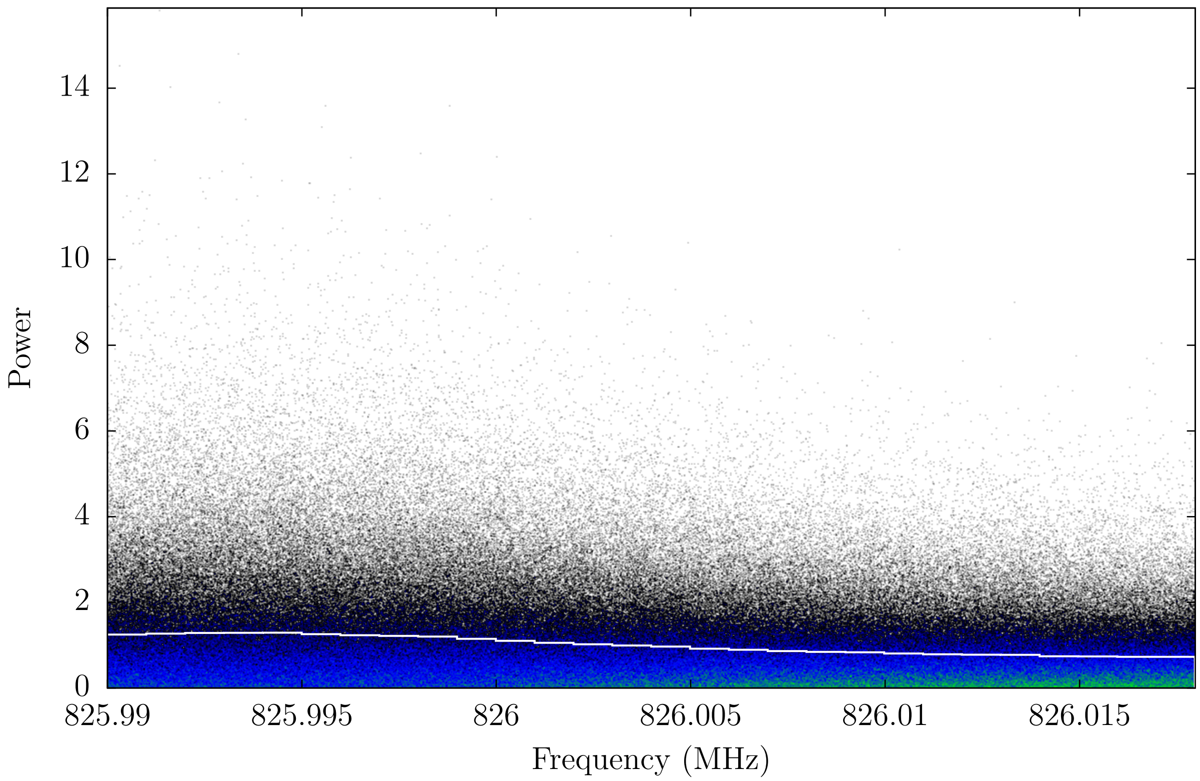

Figure 5.8: The spectrum in figure 5.7 after discarding the sides of the spectrum, generating a "trimmed" spectrum. The axes are the same as figure 5.6 except that the vertical, power axis is in units of the average power of the spectrum. The sides of the recorded spectra are outside the bandpass of the receiver and are noisy, so they are discarded.

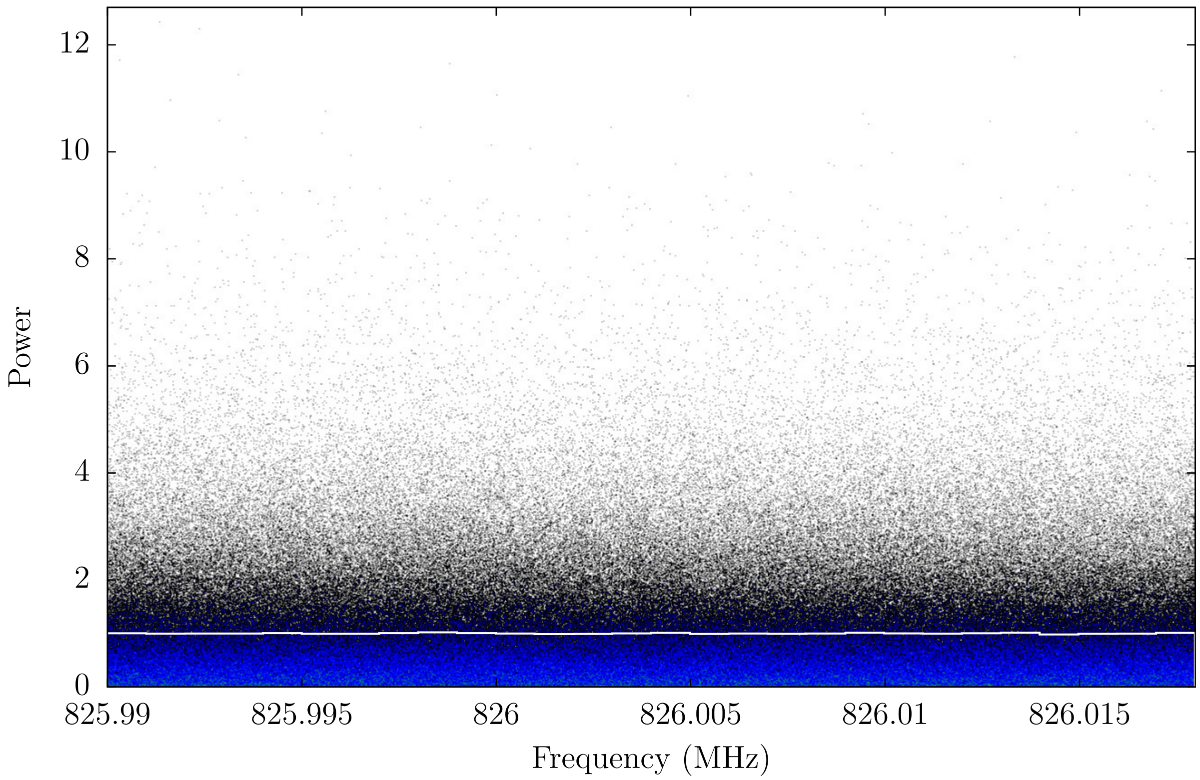

Figure 5.9: The spectrum in figure 5.8 after removing the dynamic component of its receiver-related structure. The axes are the same as figure 5.6 except that the vertical, power axis is in units of the average power of the spectrum. The dynamic structure is removed by first fitting a 5th order polynomial to a reduced frequency-resolution trimmed spectrum. The resulting fit parameters are used to generate a fit spectrum with the same frequency resolution as the trimmed spectrum. The trimmed spectrum is divided by this fit spectrum to generate a post-fit spectrum that is free of receiver-related structure.

spectrum shown in figure 5.9. The χ^2 per degree of freedom (χ^2/DOF)of the polynomial fit is a measure of the goodness of fit. The distribution of χ^2/DOF for all of the fitted spectra had clear outliers, which have excessive structure. The quality control rules to discard these outliers are hand tuned to discard these bad spectra without discarding useful spectra.

The post-fit spectra look as expected for a power spectrum of Johnson noise, like the expected noise generated by the cavity and amplifier. Johnson noise produces Gaussian random voltages in the time-series. When this time-series is converted to a power spectrum

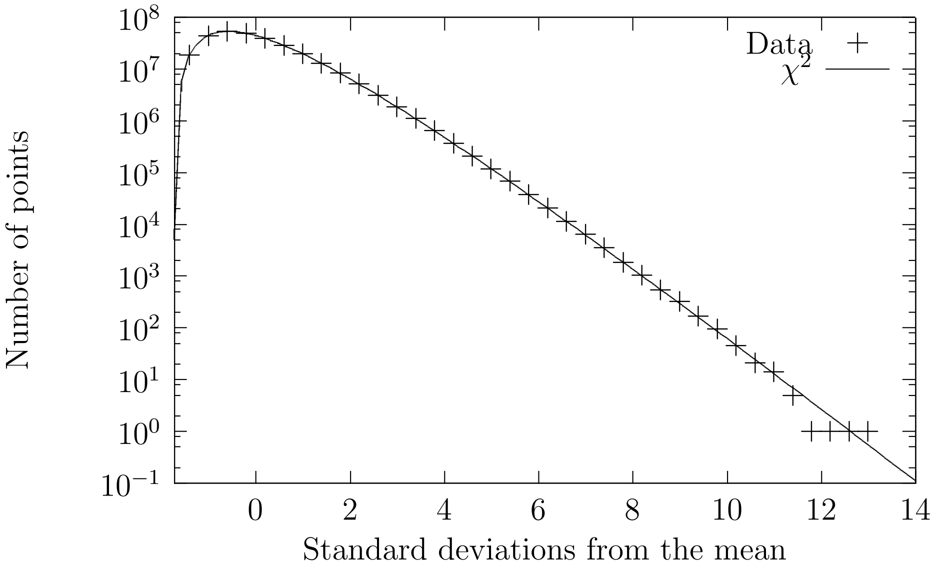

Figure 5.10: The normalized deviations around the mean of roughly 1000 power spectra FFT'd by LabVIEW. The data fits well with the expected χ^2 distribution of order 6^5. A poor receiver subtraction or fit would cause a deterioration of the fit.

with a discrete Fourier transform, the resulting power spectrum is flat, with a the values of the power spectrum obeying a χ^2 distribution of degree 2. Figure 5.10 shows the deviations from 1 day of flattened spectra. The agreement between the measured distribution and a χ^2 distribution of degree 2 allows for only minimal non-Johnson noise signals or structures. Due to this agreement, the flattened power spectra are interpreted to be measurements of the total system noise, which is dominated by the cavity's Johnson noise and the SQUID amplifier's noise. Equation 4.2 dictates the expected average noise power from the cavity and SQUID system. Therefore, the flattened spectra, with a mean value normalized to 1, are multiplied by the power predicted by equation 4.2, generating a "power-in-cavity" spectrum with units of power in yactowatts, shown in figure 5.11.

An axion signal would appear as an excess above the noise inside the cavity, so the mean of the power-in-cavity spectrum is subtracted from the power-in cavity spectrum, creating an "excess-power" spectrum. The uncertainty of each value within the power spectra are tracked through the remainder of the analysis. This uncertainty is initialized as the standard-deviation of the entire excess-power spectrum. Tracking the uncertainty of individual values

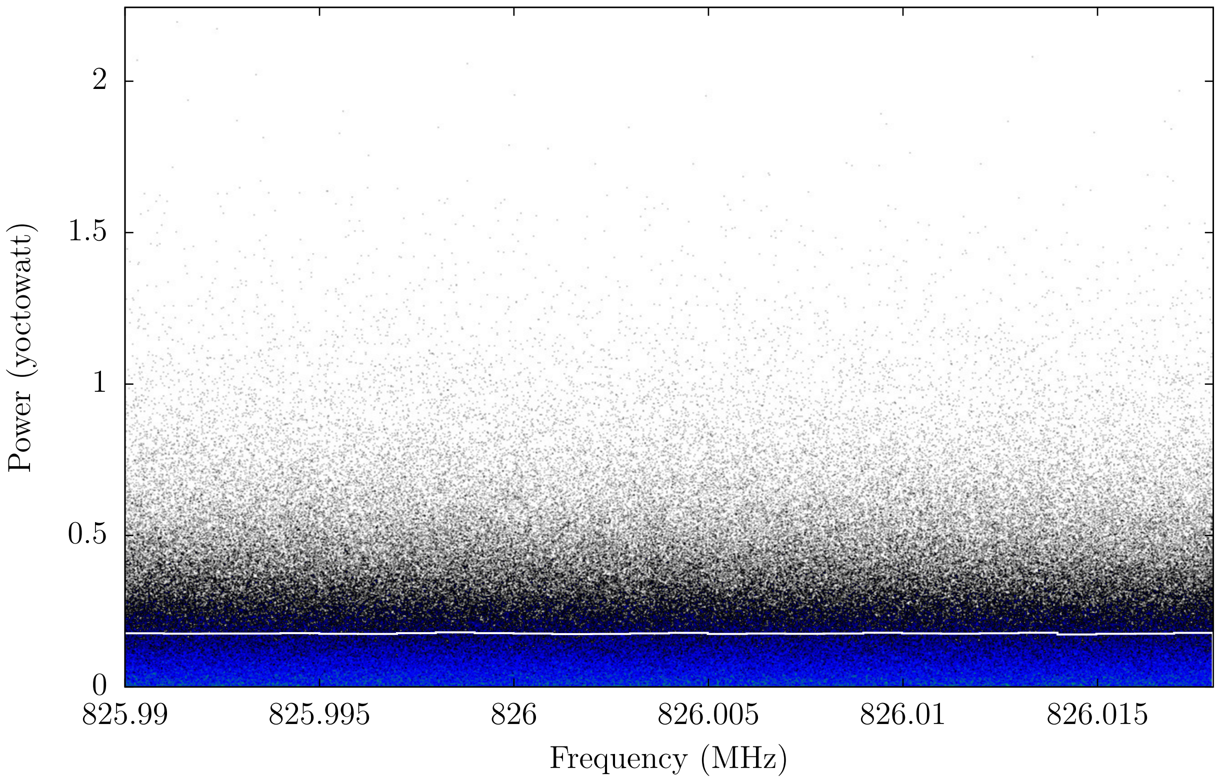

Figure 5.11: A spectrum that has been flattened then scaled to its appropriate system noise power.

is important since an expected axion signal in not uniform across the excess-power spectrum. The expected axion signal power is given by equation 4.1 multiplied by a factor of $\frac{1}{2}$ for the cavity critical coupling and weighted by the Lorentzian shape (figure 4.9) of the cavity mode. This Lorentzian shape produces stronger expected axion-signals in the middle of a power spectrum than its sides. The excess-power spectrum is divided by these factors to produce an "excess-axion-power" spectrum. These spectra have units such that the power generated from $0.45\frac{GeV}{cc}$ density, KSVZ coupling axion decaying into a single point of the power spectrum would produce an expected value of 1. The set of excess-axion-power spectra generated from all recorded data form the data set that a variety of analyses use to search for axions.

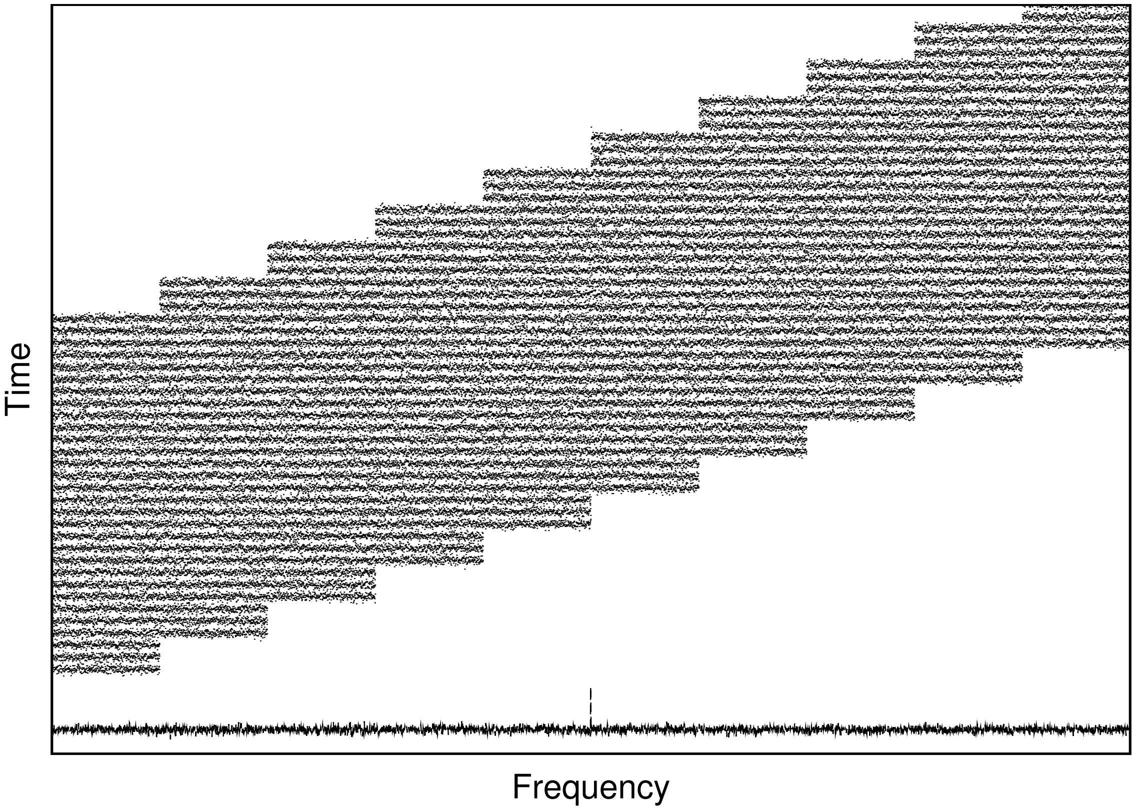

Figure 5.12: A sketch of how the grand spectrum (lowest spectrum) is generated from individual spectra. All the values at a single frequency are error-weighted averaged together to form the grand spectrum's value at that frequency. The vertical axis represents both time, with 1300 seconds of total integration time, and arbitrary power for the spectra. Individual spectra are represented by a fuzzy horizontal line. Three spectra were taken at each tuning frequency, then a 2 kHz step was taken. Each spectrum took 23 seconds to integrate and had an fixed injected signal with an SNR of 3, which is not statistically significant in any one spectrum. Combining spectra allows for the injected peak to become statistically significant, which is clearly visible at the center of the grand spectrum.

5.3.4 Limit Generation

The spectra of the excess-axion-power dataset are added together to form a single excess-axion-power spectrum, named the "grand" spectrum, that spans the entire 812 MHz to 892 MHz dataset. The grand spectrum is generated by uncertainty-weighted-averaging all excess-axion-power spectrum values with the same frequency[6] together, as shown in figure 5.12. The appropriate excess-axion-power spectra for each 1 MHz wide region are selected from the

---

[6] Due to arbitrary frequency differences between spectra, there is a maximum frequency error of the resolution or .0042 Hz

larger dataset with an SQL database. Since all analyses based on this grand spectrum search for relatively wide (> 1 Hz) axion signals, the grand spectrum is reduced in frequency resolution to 10.74 Hz by adding each adjacent 256 values, as discussed earlier.

During data-taking, any points with excess power were revisited to further investigate potential axion signals. The analysis described in this thesis was written after data-taking halted, so further scrutiny is not possible. As such, results are presented as exclusion bounds, with the assumption that there is no signal within the dataset. The grand spectrum contains all the axion-sensitive data from the entire 2008 to 2010 data-run and spans 812 MHz to 892 MHz. Each point of the grand spectrum contains a value and associated uncertainty in units of expected power from a KSVZ coupled, $0.45GeV/cc$ density axion signal. Generating an exclusion limit from the grand spectrum requires first choosing a confidence level, 90% unless otherwise specified, and calculating the corresponding number of deviations from the mean for this confidence level. For each point within the grand spectrum, the point's value is added to its confidence-adjusted uncertainty to produce an exclusion limit for each point. The largest exclusion limit for any point within a 1 MHz wide division of the grand spectrum is recorded as the exclusion limit for that division. The collection of all such limits produce an exclusion limit plot for the dataset. Just like the grand spectrum, the limit plot is in units of expected axion-conversion power, which assumes an axion-density of $0.45GeV/cc$ and a KSVZ axion-to-photon coupling strength.

5.4 Limits on Axion-to-Photon Coupling

As discussed in chapter 3, the simplest and most common model for the distribution of the dark matter in the Milky Way is an isothermal sphere. The resulting energy distribution of dark-matter axions is described completely by three parameters: the velocity of the sun around the galaxy ($v_{sun} = 220 \pm 20$ km/s), the virial velocity of the dark matter at the sun's location ($v_{disp} = 270 \pm 70$ km/s), and the local density of dark matter ($\rho = 0.45 \pm .3$ GeV/cc).

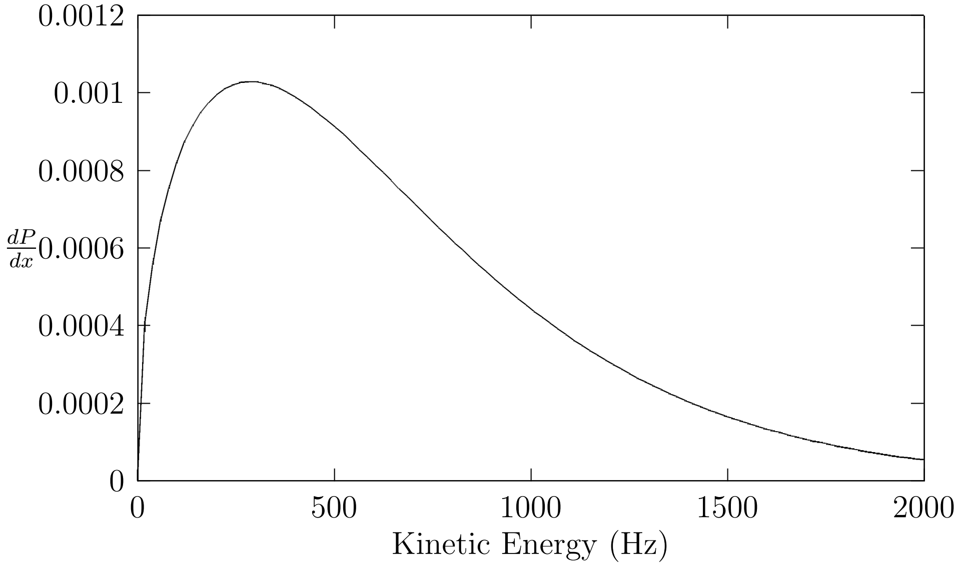

Figure 5.13: The boosted Maxwellian shape expected as the energy distribution for the isothermal halo model as observed from earth. This graph assumes an axion rest energy of 1 GHz.

This analysis assumes the median values for v_{sun}, v_{disp}, and ρ. The isothermal sphere predicts that the axion line shape is a boosted Maxwellian, as shown in figure 5.13. The easiest method to search for an isothermal sphere axion signal is by adjusting the resolution of the grand spectrum by square filtering until the sensitivity, measured in Signal to Noise Ratio (SNR), to an isothermal distribution is maximized.

This resolution was found analytically. A synthetic axion decay signal with a rest energy equivalent to 850 MHz was generated in an empty spectrum with an uncertainty equal to the average uncertainty of the grand spectrum. Square filters of varying width were performed on the signal and the resulting SNR for each was calculated. The width that maximized SNR was determined to be 998.846 Hz, which corresponds to a square filter on the 10.74 Hz resolution grand spectrum with a width of 93 values.

While this square-filtered grand spectrum is most sensitive to an isothermal sphere line-shape, it is equally sensitive to any axion line-shape whose integrated density within the 998.846 Hz wide filter is equal to the isothermal sphere's density. Also, the sensitivity of the fixed 998.846 Hz filtered spectrum varies slightly in sensitivity to the changing isothermal

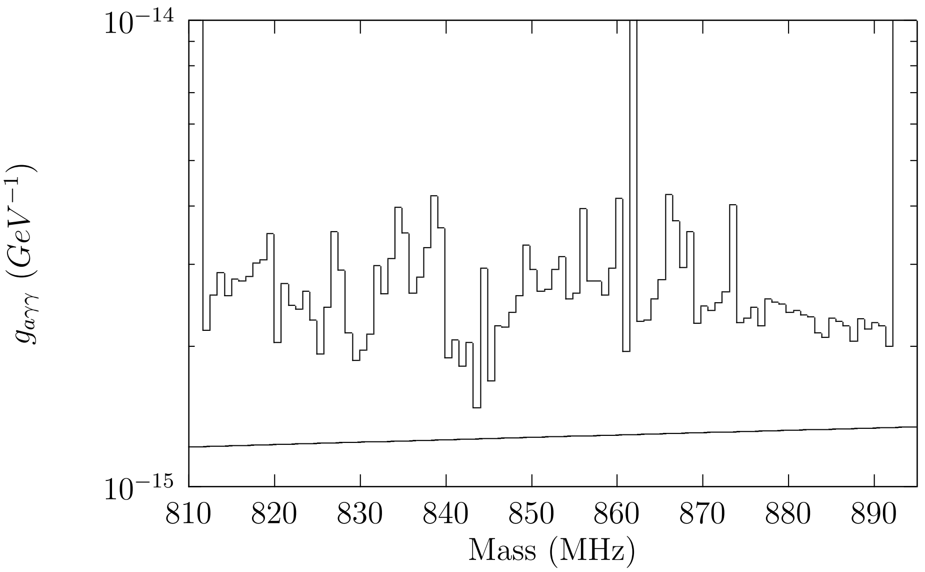

Figure 5.14: The 998.846 Hz wide square-filter based limit is sensitive to the isothermal sphere halo model with median parameters at 90% confidence. It is assumed that all of the power from a $.45 GeV/cc$ axion halo decays within the 998.846 filter width, which implies that the total halo density should be slightly larger for the isothermal halo model, which varies across the dataset. The diagonal line is the KSVZ coupling line. The "hole" at 862 MHz is discussed in appendix E

sphere line-shape over the 812 MHz to 982 MHz dataset. For these reasons and for simplicity, the limit is calculated on the assumption that the integrated density within a 998.846 filter-width is 0.45 GeV/cc. From this square-filtered grand spectrum, the exclusion limit on axion conversion power is calculated as described previously. From the resulting exclusion limit on expected axion-conversion power, a limit on the axion coupling strength, $g_{a\gamma\gamma}$ can be calculated. Since the expected axion-conversion power is proportional to $g_{a\gamma\gamma}^2$, the limit on axion coupling strength is produced by taking the square root of the expected axion-conversion power limit and multiplying by the KSVZ coupling strength. This limit shown in figure 5.14.

5.4.1 Optimal Filtering

The limit assuming an isothermal sphere can be improved by incorporating the specific line shape of the isothermal sphere model into a shaped filter instead of the simpler square filter used above. Perhaps the best line-shape based filter is a Weiner optimal filter. This implementation of the Weiner optimal filter uses a weighting defined as:

$$F(x) = \frac{S(x)^2}{S(x)^2 + N(x)^2} \tag{5.1}$$

where $S(x)$ is the expected signal power, described by the Maxwellian line shape and the axion rest energy, and $N(x)$ is the measured noise power. A Weiner optimal filter maximizes the SNR of a filtered spectrum having a known signal shape. It happens that the smooth and unstructured shape of the boosted Maxwellian line-shape is already well matched by the square filter, so the gains in SNR by using a Weiner optimal filter over the square filter are modest, 6-7% improvement as shown in figure 5.15. In practice an approximate Weiner filter is used to simply the analysis. The noise power, N(x), is set as the average of the noise power of the grand spectrum, resulting in a linear filter. This approximation is reasonable since the noise power is roughly constant throughout the dataset due to the scanning technique used to acquire data. The approximate Weiner filter is normalized so that the filter acting on the expected signal produces a value of one. In this way, the spectrum generated by applying the filter to the grand spectrum also has units of expected axion-conversion power. An exclusion limit is generated as before and is shown in figure 5.16. The average improvement in SNR for the Weiner filter over the square filter is 6.7%, in line with expectations and resulting in a 3.3% improvement in this exclusion limit on $g_{a\gamma\gamma}$.

5.5 Limits on Axion density

Besides mass, the expected axion decay signal in ADMX has two primary theoretical uncertainties: local axion density and axion coupling strength. The previous section assumed an axion density and placed limits on axion coupling strength. This section assumes the relatively optimistic, KSVZ axion coupling strength and places limits on the local axion density. Since the expected axion-conversion power assumed a 0.45 GeV/cc local axion density, mul-

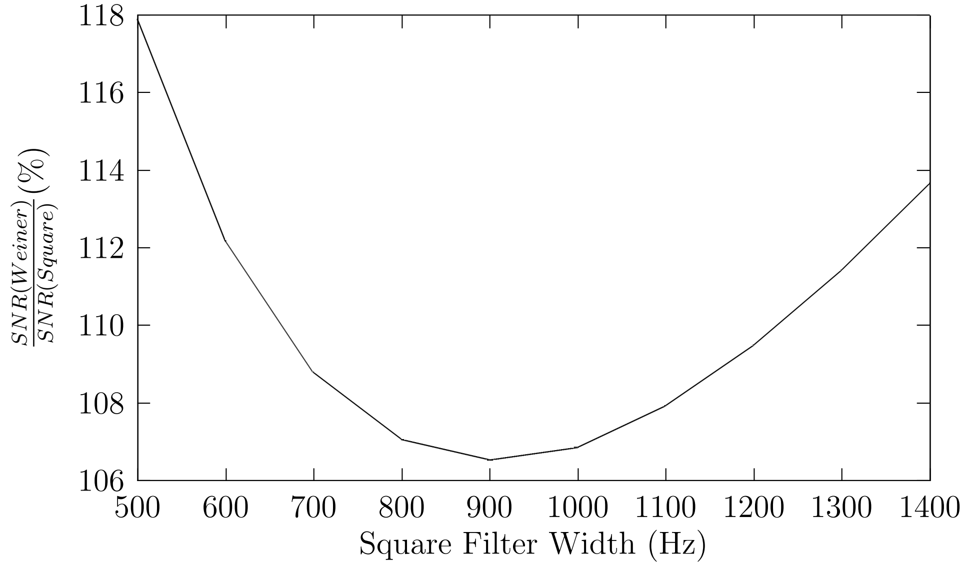

Figure 5.15: The percent ratio of Weiner filter SNR over box filter SNR as a function of the width of the box filter. The assumed axion rest energy is 850 MHz. This plot shows that for a square filter width of ~ 1 kHz, the improvement is expected to be around 6%.

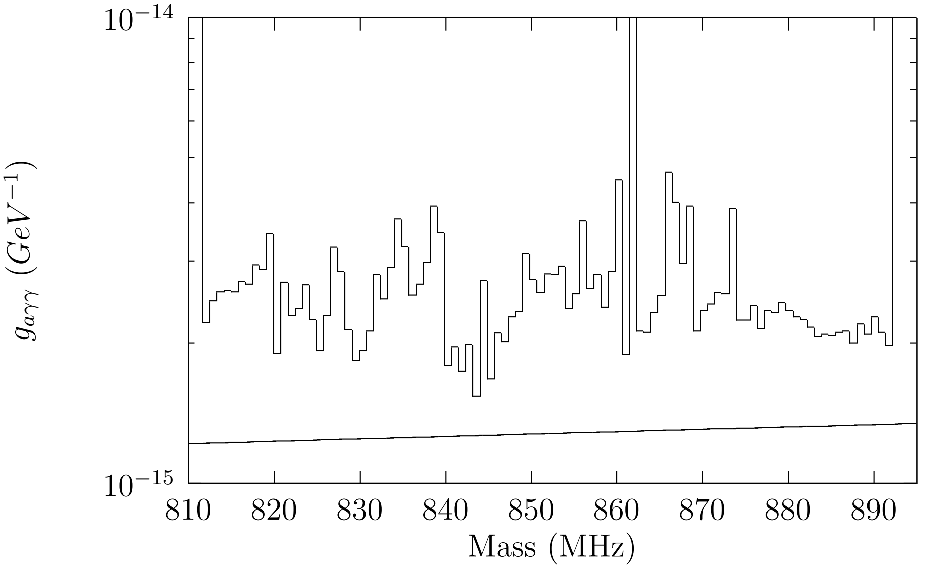

Figure 5.16: The limit on $g_{a\gamma\gamma}$ produced with an approximate Wiener filter on the isothermal halo model with mean parameters. The average improvement over the square-filter produced limit is 3.3%.

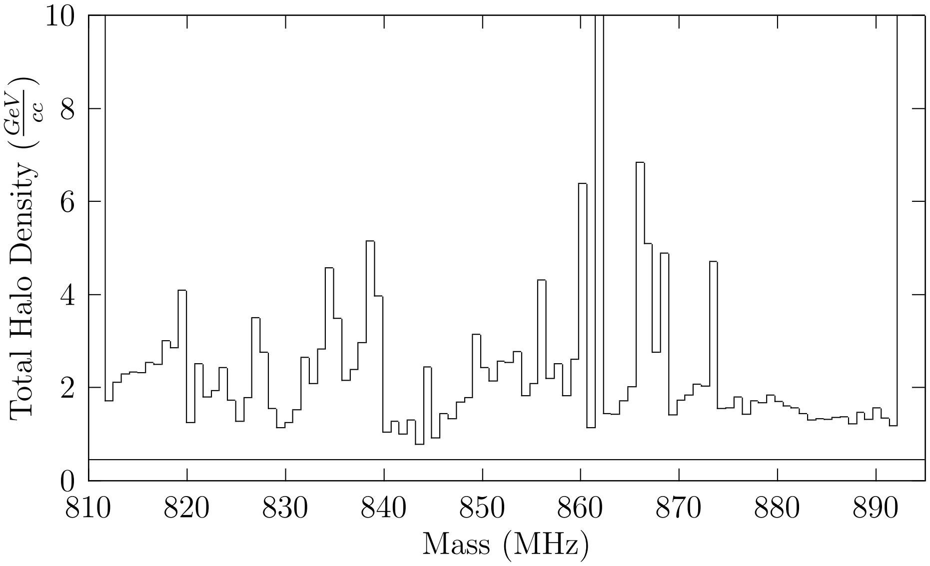

Figure 5.17: The limit on the local dark matter density, assuming the isothermal halo model and applying an approximate Weiner filter. The horizontal line is the expected 0.45 GeV/cc local density of our halo.

tiplying the limit of expected axion decay signal by 0.45 GeV/cc produces a limit on local axion density. Using the same benchmark halo model with both a square filter and Weiner filter produces the limits shown in figure 5.17.

5.5.1 Limit based on Dark Disk Model

As discussed in Chapter 3, the Milky Way's dark-matter halo is not well constrained. The Milky Way might posses a disk of dark matter or "dark disk", which would have been formed by a merger of the Milky Way with a dwarf galaxy. The local density of the Milky Way's dark disk could be as great as the local density of the rest of the dark-matter halo. Furthermore, the Milky Way's dark disk may have a much lower velocity dispersion than the halo. A dark disk with these properties that is co-rotating around the Milky Way with our sun would significantly improve ADMX's discovery potential. However, the possible parameter space of dark disks for the Milky Way is relatively unconstrained, preventing a search for a well motivated dark disk model. Instead, as an example of the potential gains for ADMX's sensitivity should such a model be presented, a co-rotating dark disk with a

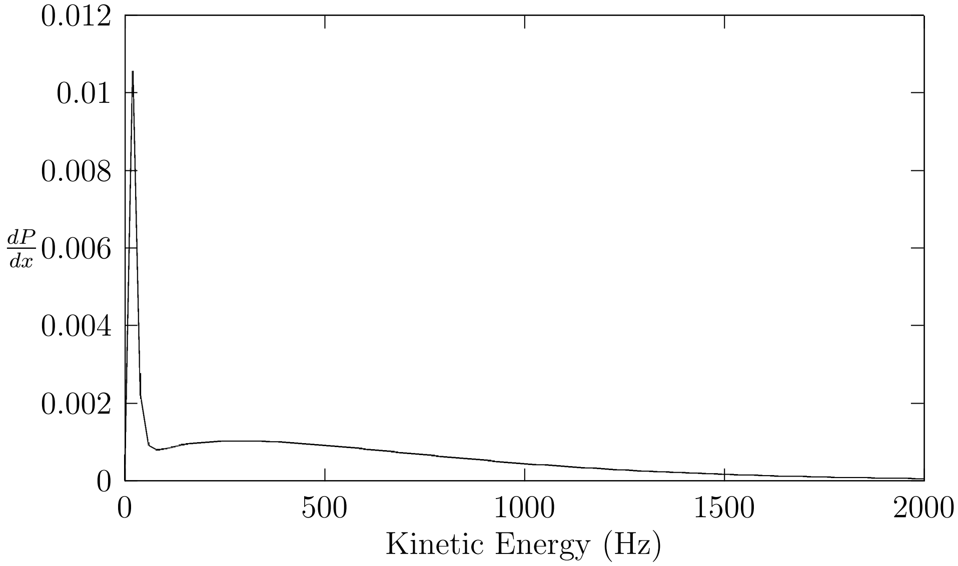

Figure 5.18: The expected signal shape in ADMX for an 850 MHz axion signal with the isothermal halo model augmented with a co-rotating dark disk with 33% of the total local density (50% of the halo's mass). The sharp peak near 0 Hz is the dark disk signal.

velocity dispersion of 50 km/s and a density of .15 GeV/cc is assumed. The resulting shape for a signal in ADMX is shown in figure 5.18. After applying the same approximate Weiner filter techniques described previously, the resulting 90% confidence limit for this search is shown in figure 5.19.

5.5.2 Limits on Cold Flow Models

As discussed in Chapter 3, the dark matter that remained unassociated with any halo remains dense in velocity-position phase-space and is therefore extremely cold. There are expected to be discrete "cold flows" of dark matter as it falls into and out of the Milky Way's gravitational potential. At the point of closest approach to the galactic center, these flows form overdensities or caustics. If the Earth happens to be located near one of these caustics, then ADMX would have significantly enhanced discovery potential. However, implementing a search for these narrow signals presents several difficulties.

The finite integration times (30 minutes typically) of ADMX mean that the relative motion of ADMX to a galactic flows changes over this time. Since ADMX has very high

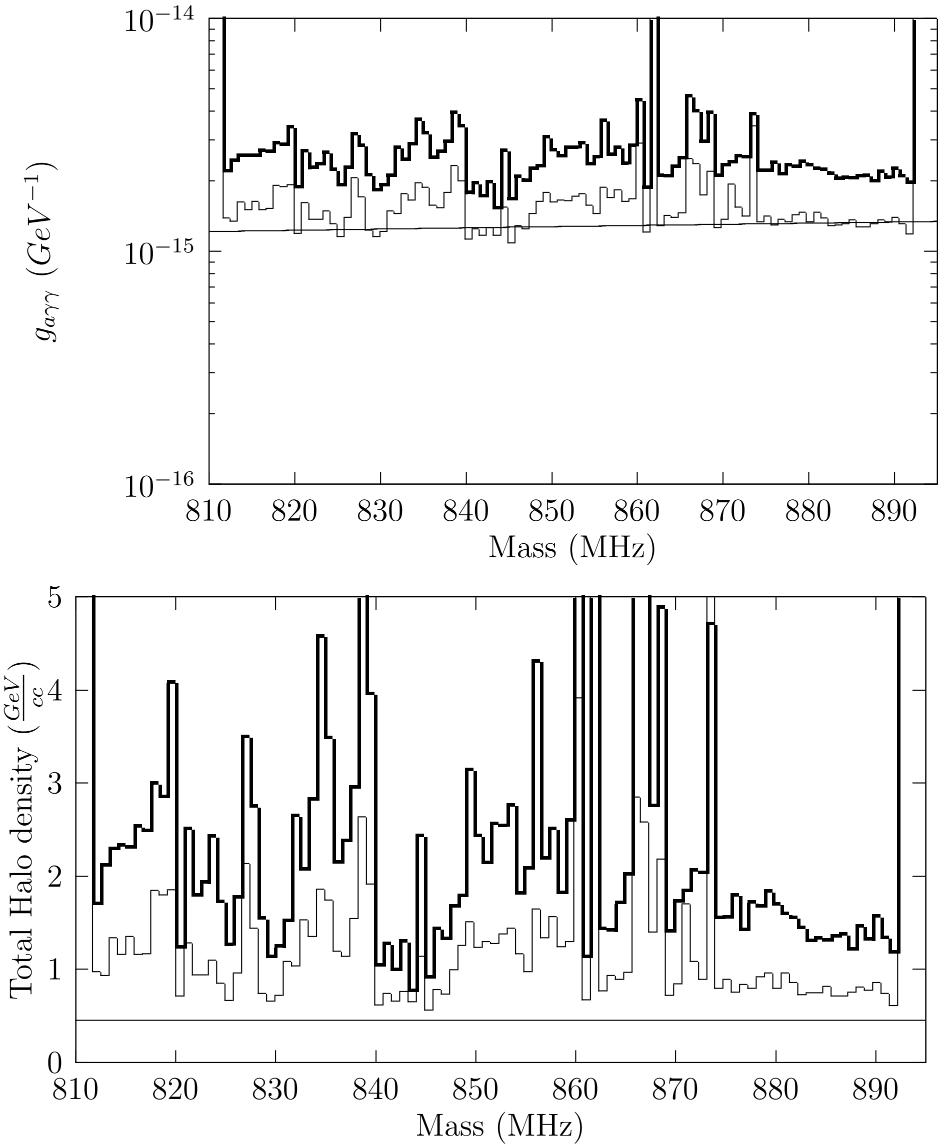

Figure 5.19: The improved limit (lighter shaded) by assuming a dark disk model. The bolded limits and plot details are the same as from the isothermal model limits shown in figures 5.16 for $g_{a\gamma\gamma}$ and 5.17 for halo density.

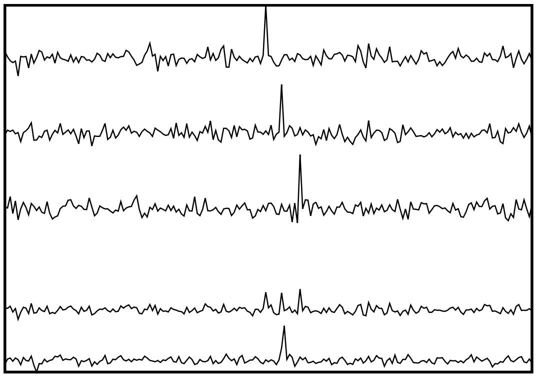

Figure 5.20: A sketch illustrating how proper accounting of relative velocity changes is important for narrow searches. The top three spectra correspond to single integrations while the bottom two are two different sums of the top three. The first summed spectrum simply adds bins together of the same frequency, smearing the signal into multiple, less significant signals. The bottom summed spectrum shifts the individual spectra to add the peaks together,thereby increasing the SNR of the peak in the summed spectrum.

frequency resolution, 1 part in 10^{10}, small changes in relative velocity between a flow and ADMX change the frequency location of the resulting signal within the dataset. This dataset was recorded at Livermore, CA, with a location of 37.683710 North, 121.704585 West on the Earth's surface. The Earth's surface rotates at a speed of cos(latitude)×0.465 km/s with a period of one sidereal day. The Earth orbits the sun at an average speed of 29.78 km/s, with a minimum of 29.29 km/s and a maximum of 30.29 km/s, due to the eccentricity of the orbit. For a cold flow with a velocity of 500 km/s[7] with an axion rest energy of 850 MHz, the worst case shift in frequency is 4.4 Hz for the rotational motion (over half a day) and 280 Hz for the orbital motion (over half a year). While the orbital shift is much larger, the worst case rate of shift is worse for the rotational motion: 0.16 mHz/s vs 0.03 mHz/s.

At the native 0.042 Hz resolution of the dataset, with the typical 30 minutes of integration time, a cold flow would deposit energy over different frequency bins of a full resolution grand spectrum, as illustrated in figure 5.20. If the search for these flows preceded as in the isothermal or dark disk sections, then ADMX's long integration time would diminish the

---

[7] The galaxy's escape velocity from the Earth's position is 550 ± 50 km/s. The expected velocity of a cold flow should at or below the galactic escape velocity.

Name	Value (km/s)	Error (km/s)
$V_{\text{solar peculiar}}x$	10.62	0.49
$V_{\text{solar peculiar}}y$	16.06	1.14
$V_{\text{solar peculiar}}z$	8.60	1.02
V_{LSR}	220	20
V_{escape}	544	33

Table 5.4: The velocities and uncertainties used in cold flow calculations. All are in galactic frame with the y axis pointing towards the galactic center, the z axis pointing perpendicular to the galactic plane, and the x axis pointed towards the direction of the Local Standard or Rest's (LSR) motion. Peculiar velocities are from [66], LSR is from [67], and escape velocity is from [68].

sensitivity of a cold flow search. There are two obvious search strategies: choose the finest resolution that is still insensitive to the changing flow energies or exploit the specific flow velocities in a cold flow model. The second approach is, in principle, more sensitive. The former approach was pursued in a previous ADMX publication [65]. This work pursues the latter.

As discussed in chapter 3, there are different models of cold flows that predict different directions and velocities of cold flows. These models predict specific flow velocities and directions in the galactic rest frame. In order to calculate the local, total energy of a flow as a function of time, the flow's coordinates are converted from galactic coordinates to Earth's equatorial coordinates. While the Earth's motion around the Sun is well known, the Sun's motion through the galaxy has large errors, as shown in table 5.4. The sun has a "peculiar" motion against the local group of stars within the galaxy, called the Local Standard of Rest, LSR. The LSR orbits the galactic center. The large uncertainties in these values result in a flow energy with a significant uncertainty in total energy.

Having the total flow energy as a function of time, the individual spectra of the excess-axion-power dataset can now be added without the energy of the flow being spread across a large number of points. This generates a model-specific grand spectrum. From this grand spectrum, limits on local axion density and axion coupling strength are generated as before. However, the large uncertainties from the specific flow model and solar motion need to be accounted for. Accounting for frequency uncertainties from a variety of values is much more difficult than the simple power uncertainties used to generate the previous limits.

To account for frequency uncertainties, the limit produced above is adjusted by calibrating the effects of the frequency uncertainties. To do this, for each 1 MHz wide section of the data, 100 large test signals are injected into the processed spectra before they are shifted and combined into a grand spectrum. Each injected signal has velocity values sampled from the large space of uncertainties, which are assumed to be Gaussian. The attenuation of these signals in the new grand spectrum is measured and the original limit is scaled accordingly to produce a frequency-error calibrated limit. As a sanity check, the process of generating a grand spectrum is repeated, but with signals injected at the new, calibrated limit. If at least 90% of injected signals are discovered above the calibrated limit, then the calibrated limit is accepted as the 90% confident limit for that 1 MHz wide section.[8].

There are several models of cold flows for our galaxy. Figure 5.21 shows the two particular flow models this work investigates. The first model this work investigates assumes that the extended halo is non-rotating, so a late infall flow at the Earth's location in the galactic rest frame would come from opposite the galactic center at the local escape velocity.[9] The algorithm described previously applied to this model generates limits shown in figure 5.22. The late infall model described in [8] argues that the late infall flows all have a uniform angular momentum and energy, forming caustics. This work investigates the case where a caustic lies near the earth's location, since it represents the highest discovery potential. The limit assuming a caustic flow labeled "n=5" from [8] is presented in figure 5.23.

Of course, these two models may not be realized in nature. Furthermore, the model dependence and astronomical uncertainties limit the sensitivity of these searches. If instead, ADMX performed a full-sky survey by choosing representative velocities and directions in

---

[8] Note that unlike the limits in the previous sections, which records the worst limit over all frequencies, this limit is a hybrid between the worst limit and the average limit.

[9] Of course there would be another flow falling out of the galaxy, but the total energy of the outgoing flow will be slightly lower than the ingoing due to the accretion of mass in the galactic halo. Also, since the outgoing flow passed through the galactic center, it is expected to be more disturbed, so the inward flow is more appealing to search for.

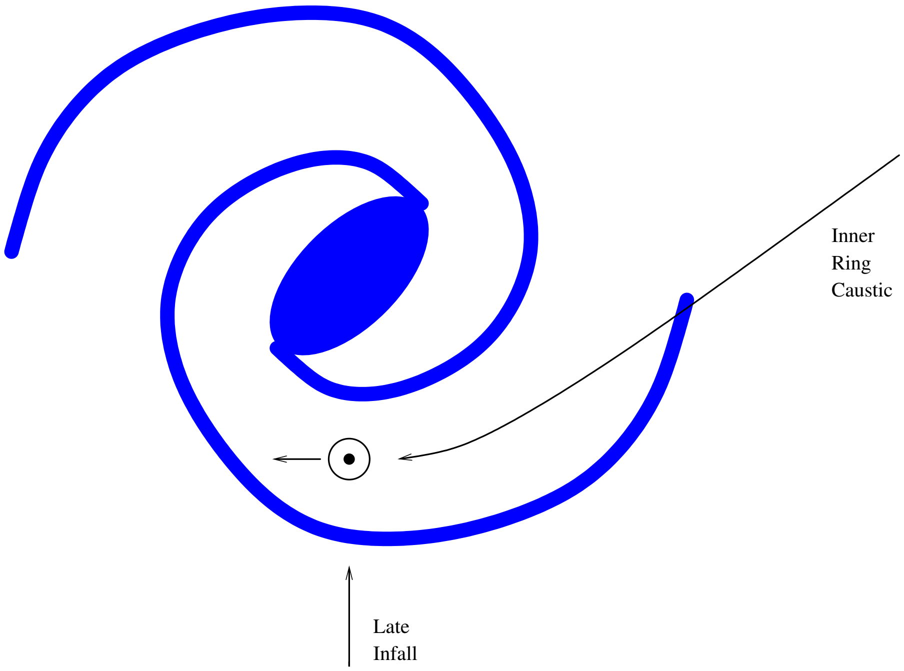

Figure 5.21: The orientation of possible cold flows at the earth's location of the galaxy. The "Late Infall" flow assumes that the dark matter falling into the galaxy for the first time has no net angular momentum; therefore, it falls directly toward galactic center. The "Inner Ring Caustic" flow assumes that the dark matter around the galaxy received a uniform torquing, forming rings of high local density at the inner turnaround of late infall dark matter.

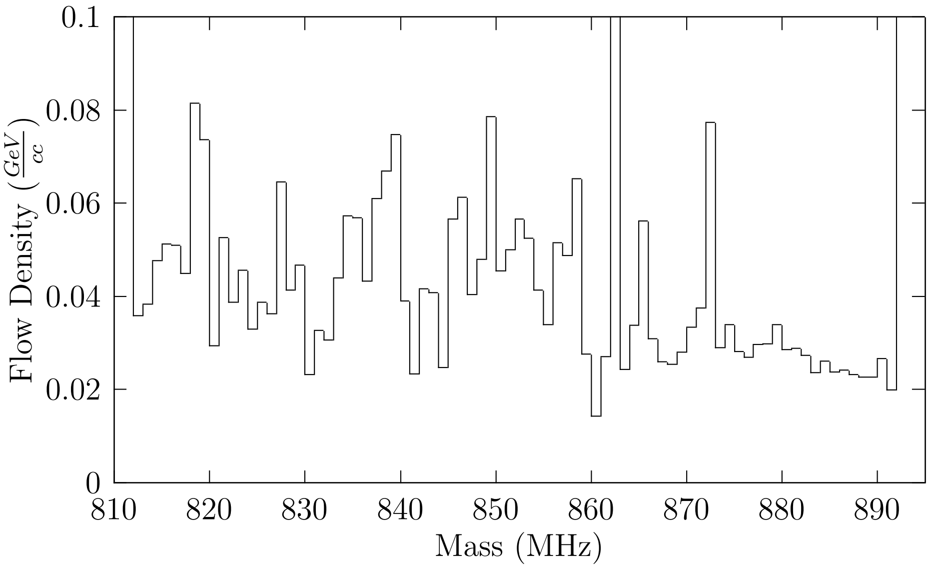

Figure 5.22: Non-rotating late infall limit. In this model, the cold dark matter falling into our galactic halo for the first time has been minimally disturbed, so it falls almost directly towards the galactic center. The flow is assumed to originate from a 20 degree cone opposite the galactic center.

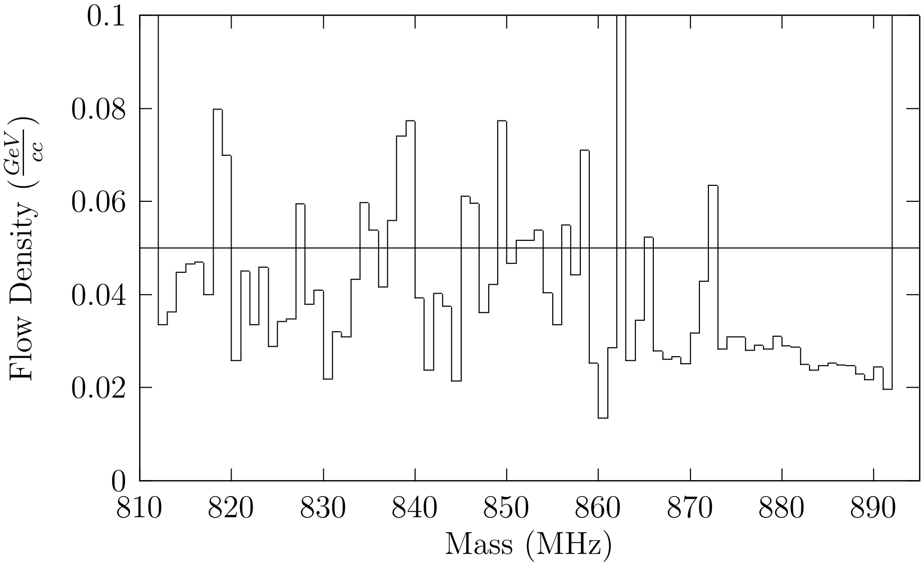

Figure 5.23: The “n=5” Sikivie Ring-Caustic limit. The horizontal line corresponds with the density predicted in reference [8]. In this model, the cold dark axions falling into our galactic halo have a uniform angular momentum and form a ring caustics of large density near the earth.

the analysis for late infall axion flows, the uncertainties in frequency become small. Unfortunately, such a search would increase processing demands by around a factor of 1000. For the 80 MHz wide dataset in this analysis, searching for a single flow from a point in the sky takes a day on a single computer, so performing a full-sky search would either require a cluster of computers or a significant algorithmic improvement[10]. As a demonstration of the technique, a single-flow search looked for a late infall flow from a single point in the sky, almost opposite galactic center((150,0) in (l,b) galactic coordinates) at 700 km/s. The resulting limit of this search is shown in figure 5.24. By eliminating the uncertainties of model-dependent late infall searches, this single-flow search improves sensitivity by roughly 2x. Of course doing 1000 searches also has pitfalls due to the trials factor, but since there are already $\sim 10^{10}$ search points, increasing that to 10^{13} only increases the maximum expected value by 15%, small compared to the 100% improvement in sensitivity.

---

[10] Most of the analysis time is spent loading datasets to and from the disk. By rewriting the analysis to perform all searches without extra disk loads, the analysis times may be reasonable. Furthermore, the vector additions required in this search may be an optimal workload for a GPU, which may improve performance by 10x.

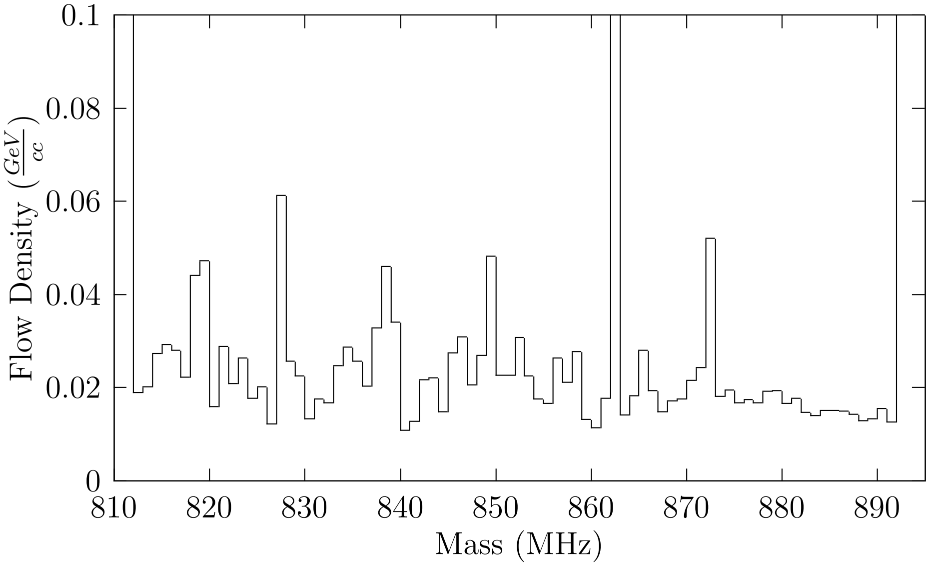

Figure 5.24: A search for a flow from one direction and velocity in the sky. This flow happens to be from (150,0) in (l,b) galactic coordinates with a velocity of 700 $\frac{km}{s}$.

Chapter 6

Discussion and Conclusions

As detailed in chapter 2, the axion is a well motivated extension of the Standard Model of particle physics and has remained so for 30 years. The Standard Model is fine-tuned in the amount of Charge-Parity symmetry violation in the Strong interaction. The associated parameter, $\overline{\theta}$, is expected to be of order one but is measured to be less than 10^{-12}. An elegant solution to this issue is the introduction of a broken symmetry, which dynamically forces $\overline{\theta}$ to zero during the early universe. Chapter 3 described how a very light, $\sim 10\,\mu\text{eV}$, axion would be produced in great abundance during the Big Bang. The resulting non-relativistic, long lived, and nearly invisible axions are ideal dark matter. As such, discovering the axion would solve a longstanding issue in particle physics as well as one of the most important questions in cosmology: What is the nature of dark matter? An important feature of axion dark matter is the relatively narrow constrains on mass and coupling strength to photons. The axion has a mass from 1 μeV to 10 meV and has a coupling strength that varies over models by a factor of roughly 3. These constraints allow for the possibility of a definitive search, either detecting the axion or eliminating it[1]. Chapter 4 described ADMX, the most sensitive experiment performing this search.

---

[1] The axion may be arbitrarily light under anthropic arguments. However, the axion is the solution to a fine tuning problem while an arbitrarily light axion is finely tuned.

6.0.3 Operating ADMX

From 1995 to 2005, the transistor-based ADMX ruled out KSVZ-coupled axions with a local density of .45 GeV/cc in a signal bandwidth of 750 Hz over an axion mass range of 1.9 μeV to 3.3 μeV. This was a significant achievement, excluding plausible dark-matter axions over almost an octave in mass. However searching over the range of axion models requires an experiment that is either 10x more sensitive, runs 100x longer, or has 100x the budget to perform parallel searches. Only the first option seems reasonable, and it can be realized with two improvements: a quantum-noise limited, broadband amplifier and a 100 mK operating temperature. While a 100 mK operating temperature for an ADMX scale experiment has been achievable for decades, quantum-noise limited, broadband amplifiers have only recently been realized in the stripline-resonator SQUID amplifier described in chapter 4. Demonstrating this new amplifier technology in an axion search was the major goal of ADMX. However, the large and strong magnetic fields in ADMX are incompatible with SQUID amplifiers. To eliminate this incompatibility, the bucking magnet system creates a near-zero field volume in the heart of ADMX. In 2008, ADMX successfully searched for axions with a SQUID amplifier.

Operating ADMX with a SQUID amplifier proved to be more challenging then initially expected. The solid-state HEMT amplifiers that the SQUID replaced were plug and play devices, with no maintenance requirements. In contrast, the SQUID was found to require daily to weekly bias adjustments. Furthermore, ADMX had multiple SQUID failures, which required long-lead-time replacement SQUIDs. The inability to obtain a replacement SQUID caused months of down-time, leading to a short 2010 run without a SQUID in order to complete the search range of the cavity system. The availability of commercial SQUID manufactures, such as Hypres and ez SQUID, alleviate SQUID sourcing problems for future ADMX operations.

With the SQUID upgrade, ADMX also changed cavities to extend its frequency reach and explore new axion masses. The new cavity has the same height, tuning rods, and field probes

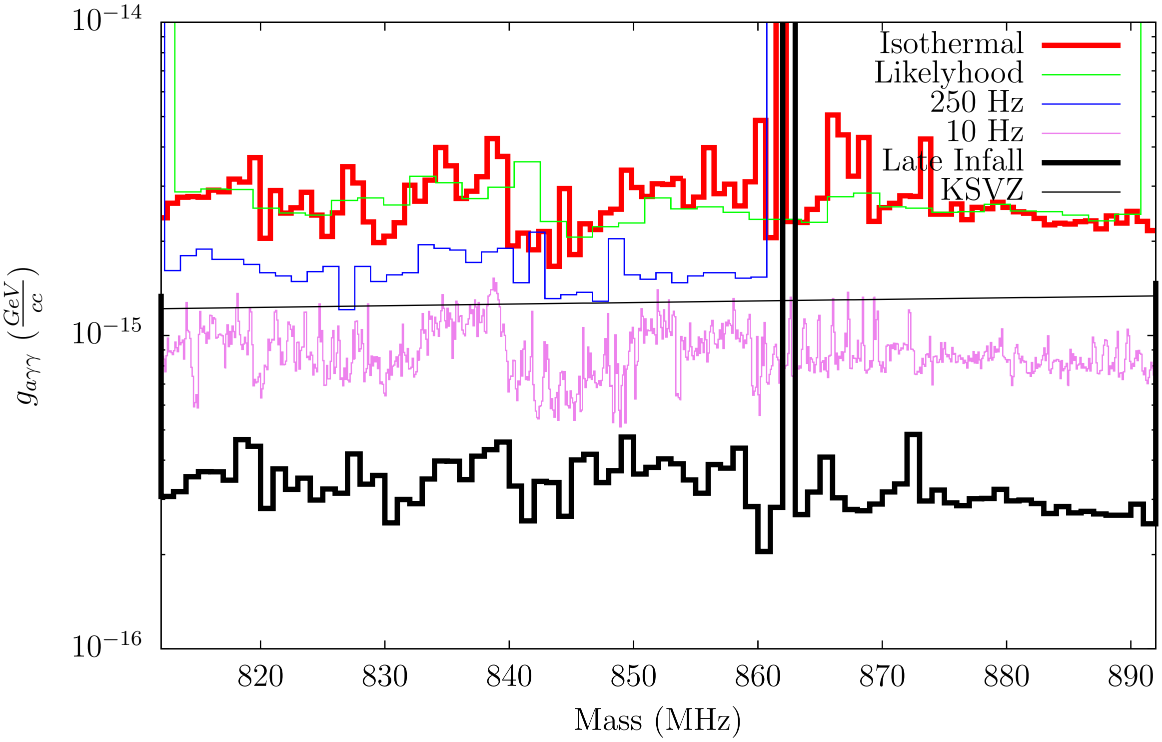

Figure 6.1: The combined limits on the axion-to-photon coupling at varying resolutions. All limits assume 0.45 $\frac{GeV}{cc}$ of local axion density. All but the maximum likelihood and Weiner filter limits should only be sensitive to a fraction of the local axion density, so their enhanced sensitivity is partially an artifact.

as the old cavity, but has a reduced radius. The smaller cavity allowed for tuning the TM_{010} mode up to 892 MHz, compared to 812 MHz for the previous cavity. From 2008 to 2010, ADMX searched within the frequency range of 812 MHz to 892 MHz corresponding to axions with masses between 3.3 μeV and 3.69 μeV. Figures 6.1 and 6.2 show the various limits on axion-to-photon coupling and axion-density limits for this search range. The large variation in sensitivity comes from assuming different axion line-shapes, motivated by different models of the Milky Way's dark-matter halo.

6.0.4 Investigating Halo Models

There are many models of the Milky Way's dark-matter halo. The baseline model typically assumed in dark-matter searches is the isothermal sphere model. As discussed in chapter

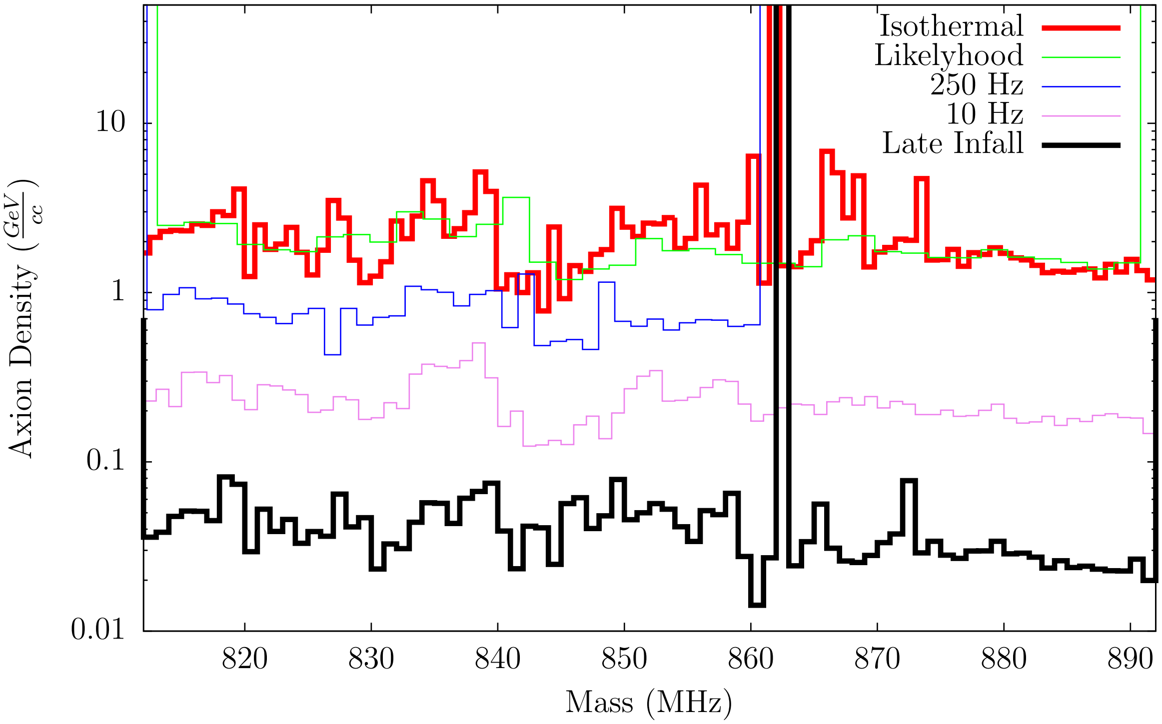

Figure 6.2: The combined limits on halo density at varying resolutions. All limits assume KSVZ coupling. The Weiner filter limit is approximately equivalent to a 1000 Hz wide box filter. The 250 Hz limit is the nonvirialized limit from our 2010 publication. The 10 Hz limit is from our 2011 publication. The .08 Hz limit is the late infall limit from this work. While it appears that smaller bandwidths are more sensitive, narrower bandwidths are expected to capture less of the halo.

3, the local energy distribution of dark matter in the isothermal sphere model is in good agreement with n-body dark-matter simulations. As such, the isothermal sphere model with parameters from the International Astronomical Union is the baseline model for ADMX searches. Past ADMX searches simply choose a bandwidth of 750 Hz to capture much of the expected line-shape from the isothermal sphere model. This work demonstrated that incorporating the shape of the isothermal sphere line instead of just its bandwidth can improve ADMX's sensitivity by roughly 7%.

Due to a warmer than expected operating temperature, the 812 MHz to 892 MHz search assuming the isothermal sphere model does not exclude KSVZ coupled axions at 0.45 GeV/cc density. Since ADMX's sensitivity scales as $1/\sqrt{\text{Bandwidth}}$, this thesis explored halo models with expected signals that are narrower in bandwidth than the isothermal sphere model. One such model is the dark-disk model, where the disk of the Milky Way contains a dark matter component. Dark disk models are primarily motivated from the results of n-body simulations with baryons, where merging subhalos are drawn into the dense disk of stars and gas in spiral galaxies. There are a wide range of possible configurations for such a dark disk in our Milky Way, so this thesis choose a disk model which maximized ADMX's sensitivity, where the disk has velocity dispersion of 50 km/s, is co-rotating with the sun, and is 50% as dense locally as the isothermal sphere's density. A search with this model excludes KSVZ coupled axions in the 812 MHz to 892 MHz search range. However, there is no physical motivation for the chosen disk model out of the range of possible models. Furthermore, observations disfavor the possibility for the Milky Way to have a significant dark disk. [52]

Another set of halo models that could improve ADMX's sensitivity are cold flow models. Undisturbed, primordial dark matter has extremely small velocity dispersion. As this dark matter falls into the Milky Way for the first time, it forms a cold flow that would appear in ADMX has a narrow line, with a bandwidth limited by the receiver electronics and the motion of the earth. If the velocity of the flow is given by the model, then the motion of the earth can be eliminated as a lower limit to signal bandwidth, leaving only receiver resolution.

This work investigated two such models: a flow falling directly towards galactic center and the most dense flow from the inner-ring caustic model from [8]. The latter model's predicted density of 52 MeV/cc allows for the exclusion of KSVZ model axions in much of the search range.

As discussed in chapter 3, n-body simulations predict a more chaotic picture than the simple flow models applied in this thesis. The direction of cold flows at the Earth's postion seem to be largely random. Futhermore, the largest flow at the sun's position is expected to have a density closer to 5 MeV/cc than 50 MeV/cc [49]. For a search for such light flows to be competitive with the isothermal sphere search, the spectral resolution would need to be roughly 1 mHz. There are a miriad of problems associated with such a fine resolution search. First, the search requires an expensive time standard with 1 part in 10^{12} stability. Second, the signal may drift as much as 200 Hz during the required 1000 second integration time. This drift requires 200 independant FFT's be performed for every 1000 second integration, drastically increasing computing resources. Finally, since the direction of the flow is unknown, the search would need thousands of search channels, requiring vast amounts of disk space and lowering the sensitivity from the large trials factor.

In summation of this thesis's findings, ADMX sees a modest, $\sim 7\%$, gain in performance by incorporating the isothermal sphere halo model's shape within the search algorithm. Further gains can be made by adding a dark-disk component of to the dark-matter halo, but such assumptions are likely to be wrong due to the wide parameter space available for a dark disk, including non-existant. If any evidence were found for a specific dark disk configuration in our Milky Way, then ADMX may see up to double performance over the basic isothermal sphere halo search. The only other search with similar gains in performance over the isothermal sphere search is the inner-ring caustic search. However, like the dark-disk model, there is no substantial observational evidence supporting the inner-ring caustic model. As such, while a inner-ring caustic search has enhanced discovery potential over the isothermal sphere search, the exclusion limits produced by the inner-ring caustic search speak

Parameter	1995-2005	2008-2010	2014 Upgrade
Cavity Volume	220 l	140 l	140 l
Cavity Q	100,000	30,000	100,000
Cavity Temperature	1.2 K	2.0 K	100 mK
Amplifier Noise	3.0 K	1.0 K (4.0 K with HFET)	50 mK
B Field	7.8 T	6.0 T	7.8 T
Relative Power Sensitivity	1.0	.16	18
Relative Scan Rate	1.0	.083	324

Table 6.1: A comparison of performance-sensitive parameters of ADMX. While the SQUID upgrade for 2008 to 2010 running improved performance, the smaller, lower quality cavity and lower magnetic field strength degraded performance compared to the 1995 to 2005 experiment. The experiment is currently being upgraded to run much colder, which will improve performance substantially.

more towards that specific halo model than the existance of a particular mass of dark-matter axions.

6.0.5 ADMX's Future

ADMX is currently being upgraded with a helium-3 dilution refrigerator. The redesigned experimental insert should achieve an operating temperature of 100 mK at max. Table 6.1 shows the expected performance parameters of this new experiment. The upgraded ADMX, when complete in 2014, will be sensitive to weaker DFSZ-model axions while scanning possible axion masses roughly four times faster than the original 1995 experiment. The upgraded sensitivity should allow for the rapid search for 2 μeV to 4 μeV axions. Furthermore, the upgraded ADMX will simultaneously capture the TM_{020} mode, searching in the 4 μeV to 8 μeV mass range with slightly reduced sensitivity. Figure 6.3 shows the planned search region for the upgraded experiment. The planned search will fully scrutinize 2 octives of axion mass out of the roughly 10 octives available. If the axion exists and all masses are equally likely, then this search has a 20% chance of success.

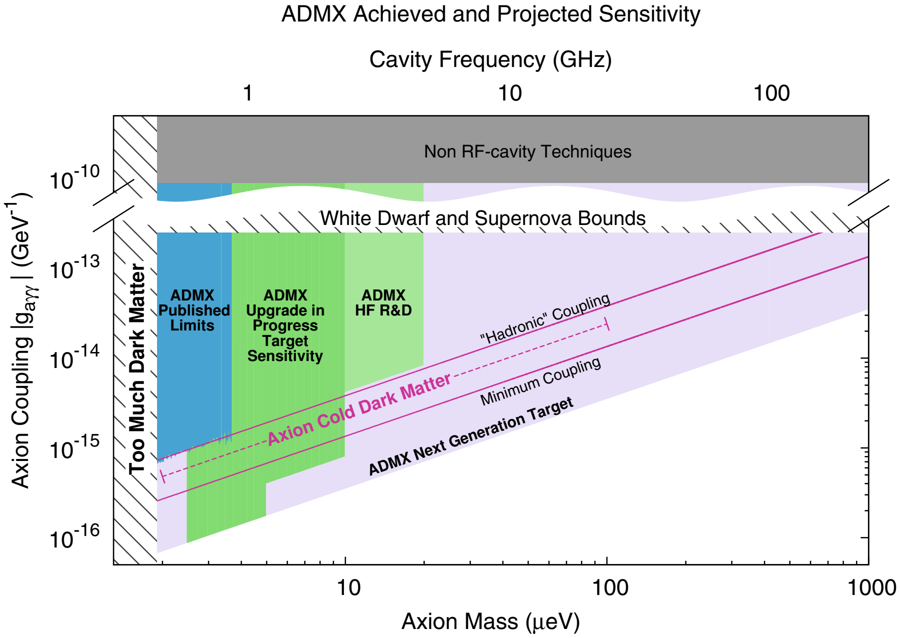

Figure 6.3: ADMX's planned search after the ongoing dilution refrigerator upgrade. The low noise of the next generation experiment allows for the detection of the weaker coupled DFSZ axion model. The inclusion of another receiver chain allows for a simultaneous search using the less sensitive TM_{020} mode, which doubles the search window. If the axion exists, this search will have roughly a 20% chance of finding it.

Appendix A

Power Developed in Sikivie Haloscope

The Lagrange density for the axion is:

$$\mathcal{L} = \frac{1}{2}\partial_\mu a \partial^\mu a - \frac{1}{2}m_a^2 a^2 - G_{A\gamma\gamma}\mathbf{E}\cdot\mathbf{B}a \tag{A.1}$$

where a is the axion field, m_a is the axion mass, $G_{A\gamma\gamma}$ is the axion to photon coupling strength, $\mathbf{E}$ is the electric field, and $\mathbf{B}$ is the magnetic field. Since an invisible axion's de Broglie wavelength is kilometers long, the axion field is approximately spatially uniform. Neglecting the small interaction term, the resulting axion field's equation of motion is simply:

$$a(t) = Ae^{im_a t} \tag{A.2}$$

for some constant coefficient A. The last term of equation A.1 scatters axions into photons. In a cavity, the $\mathbf{B}$ field is an axial external field while $\mathbf{E}$ is the cavity mode's oscillating electric field. The power deposited into a cavity with volume V from axion-to-photon conversion (at steady state) is:

$$P_{ax} = \int_V dV \left(\frac{\partial}{\partial t}\left(a(t)G_{A\gamma\gamma}\mathbf{E}\cdot\mathbf{B}\right)\right) = 2\omega_0 a(t) G_{A\gamma\gamma}\int_V dV\mathbf{E}\cdot\mathbf{B} \tag{A.3}$$

where ω_0 is the cavity mode's frequency and $m_a = \omega_0$. In a perfect resonator, this power would equalize the photon and axion fields, turning dark-matter axions into a tremendous power source. However, the cavity dissipates energy into the cavity walls, P_{dis}, so the axion decay power is quite limited. The steady state solution is when the power dissipated into the walls equals the axion conversion power. The power dissipated by the cavity is parameterized by the cavity's quality factor, Q, defined by:

$$Q = \omega_0 \frac{U}{P_{dis}} \tag{A.4}$$

where U is the stored energy in a cavity mode. The stored energy in the cavity mode is:

$$U = \int_V dV \left(\frac{\epsilon}{2} \mathbf{E}^2 + \frac{1}{2\mu} \mathbf{B}_{cav}^2 \right) \tag{A.5}$$

where $\mathbf{B}_{cav}$ is the cavity mode's magnetic component. Solving for P_{dis} yields:

$$P_{dis} = \frac{\omega_0}{Q} \int_V dV \left(\frac{\epsilon}{2} \mathbf{E}^2 + \frac{1}{2\mu} \mathbf{B}_{cav}^2 \right) \tag{A.6}$$

It is useful to introduce the field strength factor $E_{max} = \frac{\mathbf{E}}{\mathbf{E}_{mode}} = \frac{\mathbf{B}_{cav}}{\mathbf{B}_{mode}}$, where $\mathbf{E}_{mode}$ and $\mathbf{B}_{mode}$ are the normalized cavity modes. In the steady-state, time-averaged solution, the cavity energy is constant, so the powers are equal: $P_{dis} = P_{ax}$. Solving this equation for E_{max} yields:

$$E_{max} = 2QG_{A\gamma\gamma}a(t) \frac{\int_V dV \mathbf{E}_{mode} \cdot \mathbf{B}}{\int_V dV \left(\frac{\epsilon}{2} \mathbf{E}_{mode}^2 + \frac{1}{2\mu} \mathbf{B}_{mode}^2 \right)} \tag{A.7}$$

Substituting E_{max} into P_{ax} and gives the axion decay power:

$$P = 4Q\omega_0 (G_{A\gamma\gamma}a(t))^2 \frac{(\int_V dV \mathbf{E}_{mode} \cdot \mathbf{B})^2}{\int_V dV \left(\frac{\epsilon}{2} \mathbf{E}_{mode}^2 + \frac{1}{2\mu} \mathbf{B}_{mode}^2 \right)} \tag{A.8}$$

The integral expression is captured in a new parameter, f_{nlm}, called the form factor, defined as:

$$f_{nlm} \equiv \frac{\left(\int_V dV \mathbf{E}_{mode} \cdot \mathbf{B}\right)^2}{VB^2 \int_v dV \frac{\epsilon_r}{2} \mathbf{E}^2_{mode} + \frac{1}{2\mu\epsilon_0} \mathbf{B}^2_{mode}} \tag{A.9}$$

where $\epsilon_r = \epsilon(\mathbf{x})/\epsilon_0$. Substituting in for f_{nlm} and converting to MKS units, equation A.8 becomes:

$$P = 3.04 \times 10^{-42} c^2 \epsilon_0 B^2 V f_{nlm} \nu_a Q g_\gamma^2 \frac{d_a}{.3 \frac{GeV}{cc}} \tag{A.10}$$

where B is the axial field in Teslas, V is the volume in m^3, f_{nlm} is the mode dependent form factor of the cavity, ν_a is the axion's mass in Hz, Q is the quality factor of the cavity, g_γ is the model dependent coupling of .97 for KSVZ and .36 for DFSZ, and d_a is the local axion density in GeV/cc. For a meter scale laboratory experiment, this power is roughly 10^{-22} Watts.

Appendix B

Quality Factor Issue

Throughout most of the data run, sensitivity suffered from very poor quality factor, or Q. The previous ADMX cavity achieved loaded Q of around 100,000. Figure B.1 shows the Q throughout the data run. It is apparent from the graph that the Q was degrading over time. During commissioning in 2008, the Q was typically around 40,000. However, by the end of 2009, the Q was around 10,000. Scan rate scales as $\sqrt{Q}$, so operations were slowed by as much as 3x compared to expected. Since the demonstration of the operation of a SQUID amplifier in ADMX was the primary goal of 2008 to 2010 running, the poor Q was not investigated until the long downtime from September 2009 to February 2010.

Between the 2009 and 2010 runs, the cavity was opened to see if the problem was visible. Figures B.2 and B.3 show the obvious issues. The copper plating was separating from the stainless. Copper does not typically bond with the stainless steel. Standard practice for metal plating is to first plate a thin layer of Nickel, called a Nickel strike, which both copper and stainless bond with. Due to the high magnetic field environment of the cavity, the LLNL plating shop did not perform a Nickel strike. This was likely the cause of the separation.

The lossy knife edge was repaired by the liberal application of indium wire. Indium is soft and a reasonably good conductor at cryogenic temperatures. Running during 2010 showed a marked improvement in Q, typically ranging from 60,000 to 80,000.

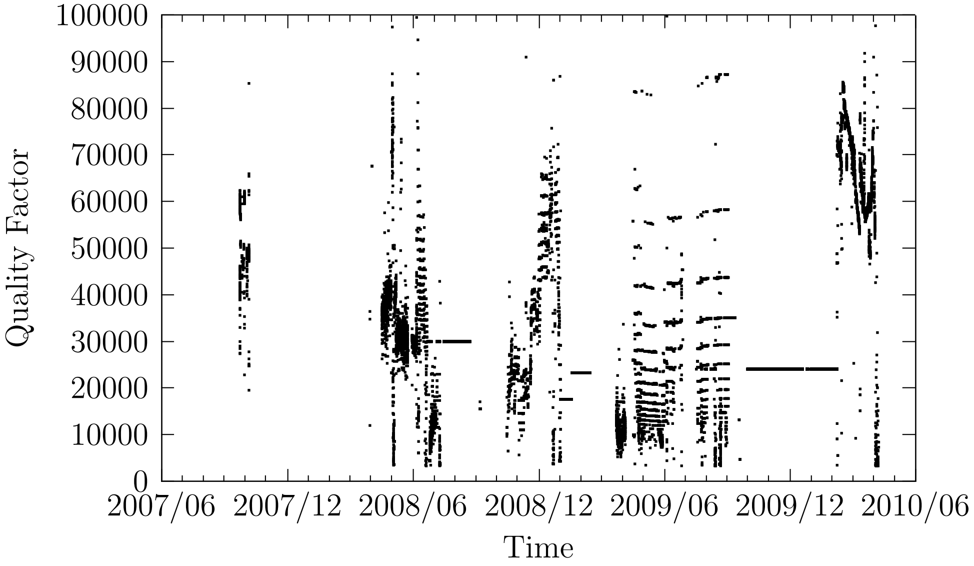

Figure B.1: The quality factor throughout running. The horizontally layered areas are caused by poor Q fits from an outdated minimization subroutine. Note the sudden improvement during 2010 operations

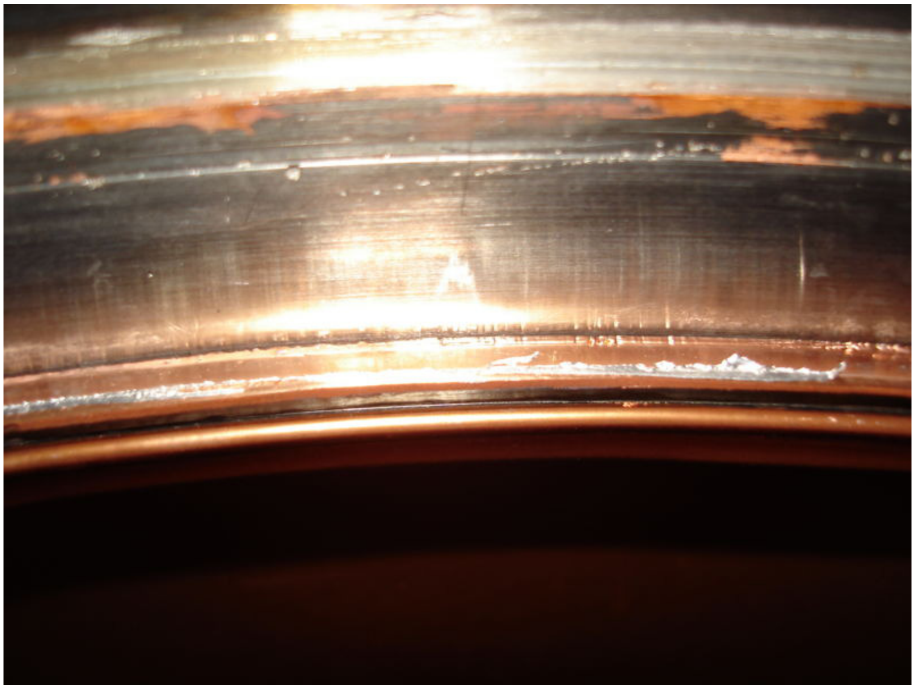

Figure B.2: The copper plating completely separated from the knife edge, causing poor conductance between the end cap and walls. The gray metal is traces indium later installed to fix the issue.

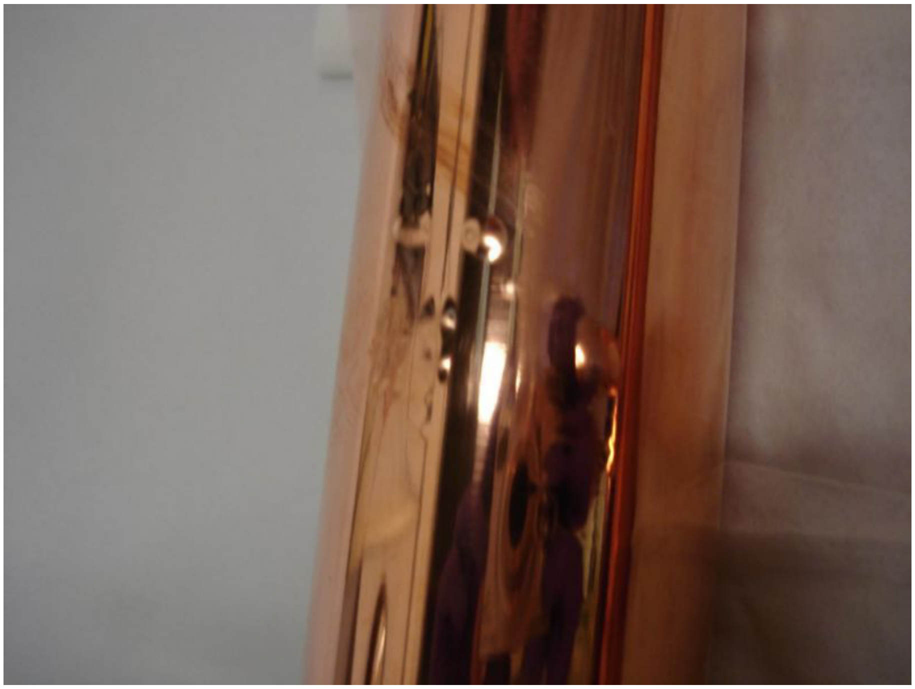

Figure B.3: The copper on the tuning rod has bubbled up off the stainless. Since there was no tear, these structures had little effect on the Q.

Appendix C

Squid Operations

ADMX had run for 10 years with HEMT amplifiers before the installation of a SQUID amplifier. HEMT amplifiers are balanced, stable, and robust. HEMT amplifiers operate in a large range of bias points and are easily driven by a feedback controlled current sources. During typical operations, the HEMT amplifiers required no maintenance besides an occasional LED flash to unfreeze charge carriers.

ADMX operated under the assumption that the SQUID amplifiers would operate similarly. At the start of operations, none of the on-site operators knew how to tune the SQUID. Initial operations of ADMX were punctuated with long periods of poor performance. Figure C.1 shows how the SQUID would fail frequently, typically by degrading over several days. The best indicator of SQUID health was the average power from the receiver chain, labeled FFT_Avg. A healthy SQUID would output more power than a dead SQUID. It was found that -55.5 dBV indicated a dead SQUID, which acts as a short, making the HEMT the primary amplifier. Whenever the FFT_Avg dropped below -55 dBV any data recorded was cut from the analysis and the SQUID was retuned.

To tune the SQUID, the current bias was first tuned to be over the critical current of roughly 8 μA. For retuning the SQUID, the current bias typically did not need any adjustment. Then, the flux bias was tuned until either the network analyzer showed maximum

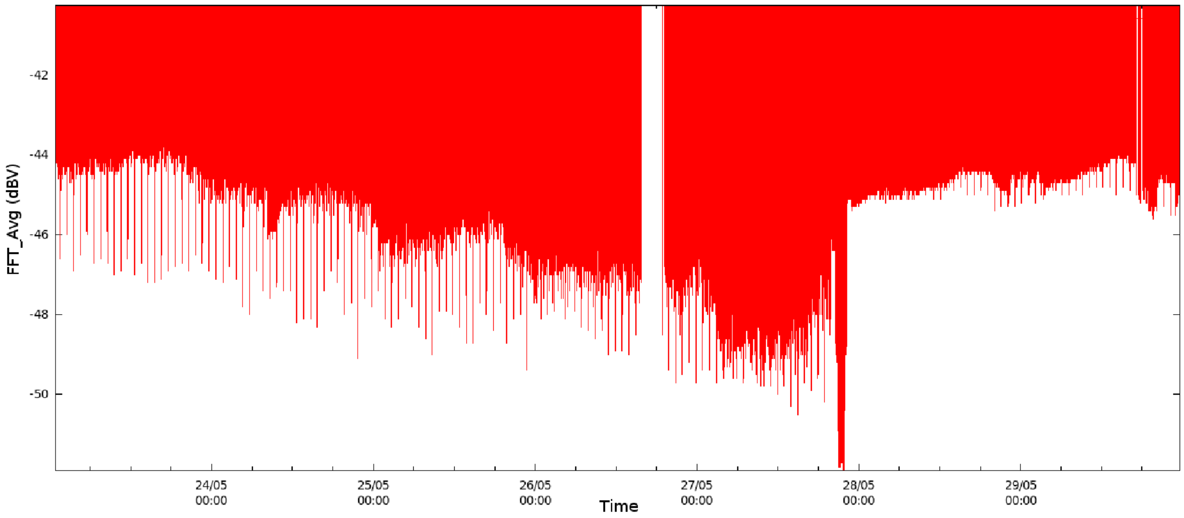

Figure C.1: The typical cycle of SQUID health. Drift in bias points would typically kill the SQUID's gain every week or so. During original running, no one on-site knew how to retune the SQUID, leading to very poor duty cycle and large gaps in the data.

gain[1] or the FFT showed a maximum noise floor. At good tuning, the FFT_Avg would be around -44 dBV. Some fine tunings created higher output, quickly jumping to -40 dBV. It is known that a SQUID does not produce minimal noise at maximum gain, so these tuning settings were avoided.

The SQUID input is far from matching impedance to our 50 Ω cables and components, including the critically coupled TM_{010} mode of the cavity. To combat this, most of our running used an isolator to eliminate any unwanted resonances. An isolator is a circulator with one port terminated. The isolator would attenuate signals reflected off the SQUID by 30 dB from 500 MHz to 1 GHz while only attenuating the input power by 0.2 dB. Unfortunately, while a large magnetic field at the SQUID would typically only kill the SQUID temporarily, it destroyed the isolator permanently, since the isolator uses a permanent magnet with a uniform field. Cryogenic isolators have long lead times, leading to our running without one for a period of time. Amazingly, operating without an isolator did not seem to deteriorate SQUID performance.

---

[1] With the scalar network analyzer used before 4/12/09, this was impossible.

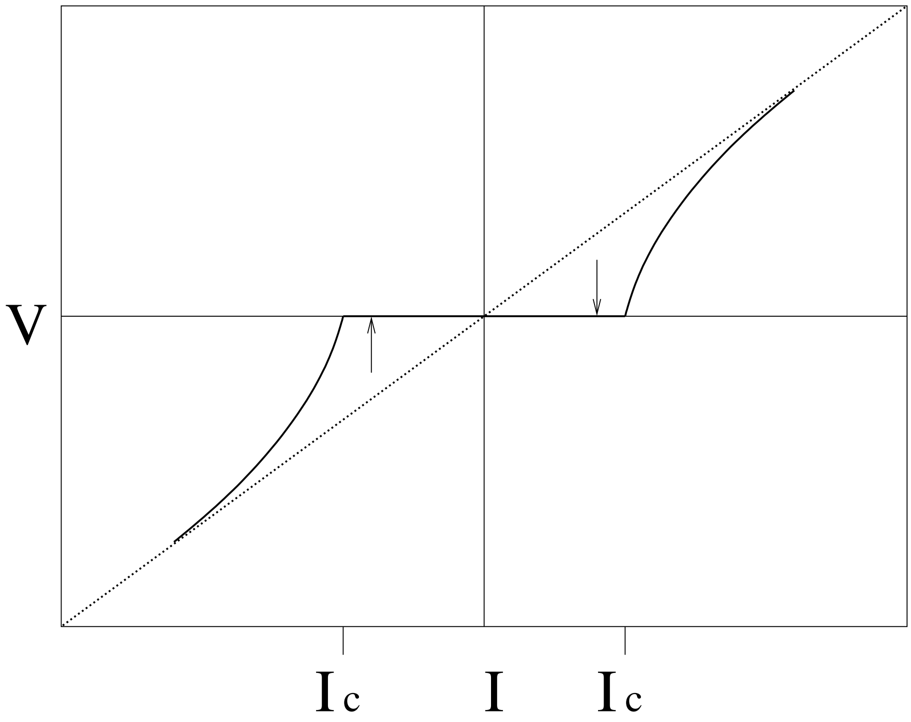

Figure C.2: A drawing of the IV curve for a SQUID. The I-V curve of the SQUID was measured at low frequency with an oscilloscope and function generator. A healthy SQUID (solid line) should be a superconductor until its critical current, Ic, of roughly 8 μA is reached, then transition to a resistive conductor. An unhealthy SQUID (dotted line) resembled follows the resistive I-V curve. For unknown reasons, flashing the HEMT LEDs eliminated this problem for roughly 10 minutes. This solution was automated, but never really understood.

The SQUID output has the same issue as the input: it is not matched to the 50 Ω transmission line or the balanced HEMT amplifiers. While the HEMTs attenuated reflected power by roughly -20 dB, this seemed to be too much for the SQUID to operate. A correlation was noticed that flashing the LED's of the HEMTs, which should only effects the HEMT's noise performance, would improve the SQUID's health. Figure C.2 shows the diagnostic I-V curve used to judge the health of the SQUID. Flashing the HEMT LED's nearly routinely returned a dead SQUID to life, but the SQUID would typically die again in 15 minutes or so. Unable to find an explanation for this behavior, we choose to automatically flash the LED's every 10 minutes to keep the SQUID healthy. We were told later that standard practice is to use another isolator between the SQUID and HFET post-amplifier, which might have prevented this behavior.

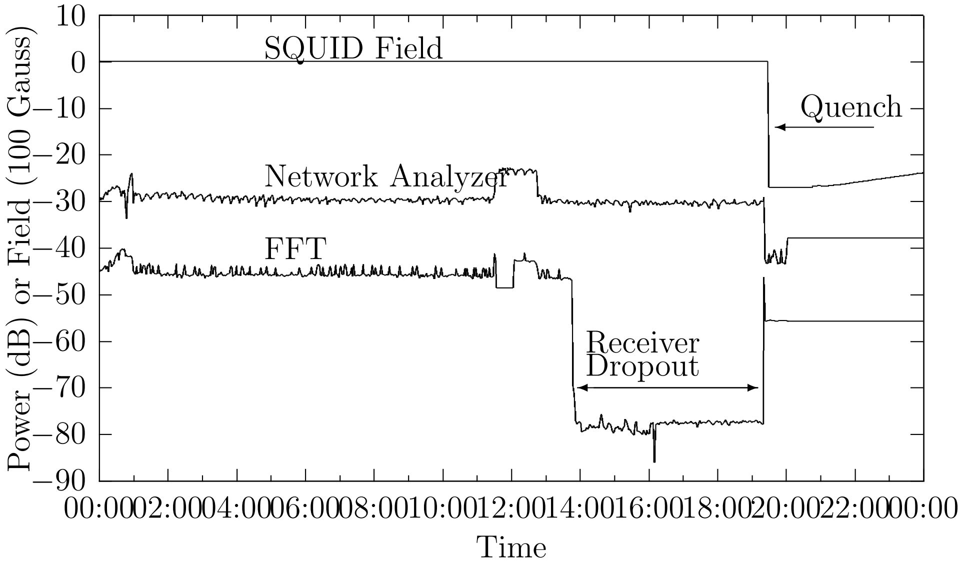

Figure C.3: The SQUID's response to a magnet quench. The field at the SQUID went from 0 to .2 Tesla during the bucking magnet quench. The loss in gain is apparent from both the Network analyzer's response and the FFT's. The region after the SQUID death gives us a baseline for when the SQUID is not functioning as an amplifier. There is also a period during the middle of the day where the receiver box overheated, which should be ignored.

From 4/12/09 onward, we replaced the Scalar Network Analyzer with a more sensitive Vector Network Analyzer or VNA. This allows for us to sweep the cavity without exceeding the SQUID's dynamic range. With the combination of gain tracking with the VNA and power tracking with the FFT, we had a proxy for noise temperature. While we could not track absolute gain or noise temperature, the best evidence that our SQUID amplifiers worked was when they failed. Figure C.3 shows when our bucking magnet failed. In it, the VNA read -29.5 dBm when the SQUID was healthy and -42 dBm when the SQUID was dead. Likewise, the FFT read -46 dBV then -55.5 dBV.

Appendix D

Issue with LabView Power Spectra

For every cavity tuning, the Hires ADC took 3 sets of 1906840 samples at 80KS/s. Each time series was Fourier transformed into a power spectrum. The transforms were performed by LabView during data taking. The set of three resulting power spectra were averaged into a single power spectra to save disk space. These power spectra form the basis of ADMX high resolution analysis.

The raw power spectra are averaged together to form a receiver shape spectrum. This averaged spectrum is subtracted from the raw spectra to produce flattened spectra. The flattened spectra are trimmed down to the 30 kHz passband of the crystal filter. A 5th order polynomial is fitted then subtracted from each trimmed spectra to remove any remaining wide structures on the data. Peak detection is used prior to the fit to minimize subtracting out narrow structures. The processed spectra are then scaled to their expected axion power and added together to form a single axion power spectrum, from which a limit is derived.

With a Nyquist resolution of 42 mHz, once flattened and trimmed, the power spectra's deviations fit a χ^2 distribution of degree 6, shown in figure D.1. However, once pairs of adjacent frequency bins are added to lower the resolution to 84 mHz, the deviations do not fit the expected χ^2 distribution of degree 12 shown in figure D.2. The ratio of $\frac{\delta P}{P}$ reflects this departure of χ^2's $\frac{\delta P}{P} = \sqrt{\frac{2}{k}}$ where k is the degrees of freedom. Figure D.3 shows $\frac{\delta P}{P}$

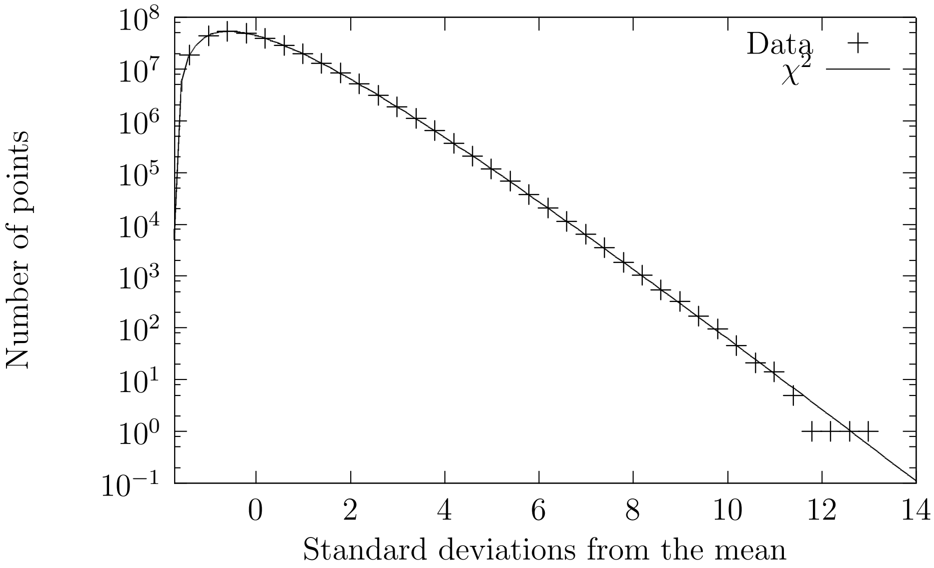

Figure D.1: The distribution of the raw LabView generated power spectra data, showing good agreement with the χ^2 distribution of degree 6.

goes from 20% higher at 2 bins to 50% higher for 512 bins. Figure D.4 shows a strong 2 bin auto-correlation, which would cause this anomaly. The mechanism of the LabView FFT that causes this issue is the Hann windowing applied before the FFT.

Any analysis performed using resolution coarser than 42 mHz with the LabView data has its integration time effectively halved. The ADMX analysis scales the flattened power spectra to their expected thermal noise power but only scales the deviations if they are better than expected. Any limit calculated from the LabView generated power spectra dataset will be valid but be poorer than expected.

After March 2009, each individual Hires time series was also saved. Figure D.4 shows that the resulting power spectra from the transformed time series do not show significant auto-correlation, even with zero padding to 2^{21} samples to improve FFT performance. The transforms were done with the FFTW package. These power spectra have the expected χ^2 $\frac{\delta P}{P}$ as bins are added, shown in figure D.5. By using time trace data, the full integration time leads to significantly improved limits.

Unfortunately, a bug in the LabView DAQ failed to save the appropriate state data to

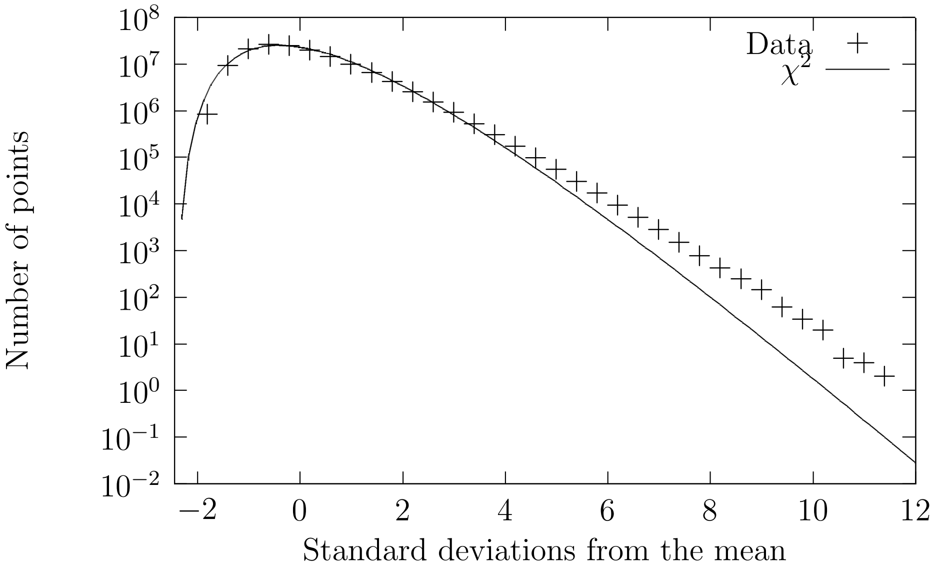

Figure D.2: The distribution of the LabView power spectra data at half resolution, showing poor agreement with the χ^2 distribution of degree 12.

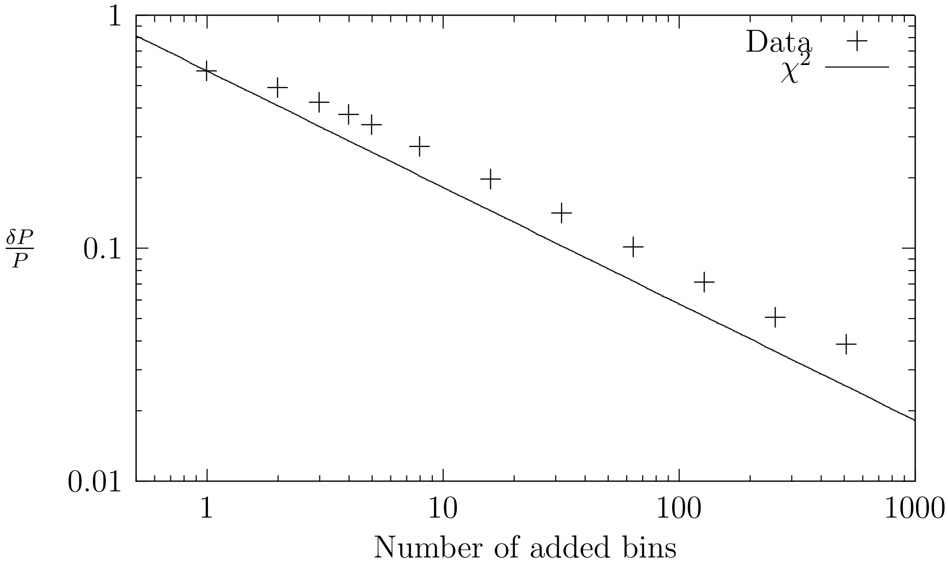

Figure D.3: $\frac{\delta P}{P}$ vs number of added bins for the LabView generated power spectra. Notice the divergence from the expected value.

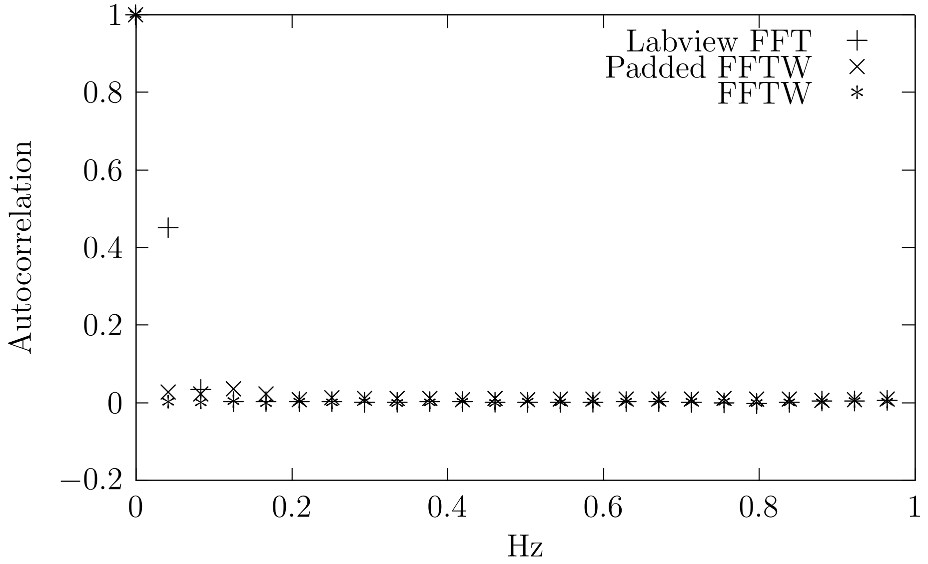

Figure D.4: The Auto-correlation vs Frequency for LabView power spectra vs FFTW generated power spectra. The Labview power spectra have a strong 2-bin correlation while FFTW does not.

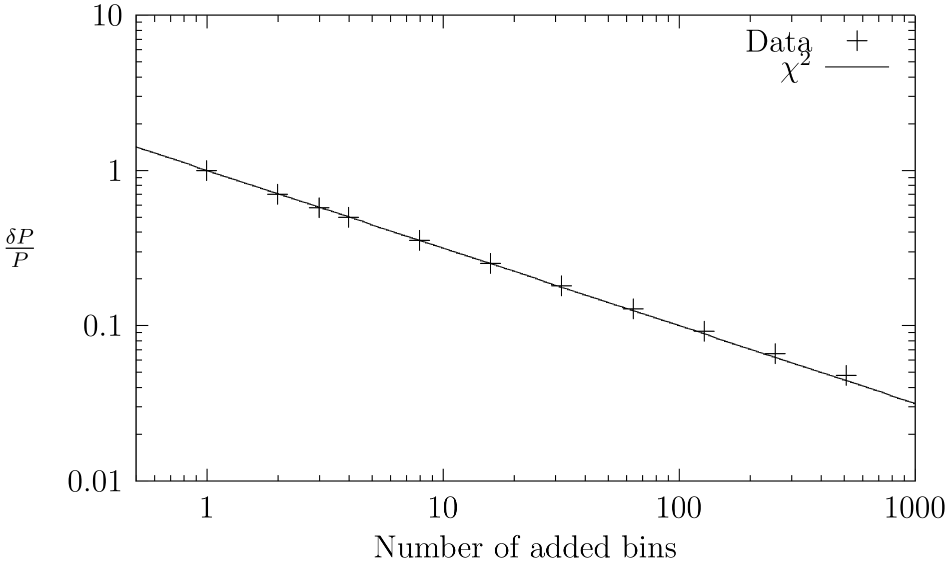

Figure D.5: $\frac{\delta P}{P}$ vs number of added bins for the FFTW generated power spectra.

each time series. Fortunately, there is an accurate time stamp inside each time series file, making look-up of appropriate data reliable. Also, since the we did not save the time series data from May 2008 to April 2009, the data around 850 MHz is limited to the inferior LabView power spectrum data. Since data taking was more problematic early in the experiment, only about 15% of usable data is only available as LabView power spectra.

Appendix E

Hole in Data

While running, the SQUID health was often not well known. What was assumed to be good data was later found to be unusable. As discussed in appendix C, the best data point (FFT_Avg=-55.5 dBV) on a dead SQUID came from a quench, but the receiver gain after the SQUID was changed several times, making this point slightly variable through running.

Rigorous SQUID health cuts on the dataset created areas of low SNR and one area with no limit at 862 MHz. Figure E.1 shows the times where the experiment scanned the region of the hole in the data. Figure E.2 shows the FFT_Avg from the first scan of the region. The low value of FFT_Avg indicates that the SQUID was dead, so this data was cut due to the poor health of the SQUID. The DAQ had failed during the second scan, saving no data. Figure E.3 shows a spectrum from the final scan, which was cut due to the receiver changing shape, resulting in a poor fit.

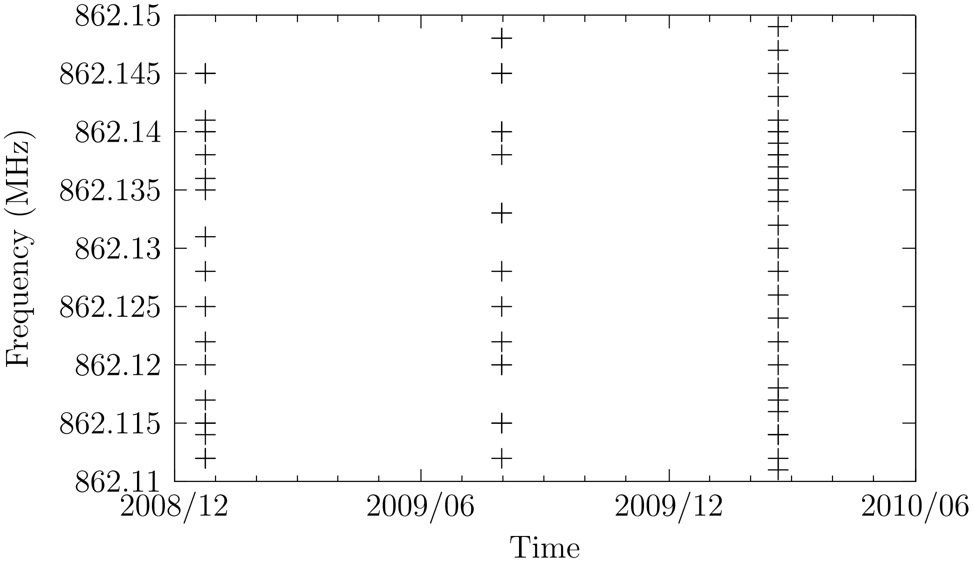

Figure E.1: The three scans through the hole in the dataset. The first scan was performed during a period when the SQUID had poor gain. The second scan had a DAQ failure, and no data was taken. The third scan contained external radio peaks.

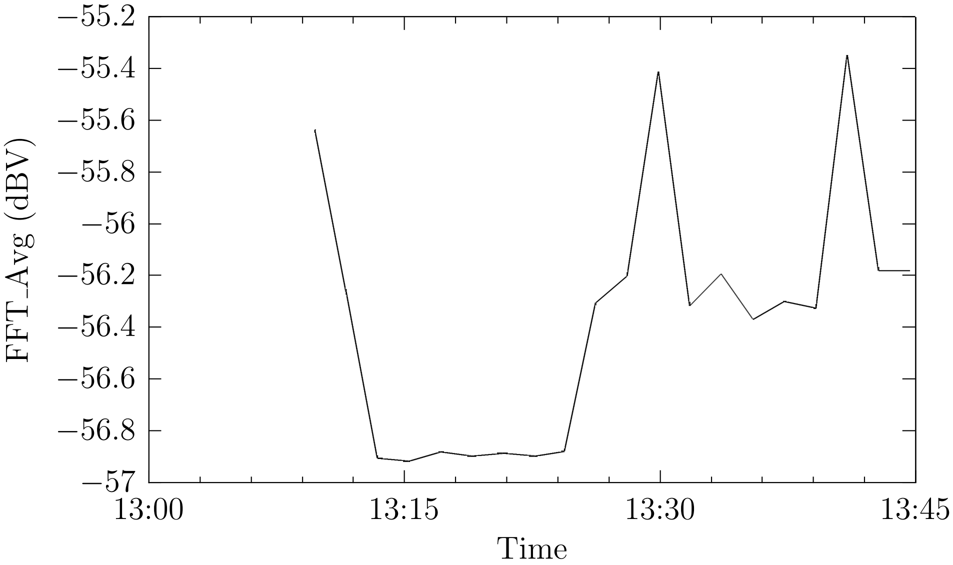

Figure E.2: The FFT_AVG from the first scan through the hole region on the afternoon of December 24 2008. The SQUID was considered dead through this region.

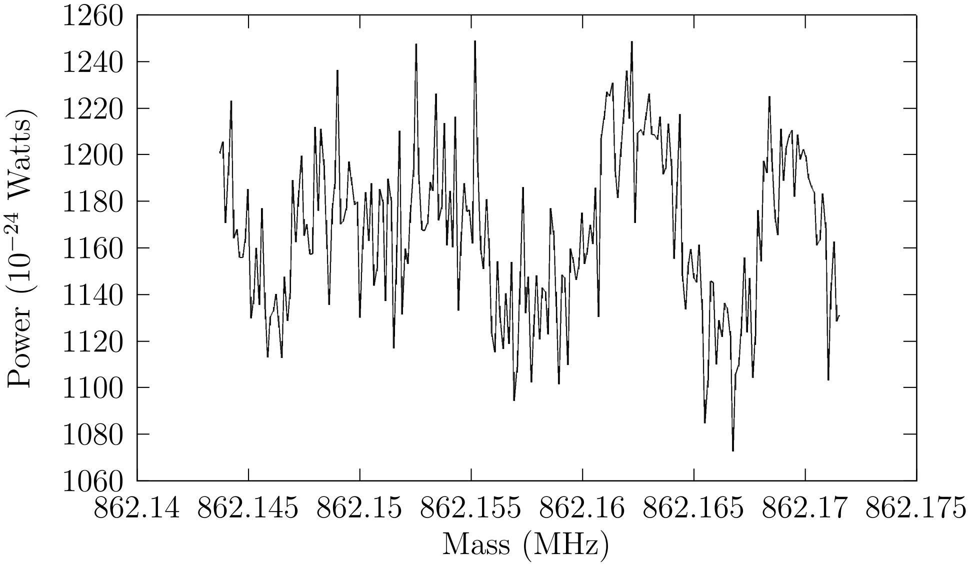

Figure E.3: The unstable receiver shape during the third pass resulted in spectra with excessive structure.

Bibliography

[1] M. Shifman, A. Vainshtein, and V. Zakharov, Nuclear Physics B **166**, 493 (1980).

[2] R. D. Peccei and H. R. Quinn, Phys. Rev. Lett. **38**, 1440 (1977).

[3] S. Weinberg, Phys. Rev. Lett. **40**, 223 (1978).

[4] F. Wilczek, Phys. Rev. Lett. **40**, 279 (1978).

[5] WMAP Collaboration, G. Hinshaw *et al.*, Astrophys.J.Suppl. **180**, 225 (2009), 0803.0732.

[6] N. R. C. Committee on the Physics of the Universe, *Connecting Quarks with the Cosmos:Eleven Science Questions for the New Century* (The National Academies Press, 2003).

[7] C. W. Purcell, J. S. Bullock, and M. Kaplinghat, ApJ **703**, 2275 (2009).

[8] L. Duffy and P. Sikivie, Phys.Rev. **D78**, 063508 (2008), 0805.4556.

[9] M. Gell-Mann, Phys. Rev. **125**, 1067 (1962).

[10] E. D. Bloom *et al.*, Phys. Rev. Lett. **23**, 930 (1969).

[11] S. Weinberg, Phys. Rev. D **11**, 3583 (1975).

[12] S. L. Adler, Phys. Rev. **177**, 2426 (1969).

[13] J. Bell and R. Jackiw, Il Nuovo Cimento A **60**, 47 (1969).

[14] C. C. Jr., R. Dashen, and D. Gross, Physics Letters **63B**, 334 (1976).

[15] R. Jackiw and C. Rebbi, Phys. Rev. Lett. **37**, 172 (1976).

[16] A. Belavin, A. Polyakov, A. Schwartz, and Y. Tyupkin, Physics Letters B **59**, 85 (1975).

[17] G. 't Hooft, Phys. Rev. Lett. **37**, 8 (1976).

[18] C. A. Baker *et al.*, Phys. Rev. Lett. **97**, 131801 (2006).

[19] J. t. P. D. G. Beringer, Phys. Rev. , 010001 (2012).

[20] D. Antreasyan *et al.*, Physics Letters B **251**, 204 (1990).

[21] J. t. P. D. G. Beringer, Phys. Rev. , 010001 (2012).

[22] J. E. Kim, Phys. Rev. Lett. **43**, 103 (1979).

[23] M. Shifman, A. Vainshtein, and V. Zakharov, Nuclear Physics B **166**, 493 (1980).

[24] M. Dine, W. Fischler, and M. Srednicki, Physics Letters B **104**, 199 (1981).

[25] A. R. Zhitnitsky, Sov. J. Nucl. Phys. , 260 (1980).

[26] E. Hubble, Proceedings of the National Academy of Science **15**, 168 (1929).

[27] A. A. Penzias and R. W. Wilson, Astrophycial Journal **142**, 419.

[28] J. H. Oort, BAIN **6**, 249 (1932).

[29] F. Zwicky, ApJ **86**, 217 (1937).

[30] V. C. Rubin, W. K. J. Ford, and N. . Thonnard, ApJ **238**, 471 (1980).

[31] B. Catinella, R. Giovanelli, and M. P. Haynes, The Astrophysical Journal **640**, 751 (2006).

[32] C. Alcock *et al.*, The Astrophysical Journal Supplement Series **136**, 439 (2001).

[33] F. Iocco, G. Mangano, G. Miele, O. Pisanti, and P. D. Serpico, Physics Reports **472**, 1 (2009).

[34] E. W. Kolb and M. S. Turner, *The Early Universe*Frontiers in Physics (Addison-Wesley Publishing Company, 1990).

[35] R. Cowsik and J. McClelland, Phys. Rev. Lett. **29**, 669 (1972).

[36] S. A. Thomas, F. B. Abdalla, and O. Lahav, Phys.Rev.Lett. **105**, 031301 (2010), 0911.5291.

[37] A. Kusenko, Physics Reports **481**, 1 (2009).

[38] K. N. et. al. (Particle Data Group), J. Phys. **G 37**, 075021 (2010).

[39] H. Baer, V. Barger, and A. Mustafayev, Phys.Rev. **D85**, 075010 (2012), 1112.3017.

[40] E. Mass, **741**, 83 (2008).

[41] S. Hellerman and J. Walcher, Phys.Rev. **D72**, 123520 (2005), hep-th/0508161.

[42] T. Hiramatsu, M. Kawasaki, K. Saikawa, and T. Sekiguchi, Phys. Rev. D **85**, 105020 (2012).

[43] M. Kamionkowski and A. Kinkhabwala, Phys. Rev. D **57**, 3256 (1998).

[44] X. X. Xue *et al.*, ApJ **684**, 1143 (2008), 0801.1232.

[45] G. Battaglia *et al.*, Mon.Not.Roy.Astron.Soc. **364**, 433 (2005), astro-ph/0506102.

[46] M. Zemp *et al.*, Mon.Not.Roy.Astron.Soc. **394**, 641 (2009), 0812.2033.

[47] A. M. Brooks, M. Kuhlen, A. Zolotov, and D. Hooper, (2012), 1209.5394.

[48] T. Abel, O. Hahn, and R. Kaehler, (2011), 1111.3944.

[49] M. Volgelsberger and S. D. M. White, MNRAS **413**, 1419 (2011).

[50] J. Einasto and U. Haud, AAp **223**, 89 (1989).

[51] M. Volgelsberger *et al.*, MNRAS **395**, 797 (2009).

[52] C. M. Bidin, G. Carraro, R. Mendez, and W. van Altena, Astrophys.J. **724**, L122 (2010), 1011.1289.

[53] D. Grin *et al.*, Phys. Rev. D **75**, 105018 (2007).

[54] P. Sikivie, Phys. Rev. Lett. **51**, 1415 (1983).

[55] C. Hagmann, P. Sikivie, N. S. Sullivan, and D. B. Tanner, Phys. Rev. D **42**, 1297 (1990).

[56] W. U. Wuensch *et al.*, Phys. Rev. D **40**, 3153 (1989).

[57] L. J. Rosenberg, SSI04 (2004).

[58] J. D. Jackson, *Classical Electrodynamics*, Third ed. (Wiley, 1998).

[59] A. B. Pippard, Proceedings of the Royal Society of London. Series A. Mathematical and Physical Sciences **191**, 385 (1947), http://rspa.royalsocietypublishing.org/content/191/1026/385.full.pdf+html.

[60] J. Clarke and A. I. Braginski, *The SQUID Handbook: Volume 2 Applications of SQUIDs and SQUID Systems* (Wiley, 2006).

[61] W. Heitler, *The Quantum Theory of Radiation* (Courier Dover Publications, 1954).

[62] R. Bradley *et al.*, Rev. Mod. Phys. **75**, 777 (2003).

[63] T. V. Duzer and C. W. Turner, *Principles of Superconductive Devices and Circuits*, Second ed. (Prentice Hall, 1998).

[64] ADMX Collaboration, S. Asztalos *et al.*, Phys.Rev.Lett. **104**, 041301 (2010), 0910.5914.

[65] J. Hoskins *et al.*, Phys.Rev. **D84**, 121302 (2011), 1109.4128.

[66] R. A. Méndez, I. Platais, T. M. Girard, V. Kozhurina-Platais, and W. F. van Altena, ApJ **524**, L39 (1999), arXiv:astro-ph/9908118.

[67] S. R. Majewski, Proceedings of the International Astronomical Union **3**, 450 (2007).

[68] M. C. Smith *et al.*, Mon.Not.Roy.Astron.Soc. **379**, 755 (2007), astro-ph/0611671.